EI 92

ACTA POLYTECHNICA SCANDINAVICA

ELECTRICAL ENGINEERING SERIES No. 92

Electromechanical Properties of Radial Active Magnetic Bearings

MATTI ANTILA

Helsinki University of Technology
Laboratory of Electromechanics
P.O.Box 3000
FIN-02015 HUT
Finland

Dissertation for the degree of Doctor of Technology to be presented with due permission for public examination and debate in Auditorium S4 at Helsinki University of Technology, Espoo, Finland, on November 20, 1998, at 12 o'clock noon.

ESPOO 1998

El 92
ACTA
POLYTECHNICA
SCANDINAVICA
ELECTRICAL ENGINEERING SERIES No. 92

Electromechanical Properties of Radial Active Magnetic Bearings

MATTI ANTILA

Helsinki University of Technology
Laboratory of Electromechanics
PO 3000
02015 HUT
Espoo
Finland

Antila M. **Electromechanical properties of radial active magnetic bearings**. Acta Polytechnica Scandinavica, Electrical Engineering Series No. 92, Espoo 1998, 96 pp. Published by the Finnish Academy of Technology. ISBN 952-5148-73-4. ISSN 0001-6845.

Keywords: Active magnetic bearings, linearised parameters, finite element method, reluctance network method

Abstract

Nonideal properties of the electromagnetic actuators in radial active magnetic bearings are studied. The two dimensional nonlinear stationary finite element method is used to determine the linearised parameters of a radial active magnetic bearing. The method is verified on two test machines. The accuracy is 10-15 % in the magnetic saturation region. The effect of magnetic saturation on the bearing dynamics is studied based on the root locus diagrams of the closed loop system. These diagrams show the possibility of extending the operation range into the magnetic saturation region. The magnetic cross coupling between the x- and y-coordinates is studied in detail. The formulation in which the cross coupling can be regarded as phase errors is presented. The magnetic cross coupling can produce phase errors up to ten degrees. The effect of the power amplifier saturation is studied based on the nonlinear simulations and describing function approach. A high frequency large amplitude disturbance can be an origin for a limit cycle oscillation in the neighborhood of the crossover frequency.

The eddy currents in the laminations, magnetic hysteresis and unmodelled eddy current paths produce phase errors to the linearised parameters. These errors are studied by measurements and models based on the reluctance network. The dynamic force measurement is done by measuring the accelerations at the both ends of the rotors and solving the equation of the motion of the rotor. The eddy current model is derived from the one-dimensional magnetic field solution inside an electric steel sheet. The model is a linear model, which is linearised at one operation point of the radial bearing. This model neglects the excess losses and the unmodelled eddy current paths. The linearised parameters from the hysteresis model are calculated by the describing function. These phenomena can produce phase errors up to ten degrees.

Preface

This work was carried out at the Laboratory of Electromechanics, Helsinki University of Technology. The work is a part of the research project "Development of a high-speed electric motor". The project was financed by Graduate School of Ministry of Education, Technology Development Center (TEKES) and High Speed Tech Oy Ltd.

I wish to express my gratitude to Professor Tapani Jokinen, Head of the Laboratory of Electromechanics, for his encouragement and advice during the course of the work. I also wish to thank Dr. Antero Arkkio, Dr. Juhani Tellinen and other members of the laboratory staff for helpful discussions and advices as well as enjoyable atmosphere to work in. Furthermore, I would like to thank the personnel of High Speed Tech Oy Ltd. for the close collaboration in this challenging project. Finally, I am obliged to the prestigious AMB-group: Mr Erkki Lantto, Mr Ville Tommila and Mr Marko Palko. Working in this highly skilled group has been an honor and a privilege for me.

For the delightful moments with sailing, skiing, floorball and leisure time I express my gratitude to my friends. Without these moments the toil would have been unbearable.

The lifelong support of my father and my late mother has been the backbone and essence of my studies and work. No words can express my debt of gratitude. My sister Minna, and Tommi, I thank you for your friendship when it mattered the most. Hanna-Mari has been my sun and moon, my rain and wind, thank You for the sacrifices done to carry out this work.

Financial support by the Foundation of Technology in Finland (Tekniikan Edistämissäätiö) and the Finnish Cultural Foundation, Häme Regional Fund is gratefully acknowledged.

Espoo, October 1998

Matti Antila

Contents

List of symbols

$\boldsymbol{A}$	vector potential
A	z-component of $\boldsymbol{A}$
A_h	cross sectional area of a branch reluctance
A_p	area of one pole
$\boldsymbol{a}$	vector of nodal values of vector potential
a_j	j^{th} element of $\boldsymbol{a}$
$\boldsymbol{B}$	magnetic flux density
B_ave	average flux density across the lamination
$B_\mathrm{H-}, B_\mathrm{H+}$	limiting hysteresis curves
B_s	flux density at the surface of the lamination
b_i	width of the i^{th} branch reluctance
c, c_0, $\boldsymbol{c}$	position stiffness, scalar, nominal, matrix
$\boldsymbol{D}_\mathrm{rot}$	modal damping matrix
d	thickness of lamination
F, $\boldsymbol{F}$	force general, scalar, vector
F_b	bearing force
$F_{\omega\mathrm{max}}$	maximum bearing force at the angular disturbance frequency of ω
f_ave	average relative response on the rotational control
$\boldsymbol{f}_\mathrm{h}$	vector of branch magnetomotive forces of the reluctance network model
f_r	relative response on the rotational control
$\boldsymbol{G}_\mathrm{B}$	transfer function matrix of the bearing
$\boldsymbol{G}_\mathrm{C}$	transfer function matrix of the controller
$\boldsymbol{G}_\mathrm{J}$	Jacobian matrix coupling the local and global coordinates in finite element method
$\boldsymbol{G}_\mathrm{R}$	transfer function matrix of the rotor
$\boldsymbol{G}_\mathrm{rot}$	modal gyroscopic coupling matrix
$\boldsymbol{G}_\mathrm{S}$	transfer function matrix of the position sensors
g_h	relative describing function of the current reference to bearing force function
$\boldsymbol{H}$	magnetic field strength
h_s	height of the slot
h_f, h_f0, $\boldsymbol{h_\mathrm{f}}$	current stiffness, scalar, nominal, matrix

$h_{\mathrm{f(u,d),(D,N)}}$	current stiffness, up or down magnet, D- or N-end bearing
h_i	height of the i^{th} branch reluctance
h_{v}, $\boldsymbol{h_{\mathbf{v}}}$	velocity induced voltage coefficient
$\boldsymbol{i}_{\mathrm{AC}}$	current phasor
i_{bias}	bias current
$\boldsymbol{i}_{\mathrm{ec}}$	vector of branch eddy currents
$\boldsymbol{i}_{\mathrm{ecfe}}$	vector of eddy currents
i_{hf}	high frequency component in the nonlinear simulation model
i_{max}	maximum current
$i_{\mathrm{c}}, \boldsymbol{i}_{\mathrm{c}}$	control current, scalar, vector
i_{ref}	reference current
$i_{\mathrm{u}}, i_{\mathrm{d}}$	current in the upper and lower coil
$\boldsymbol{i}$	coil current vector
$\boldsymbol{I}$	diagonal unity matrix
$\boldsymbol{J}_{\mathrm{e}}, J_{\mathrm{e}}$	current density in the eddy current model
$\boldsymbol{J}$	current density
J	z-component of $\boldsymbol{J}$
$\mathbf{K}_{\mathrm{B}}$	uncertainty matrix of the bearing model
$\mathbf{K}_{\mathrm{R}}$	uncertainty matrix of the rotor model
$\boldsymbol{K}_{\mathrm{rot}}$	modal stiffness matrix
$\mathbf{K}_{\mathrm{U}}$	uncertainty matrix of the plant
$\boldsymbol{K}_1$	linearised current to loop flux coefficient matrix
$\boldsymbol{K}_2$	linearised displacement to loop flux coefficient matrix
$\boldsymbol{K}_3$	linearised eddy current to loop flux coefficient matrix
$\mathbf{K}_{\mathrm{tf1}}$	transformation matrix from branch flux vector to modified branch flux vector
$\mathbf{K}_{\mathrm{tf2}}$	transformation matrix from eddy current vector to branch eddy current vector
k_{p}	geometric pole factor

L_{dyn}, L_{dyn0}, $\boldsymbol{L}_{\mathbf{dyn}}$	dynamic inductance, scalar, nominal, matrix
$L_{\mathrm{f(u,d),(D,N)}}$	dynamic inductance, up or down magnet, D- or N-end bearing
L_e, $\boldsymbol{L}_e$	integration path in the eddy current model
L_{ecj}	j^{th} inductance of the eddy current model
$\boldsymbol{L}_w$	winding path
l_i	axial length of the i^{th} branch reluctance
$\boldsymbol{M}_{\mathrm{f}}$	vector of the loop magnetomotive forces in the reluctance network model
$\boldsymbol{M}_{\mathrm{rot}}$	modal mass matrix
N	number of turns per pole
N_f	number of free nodes
N_i	shape function of i^{th} node in the finite element method
N_n	number of nodes in a finite element mesh
N_w	number of turns in a winding
$\boldsymbol{N}$	coupling matrix of coil currents and loop magnetomotive forces
$\boldsymbol{n}$	unit normal vector of the integration surface
$\boldsymbol{P}$	Jacobian of the system equation in the finite element method or in the reluctance network method
$\boldsymbol{p}$	position vector
$\boldsymbol{Q}$	system matrix of the hysteresis model
R, $\boldsymbol{R}$	resistance, scalar, diagonal matrix
R_{C}	resistance of the coil
$\boldsymbol{R}_{\mathrm{m}}$	diagonal reluctance matrix
R_{ecj}	j^{th} resistance of the eddy current model
R_{S}	resistance of the shunt
r_r	outer radii of the airgap
r_s	inner radii of the airgap
$\boldsymbol{r}$	column vector of residual functions in the finite element method or in the reluctance network method
r_i	i^{th} element of $\boldsymbol{r}$
S, $\boldsymbol{S}$	integration surface, surface vector
S_{ag}	the cross sectional area of the airgap
S_e	integration area in the eddy current model
$\mathbf{T}$	loop-set matrix of reluctance network model

$\boldsymbol{u}_{\mathrm{AC}}$	voltage phasor
u_{c}, $\boldsymbol{u}_{\mathbf{c}}$	control voltage
$u_{\max}$	maximum voltage in the power amplifier
$\boldsymbol{u}_{\mathrm{s}}$	source vector in the hysteresis model
V	volume
$\boldsymbol{v}_{\mathrm{n}}$	n^{th} eigenvector
W	weight function in Galerkin's method
W_c	magnetic coenergy
W_m	magnetic energy
x, y, z	Cartesian coordinates
x_{ref}	position reference
$\boldsymbol{z}$	vector of loop-fluxes and coil currents in the hysteresis model
α	pole angle of the bearing
δ	airgap
$\Delta F_{\mathrm{b}}, \Delta \boldsymbol{F}_{\mathrm{b}}$	deviation of bearing force from equilibrium, scalar, vector
$\Delta i_{\mathrm{c}}, \Delta \boldsymbol{i}_{\mathrm{c}}$	deviation of control current from equilibrium, scalar, vector
$\Delta i_{\mathrm{ref}}, \Delta \boldsymbol{i}_{\mathrm{ref}}$	deviation of reference current from equilibrium, scalar, vector
$\Delta u_{\mathrm{c}}, \Delta \boldsymbol{u}_{\mathrm{c}}$	deviation of control voltage from equilibrium, scalar, vector
$\boldsymbol{\phi}_{\mathrm{h}}$	vector of branch fluxes of reluctance network model
$\boldsymbol{\phi}_{\mathrm{hf}}$	vector of iron branch fluxes
$\boldsymbol{\phi}_{\mathrm{hfe}}$	modified branch flux vector
ϕ_{hi}	i^{th} branch fluxes of reluctance network model
ϕ_k	flux of the k^{th} coil
$\boldsymbol{\Phi}$	vector of loop fluxes of reluctance network model
Γ	integration path
λ_{n}	n^{th} eigenvalue
μ	permeability
μ_0	permeability of vacuum
ν	reluctivity
ν_0	reluctivity of vacuum
ω	angular frequency
Ω	integration surface
Ω_m	mechanical angular frequency
Ψ, $\boldsymbol{\Psi}$	flux linkage, scalar, vector
Ψ_k	flux linkage of the k^{th} coil
$\boldsymbol{\sigma}$	Maxwell's stress sensor
σ	conductivity

1 Introduction

1.1 Introduction to high-speed technology

In this thesis, the term high-speed technology is used in the following meaning. In high-speed technology, the working or load machine, such as a compressor or a pump, an electric motor and a cooling fan has a common rotor. Thus, the load machine is directly driven by the electric motor without any gears. The electric motor is supplied and the rotation speed is controlled by a frequency converter. A typical speed range is from 20 000 to 200 000 RPM and the corresponding power range is from 300 kW to 20 kW. Currently, the main applications are water treatment compressors and vacuum pumps for the pulp and paper industry. Some details of the high-speed technology can be found from papers [Lindgren et al. 1995, Antila et al. 1996, Lantto et al. 1997].

The need for the high rotation speed comes from the fact that the load machine, for example, a turbo compressor, needs high rotational speed to perform with high efficiency. The demand of the speed and power range is determined by the performance map of a compressor. The performance map of the compressor has to match the demand of the application. These principles are covered in [Larjola 1988].

The high rotational speed imposes some technical difficulties which need to be overcome. The combination of the speed and power sets the torque range the electric motor has to produce. This means that the size of the rotor is such that the peripheral speed of the rotor may exceed 250 m/s. In this range, conventional induction motors made of laminated steel sheets cannot be used, due to excessive mechanical stresses. Thus, the rotor has to be made of solid iron and to guarantee satisfactory electric efficiency the rotor is coated by a thin layer of conducting material [Patent U.S. 5473211]. On the other hand, as the rotation speed of the machine increases the power-size ratio of the machine increases. This increases the power density as well as the loss power density in the machine. So, the cooling of the machine needs special attention and this is thoroughly covered in [Saari 1995], [Saari 1998].

Finally, the conventional roller bearings cannot be used at high speeds due to a limited or even negligible life time. A contactless suspension of the rotor is necessary at high speeds. Active magnetic bearings have proven to be a suitable solution in high-speed compressors. Thus, the benefits of high-speed technology can be listed: the high efficiency of the total application, first, due to the high efficiency of the turbo compressor, electric motor and, second, the possibility to control the operation point of the compressor by rotational speed. Small size and weight, minimum maintenance due to few wearing components, negligible vibration due to contactless suspension, oil free operation and small size enables direct integration into processes. Fig. 1(a) presents the main components of the high-speed compressor. The high-speed unit consists of the electric motor, turbo compressor and the cooling fan in a

common shaft. Radial and axial magnetic bearings maintain the contactless support of the high-speed rotor.

(a) Several high-speed turbo compressors in parallel operation

(b) The electric units, the frequency converter and AMB-controller

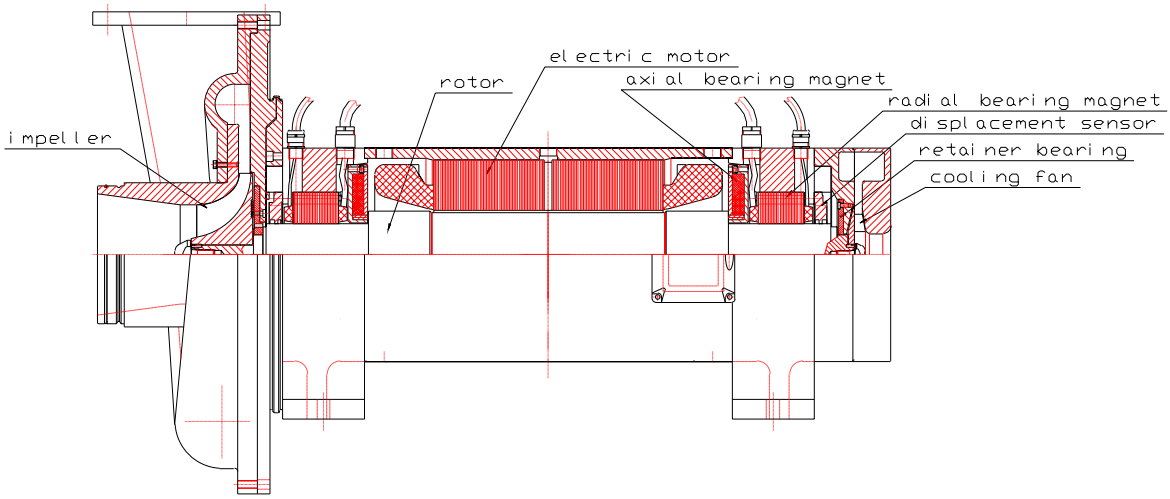

Figure 1: High-speed turbo compressor consists of a high-speed unit and an electric cabinet. Schematic diagram of a high-speed unit.

1.2 Introduction to Active Magnetic Bearings (AMB)

1.2.1 General

The idea of contactless support of objects has been intriguing the human mind for centuries. The idea of using magnetic field comes first to mind. However, one faces some laws of nature, which heavily bound the usage of magnetic forces for contactless support of objects. The best known is the theorem of Earnshaw [Earnshaw 1842], which says that an object in a passive magnetic field can achieve a stable position only if the material of the object is diamagnetic or superconducting. This feature restricts engineering applications of passive fields quite a bit, as most of the machines designed by engineers are made of ferromagnetic material. However, permanent magnets can be used to support a few degrees of freedom of a ferromagnetic rigid body, if at least one degree of freedom is supported by other means. In any case, the stiffness and damping properties of permanent magnet bearings are insufficient for many practical applications. The major applications where permanent magnet bearings are used are turbo-molecular pumps and household electric energy counters [Fremerey 1988]. Recently, bearings based on the superconductors have gained reasonable interest amongst researchers, but practical applications are still to be found [Moon 1994].

On the contrary, active magnetic bearings (AMB) have become a widely accepted and used solution for contactless support rotors [Brunet 1988], [Dussaux 1990]. This field has different types of technical solutions and extensive reviews of different types of electromagnetic levitation systems are made by [Bleurer 1992], [Jayawant 1981]. In addition, it is worth noting the book by Schweitzer et. al. 1994 [Schweitzer et al. 1994], which not only reviews magnetic levitation types but also gives a thorough introduction to AMB. Also, the report made by Zhuravlyov [Zhuravlyov 1992] can be seen as a practical handbook for people wanting to get familiar with AMB and a tutorial paper can be found made by Lantto and Antila [Lantto and Antila 1995].

In AMB, the five degrees of freedom of a rotor are controlled by electromagnets. Fig. 2 shows the principle of active magnetic bearing in one coordinate axis. The electromagnets at opposite sides pull the rotor and the total force acting on the rotor is the sum of the forces of the electromagnets. The interaction between the ferromagnetic rotor and electromagnets is unstable. Thus, the position of the rotor has to be measured and the currents in the coils have to be controlled to maintain the suspension. In the suspension system, the five degrees of freedom are controlled by four radial bearings (two at each end of the rotor) and one axial bearing. In principle, the suspension could be realized without position sensors by estimating the position of the rotor from coil currents and voltages. This type of sensorless bearing is not covered in this thesis.

In this thesis, the current controlled radial AMB system with position measurements is studied. By the current controlled AMB it is meant that the position controller output is

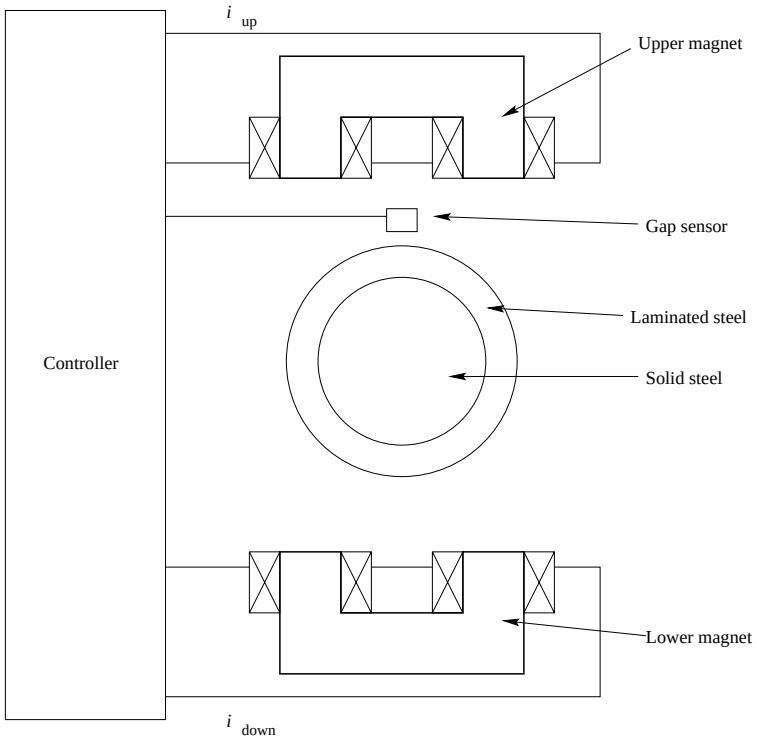

Figure 2: Principle of an active magnetic bearing.

a current reference. This reference is the input to the current control circuit in which the output is a control voltage applied to the coil.

In radial bearings, the rotor consists of a solid core and outer part made of laminated steel. The purpose of the lamination is to reduce the effects of eddy currents when the rotor is rotating and when the bearing forces are controlled. The stator is made of laminated steel as well. The winding of an electromagnet is made of regular copper wire. The axial bearings are separate magnets manufactured from solid iron.

1.2.2 Linear magnetic circuit theory and the linearised dynamic model of AMB

As mentioned in the previous section, a control feedback loop is necessary for a stable AMB suspension. Thus, in the end, the design problem is reduced to a control system synthesis. When designing the controller an accurate and reliable magnet actuator model is of primary importance. While most of the control system design tools are based on linear models, the bearing actuator model should be a linear block in the control loop. The first approach to creating a bearing model is the linear magnetic circuit theory, where it is assumed that the permeability of the iron is infinite, the flux density in the airgap is in radial direction and leakage flux is zero. The force of the bearing depends on the flux density in the air gap. The flux density is controlled by the currents in the coils. The force-current dependence of magnets at one coordinate axis is highly nonlinear and is approximated

$$F_{\mathrm{b}} = \frac{\mu_0 (N i_{\mathrm{u}})^2}{(\delta - k_{\mathrm{p}} x)^2} A_{\mathrm{p}} k_{\mathrm{p}} - \frac{\mu_0 (N i_{\mathrm{d}})^2}{(\delta + k_{\mathrm{p}} x)^2} A_{\mathrm{p}} k_{\mathrm{p}} \tag{1}$$

where μ_0 is the permeability of vacuum, $2Ni_{\mathrm{u}}$ and $2Ni_{\mathrm{d}}$ are the magnetomotive forces of the opposite magnets, δ is the air gap, x is the position of the shaft, A_{p} is the area of one pole and k_{p} is a geometric pole factor and for a eight pole bearing k_{p} is 0.924. This nonlinear dependence is often linearised to simplify the control system. The linearisation is realized by supplying bias-current i_{bias} into both coils at the opposite sides of the rotor. This bias-flux can also be supplied by permanent magnets [Sortore et al. 1990]. The control of the force in that particular direction is done by adding a control current i_{c} into the other coil and subtracting it from the other one. Therefore, the total force, for example, in x-direction depends linearly on the control current i_{c}. In addition, the nonlinear spatial force dependence can be linearised by assuming $x \ll \delta$.

$$F_{\mathrm{b}} = \frac{4\mu_0 i_{\mathrm{bias}} N^2 A_{\mathrm{p}} k_{\mathrm{p}}}{\delta^2} i_{\mathrm{c}} + \frac{4\mu_0 i_{\mathrm{bias}}^2 N^2 A_{\mathrm{p}} k_{\mathrm{p}}^2}{\delta^3} x \tag{2}$$

$$F_{\mathrm{b}} = h_{\mathrm{f}} i_{\mathrm{c}} + c x \tag{3}$$

The coefficients of i_{c} and x are the current stiffness h_{f} and negative position stiffness c, respectively. The dynamic model is formed by taking the linearised voltage equations of the bearing magnets. Also, when considering a point mass one has to take the equation of motion into the model. Thus, the dynamic model of a point mass levitating between two electromagnets is

$$m\ddot{x} - cx = h_{\mathrm{f}} i_{\mathrm{c}} \tag{4}$$

$$u_{\mathrm{c}} = L_{\mathrm{dyn}} \dot{i}_{\mathrm{c}} + h_{\mathrm{v}} \dot{x} + R i_{\mathrm{c}} \tag{5}$$

$$\frac{d}{dt} \begin{bmatrix} x \\ \dot{x} \\ i_{\mathrm{c}} \end{bmatrix} = \begin{bmatrix} 0 & 1 & 0 \\ c/m & 0 & h_{\mathrm{f}}/m \\ 0 & -h_{\mathrm{v}}/L_{\mathrm{dyn}} & -R/L_{\mathrm{dyn}} \end{bmatrix} \begin{bmatrix} x \\ \dot{x} \\ i_{\mathrm{c}} \end{bmatrix} + \begin{bmatrix} 0 \\ 0 \\ 1/L_{\mathrm{dyn}} \end{bmatrix} u_{\mathrm{c}} \tag{6}$$

where c is the negative position stiffness, h_{f} is the current stiffness, h_{v} is the velocity induced voltage coefficient, m is the mass of the rotor reduced to the AMB position, L_{dyn} is the coil inductance (also based on linear magnetic circuit theory), R is the coil resistance, x is the displacement, i_{c} is the control current, u_{c} is the control voltage. This form of the linearised dynamic model of AMB is widely used when designing the control system of AMB. In this thesis, the parameters of Eqs. $2 \cdots 6$ are referred as the ideal linearised parameters of AMB.

1.2.3 Position sensor, controller and power amplifier

In Fig. 3, a more detailed presentation of a current controlled AMB in one coordinate axis is presented. In this section, the key components of the AMB system are presented.

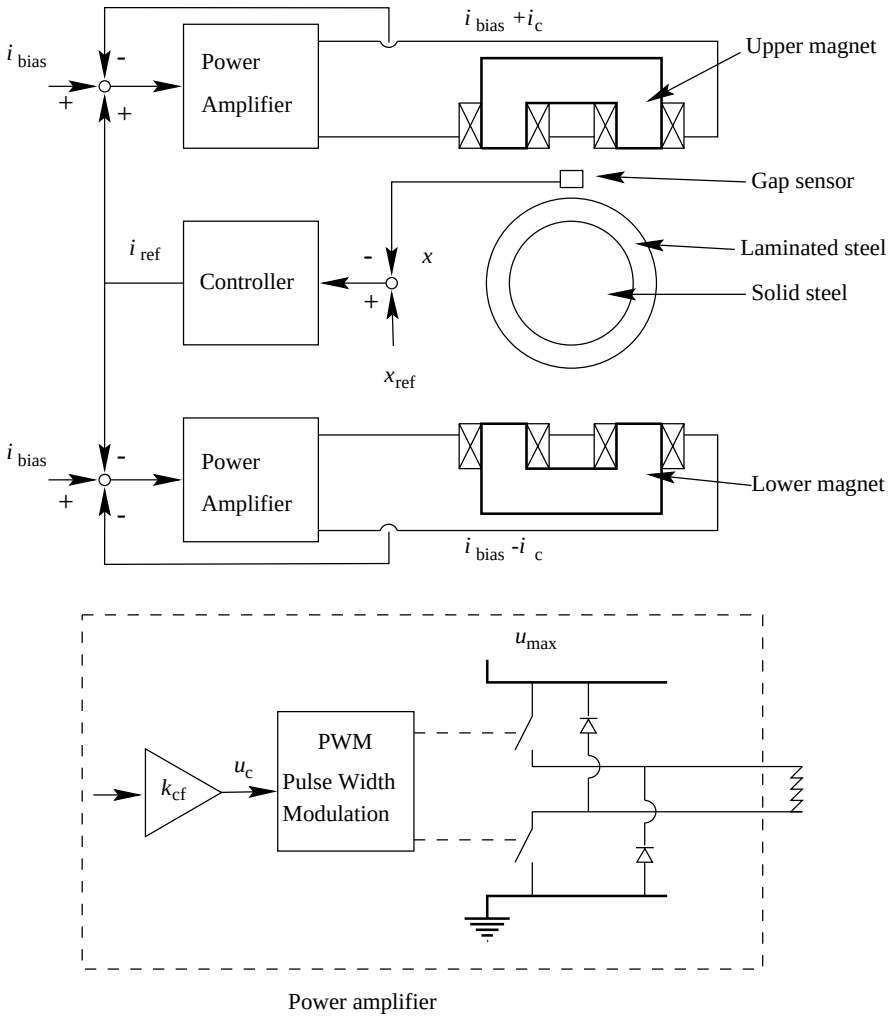

Figure 3: A detailed principle of a current controlled active magnetic bearing in one coordinate axis.

In active magnetic bearings, the position of the rotor in radial and axial directions can be measured by inductive, capacitive, eddy-current or optical sensors. The response of the sensor must be linear and the bandwidth should be over 1 kHz without any significant phase drop. In high-speed machines, the temperature varies in a large range so the position measurement has to be thermally stable. The noise of the measurement signal has to be low because the signal is amplified in the power amplifier and a noisy measurement signal results in audible noise in the bearing. The inverter-fed electrical motor causes large electrical disturbances, so the position measurement has to be electromagnetically compatible. Thermal enlargement of the rotor in axial direction is considerable in a high-speed machine. Therefore, it should be kept in mind that it is the location of the position sensor that is kept in the ordinary position and the clearances in the working machine and axial bearing might change. The test machines used in this thesis are equipped with inductive differential position sensors, that is, the position is measured from the difference of the sensors at the opposite side of the rotor. In addition, it is assumed in this thesis that the position sensors

are ideal, that is, with constant sensitivity and no phase lag.

The control system of an AMB is a widely studied subject. Recently, the classical analogous PID-type controllers [Habermann and Brunet 1984], [Humpris et al. 1986] have been replaced by digital controllers. These modern controllers are synthesised using methods of modern control strategies, such as H_∞, sliding mode and μ-synthesis, that have been implemented with DSP into AMB [Nonami and Yamaguchi 1992], [Bleurer et al. 1994], [Fujita et al. 1992], [Cui and Nonami 1992]. The newest trends in AMB control can be found from a special issue edited by Knospe [Knospe and Collins 1996]. In its simpliest form, the controller is realised by decentralised proportional integral derivative PID controllers. In one dimension, the current reference is $i_{\mathrm{ref}} = G(x_{\mathrm{ref}} - x)$, where G is the transfer function of the position controller. This topology gives at least satisfactory performance and robustness in many applications. In this thesis, the design of the control system or the control topology is not considered. The position controllers used in this thesis are analog PID-controllers with appropriate low-pass filters. In some of the controllers, there are cross connections between drive-end and non-drive-end bearings and some of the controllers are totally decentralised. The performance and robustness of these controllers have been verified in several high speed machines. The design of the controllers is thoroughly described in the thesis by Lantto [Lantto 1998].

In the current controlled AMB, the control current reference i_{ref} from the controller, the bias-current value i_{bias} and the current in the coil i are inputs to the power amplifier. The control voltage reference is the current difference multiplied by the current feedback coefficient k_{cf}, $u_{\mathrm{c}} = k_{\mathrm{cf}}(i_{\mathrm{ref}} + i_{\mathrm{bias}} - i)$. The control voltage reference is supplied into a pulse width modulation (PWM) -module, which gives the switching commands to the 1/2-H-bridge. This is the usual configuration used with analog and digital controllers. The switching frequency is usually from 30 kHz to 125 kHz. The voltage of the power amplifier can be from 50 V to 300 V and the current up to tens of amperes. In the power amplifier used in this thesis, the switching frequency is 60 kHz, the voltage is 100 V and current up to 10 A.

1.2.4 Static and dynamic bearing forces

Fig. 4 presents schematically the force an AMB can produce. In this section, the phenomena setting the limits on the AMB force are briefly studied.

The static bearing force is in the end limited by the flux density one can create into the airgap, thus magnetic saturation will bound the static load capacity. Thus, the size and geometry of the bearing dictates the maximum static bearing force. However, there are other technical boundary conditions to be met. The temperatures of the coils cannot rise above the limit of the insulation. The power amplifier also has a maximum current it can supply.

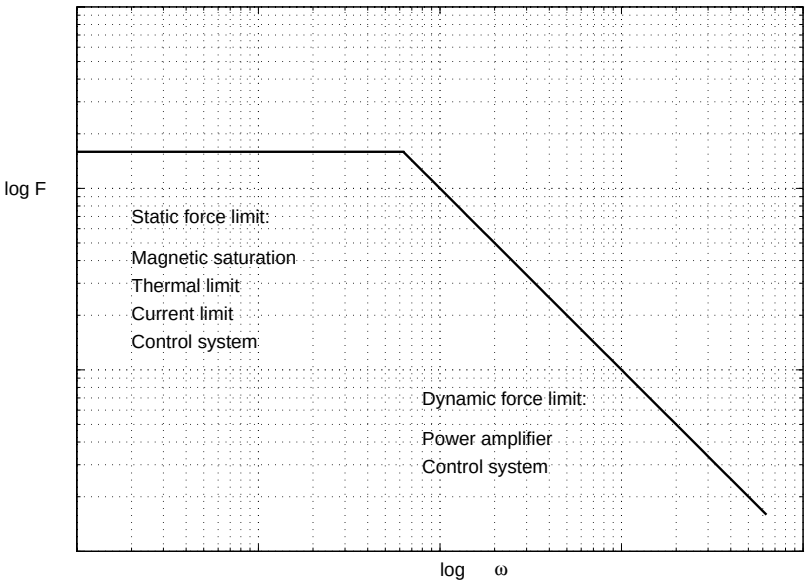

Figure 4: A schematic figure of the static and dynamic force of an AMB.

All this is based on the assumption that the control system can keep the suspension stable. All these conditions set the absolute maximum static force that an AMB can produce.

A magnetic bearing is basically a voltage source driving an inductor. Based on the linear magnetic circuit theory, a formula of the dynamic bearing force is easily solved. The velocity voltage term and position term are neglected as they are negligible at higher frequencies

$$u_{\max} i_{\max} = F_{\omega \max} \omega \delta \tag{7}$$

where $u_{\max}$ is the maximum control voltage available, $i_{\max}$ is the maximum current, $F_{\omega \max}$ is the maximum force at the disturbance angular frequency ω and δ is the airgap. Here, the maximum current is assumed to be exactly twice the bias current $i_{\max} = 2 * i_{\text{bias}}$ and the leakage flux and the geometric fact that the poles are usually not parallel to the coordinate direction are neglected. Usually the voltage of the power amplifier is fixed and the designer can make decisions to choose appropriate values for the airgap, number of turns and bias current to achieve the desired dynamic bearing force. These important basic results have been discussed by Bornstein [Bornstein 1991].

1.2.5 Rotordynamic model and unbalance compensation

In rotating machines, rotordynamic analysis is of crucial importance when studying and designing the behaviour of the machine. The rigid body models could easily be formed from the geometry of the machine. However, the elastic modes of rotor play an important role

in applications where rotational speed is "close" to the eigenfrequency of the elastic modes, especially with AMB's, where elastic modes have to be considered even when the rotational speed is "far" from the critical speed. Typically in high-speed technology, the rotational speed is about 20-30 percent under the first bending critical speed. In this thesis, a rotordynamic model based on the finite element model for the elastic rotating shaft is used [Lantto 1997]. In this method, the rotor shape is approximated by finite dimensional vectors and the rotor energies are expressed as a function of these vectors. The equations of motion are formed by inserting these energy expressions into Lagrangian equations. Then the finite dimensional equations of motion are reduced by modal coordinate transformation. In this reduction method, the finite dimensional equation of motion is solved with time harmonic assumption and the eigenfrequencies and -modes are calculated from the generalised eigenvalue problem. Finally, the equations of motions are

$$\boldsymbol{M}_{\mathrm{rot}}\,\ddot{\boldsymbol{q}}_X + \boldsymbol{D}_{\mathrm{rot}}\,\dot{\boldsymbol{q}}_X + \boldsymbol{K}_{\mathrm{rot}}\,\boldsymbol{q}_X + \Omega\,\boldsymbol{G}_{\mathrm{rot}}\,\dot{\boldsymbol{q}}_Y + \Omega\,\boldsymbol{D}_{\mathrm{rot}}\,\boldsymbol{q}_Y = \boldsymbol{F}_{\mathrm{X}} \tag{8}$$

$$\boldsymbol{M}_{\mathrm{rot}}\,\ddot{\boldsymbol{q}}_Y + \boldsymbol{D}_{\mathrm{rot}}\,\dot{\boldsymbol{q}}_Y + \boldsymbol{K}_{\mathrm{rot}}\,\boldsymbol{q}_Y - \Omega\,\boldsymbol{G}_{\mathrm{rot}}\,\dot{\boldsymbol{q}}_X - \Omega\,\boldsymbol{D}_{\mathrm{rot}}\,\boldsymbol{q}_X = \boldsymbol{F}_{\mathrm{Y}} \tag{9}$$

$$\boldsymbol{F}_{\mathrm{X}} = \boldsymbol{B}_{\mathrm{b}}\boldsymbol{F}_{\mathrm{b}X} + \boldsymbol{F}_{\boldsymbol{q}_X} + \Omega^2(\cos(\beta)\,\boldsymbol{U}_X - \sin(\beta)\,\boldsymbol{U}_Y) \tag{10}$$

$$\boldsymbol{F}_{\mathrm{Y}} = \boldsymbol{B}_{\mathrm{b}}\boldsymbol{F}_{\mathrm{b}Y} + \boldsymbol{F}_{\boldsymbol{q}_Y} + \Omega^2(\sin(\beta)\,\boldsymbol{U}_Y + \cos(\beta)\,\boldsymbol{U}_X) - \boldsymbol{F}_{\mathrm{G}} \tag{11}$$

$$\Omega = \dot{\beta} \tag{12}$$

$$\boldsymbol{p}_{\mathrm{s}X} = \boldsymbol{C}_{\mathrm{s}}\boldsymbol{q}_X \tag{13}$$

$$\boldsymbol{p}_{\mathrm{s}Y} = \boldsymbol{C}_{\mathrm{s}}\boldsymbol{q}_Y \tag{14}$$

where $\boldsymbol{M}_{\mathrm{rot}}, \boldsymbol{D}_{\mathrm{rot}}, \boldsymbol{K}_{\mathrm{rot}}, \boldsymbol{G}_{\mathrm{rot}}$ are the modal mass, damping, stiffness and gyroscopic matrices, respectively. $\boldsymbol{q}_X, \boldsymbol{q}_Y$ are the vectors of modal weights, $\boldsymbol{F}_{\boldsymbol{q}_X}, \boldsymbol{F}_{\boldsymbol{q}_Y}$ are external modal forces, $\boldsymbol{U}_X, \boldsymbol{U}_Y$ are the modal unbalance vectors and $\boldsymbol{F}_G$ is the modal gravitational force. The matrix $\boldsymbol{B}_{\mathrm{b}}$ couples the bearing forces $\boldsymbol{F}_{\mathrm{b}X}, \boldsymbol{F}_{\mathrm{b}Y}$ into modal coordinates and the matrix $\boldsymbol{C}_{\mathrm{s}}$ couples the modal weights into the rotor positions at the sensor locations $\boldsymbol{p}_{\mathrm{s}X}, \boldsymbol{p}_{\mathrm{s}Y}$. β is the rotational angle rotor and Ω is the angular frequency of the rotor. For a more detailed description of the rotor model see [Lantto 1997].

In Eqs. 10, 11, it is shown that the unbalance force is proportional to the square of the angular frequency. At high rotation speeds, relatively small unbalance causes a large rotational force. In Fig. 4, it was shown that the dynamic force of AMB is limited by the power amplifier voltage. In order to be able to cancel the unbalance force at high speeds, the power amplifier would have to be severely oversized. In practice, this problem is handled by an unbalance compensator. It can be realised in a number of ways, but the idea is to remove the rotational synchronous component from the control currents and

voltages. This is an important aspect of magnetic bearings at high speeds and has been a subject of recent studies[Larsonneur and Herzog 1994], [Knospe et al. 1997]. The unbalance compensator associated with this study, is presented by Lantto [Lantto 1998].

1.3 Review of AMB concerning this work

There are few publications on the prediction of the force and other electromagnetic properties of AMB. Imlach et al. [Imlach et al. 1991] used linear magnetic circuit theory to estimate the force and stiffness of radial AMB. The measurements were done with AMB installed in a canned motor pump. The agreement was found to be good at low eccentricities.

Knight et al. [Knight et al. 1992], [Knight et al. 1993] used linear finite element techniques to study one magnetic bearing actuator (C-magnet). The force calculations were done based on the virtual work method. The flux solutions were calculated in four positions of the rotor. The perturbations of the position were done in positive and negative x and y directions. The electromagnetic energy was then calculated at these positions and forces were calculated by differences. The measurements were done with an experimental setup, where a single c-magnet pulled the journal mounted into positioning disks. The material was assumed to be linear. They studied both the principal (diagonal) and normal (cross coupling) forces as functions of magnetomotive force and rotor position. The measurements were done at magnetomotive forces which corresponds to high level of saturation. The authors conclude that in order to be able to reliably estimate the cross coupling forces a nonlinear analysis is necessary. However, the measurements showed the ratio of cross coupling force and diagonal force of around 10 percent. This coupling was found to be almost linear with respect to the eccentricity in normal direction.

Hsiao and Lee [Hsiao and Lee 1994] used the nonlinear finite element technique to determine the force of radial magnetic bearing. They studied two types of radial bearings and the effects of geometric parameters. No measurements were done. The force of an AMB was calculated by using Maxwell's stress tensor method. Lee et. al. [Lee et al. 1994] studied a permanent magnet bias system with a magnetic circuit model. The static characteristics of a prototype were tested and compared with the estimated ones in the linear region. They noticed a discrepancy of 45.8 % in position stiffness and 66 % in current stiffness between the calculated and measured values at nominal point. They claimed the discrepancy was due to an underestimation of the leakage factor. After the corrections the agreement between estimated and measured forces was good at small displacements and coil currents.

Schmidt et. al. [Schmidt et al. 1996] compared linear finite element (FEM) and linear reluctance network methods when calculating the force and diagonal and cross coupling current stiffnesses. The agreement was found to be good in force and diagonal current stiffness calculations. The cross coupling stiffnesses showed noticeable differences between

the two methods. It is worth emphasising that the nonlinear nature of the iron was neglected in this study and therefore the cross coupling stiffnesses were found to be negligible.

Meeker and Maslen [Meeker and Maslen 1996] used linear network theory as well, but they studied the airgap region more precisely. They modelled the airgap region with magnetic vector potential and the iron was treated as a boundary condition of infinite permeability. Based on this solution the airgap reluctance was deduced.

Antila et. al. [Antila et al. 1998] determined the forces and linearised parameters by nonlinear 2D-FEM at different operation points. The calculations were verified with measurements done with two test bearings. The agreement was found to be satisfactory also far in the saturation region.

Common to all the above methods is that they are based on the stationary field solution. Thus, they neglect the effects of eddy currents and hysteresis, and the linearised parameters are all real valued. However, both these phenomena cause a small phase lag, for example, to the current stiffness. As these effects are usually neglected in the dynamic models, the true behaviour of an AMB system deviates from the designed one. Therefore, the control system designer has to be prepared for small phase errors when using static parameters. Previously, Zmood et. al. [Zmood et al. 1987] presented a simple expansion term into the current stiffness. This simple model effectively describes the qualitative nature of the eddy current effect in one coordinate dimension. Meeker and Maslen [Meeker and Maslen 1996] extended this formulation into arbitrary order. In addition, they derived the one-dimensional eddy current formulation into a form suitable for large networks. They also made impedance measurements over a large frequency range and compared the calculated impedance with the measured one. The calculations were done based on the complex reluctivity formulation. The agreement was found to be good and the major eddy current effects were found at frequencies above 1000 Hz.

1.4 Aim and contributions of this work

This work is a part of the high-speed technology project. In this project, the aim is to develop new types of compressors and pumps to be manufactured by series production. These machines are equipped with AMB. The demand of the series production poses new criteria for AMB as well, mainly, because in series production it is no longer possible to tune every machine individually.

Fig. 5 presents the blocks of an AMB system. In this thesis, the focus is in the modelling and properties of the electromagnetic actuator. The first aim in this study is to find and verify reliable methods to analyse the electromagnetic properties of the bearing actuators (the magnets) and based on the methods to create practical design guides for radial active magnetic bearings. The second aim is to find the uncertainties of the linearised parameters.

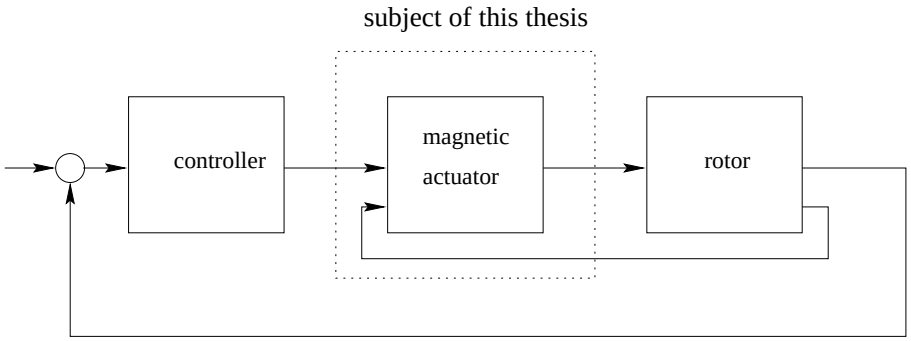

Figure 5: Sub blocks of a control system of an active magnetic bearing.

This is done based on the methods and measurements. These structured uncertainty blocks are then used when designing robust controllers for radial AMB [Lantto 1998].

This work is divided into two categories. First, the variation of the static parameters is studied. The main new contributions of this chapter are:

- Verifying the method (FEM) to determine the linearised parameters of radial AMB in the magnetic saturation region
- Determination of the variation of the linearised parameters due to the magnetic saturation and the effect of the variations to the bearing dynamics
- Determination of the magnetic cross coupling in radial AMB and the effect of the magnetic cross coupling to the bearing dynamics based on the response to a rotational control
- Quantifying the effect of the power amplifier saturation, especially the effect to the low frequency response when the saturation is caused by high frequency disturbances

Secondly, the variation of the linearised parameters caused by the hysteresis, eddy currents in the laminations and parasitic eddy current paths in the bearing magnets are studied. The main contributions of this chapter are:

- Implementing the one-dimensional eddy current model into the nonlinear reluctance network model and implementing the scalar hysteresis model into the reluctance network
- Verifying the models by dynamic inductance and dynamic force measurements
- Quantifying the magnitude and phase errors of the current stiffness caused by hysteresis, eddy currents in the lamination and parasitic eddy currents

2 Static parameters of radial AMB based on the stationary finite element method

2.1 Solution of the magnetic field

The magnetic field of the radial magnetic bearing is analysed by finite element method (FEM). The magnetic field is assumed to be two dimensional and stationary.

In the two-dimensional magnetostatic approximation the magnetic vector potential A in z or axial direction satisfy the equation

$$-\nabla \cdot (\nu \nabla A) = J \tag{15}$$

where ν is the reluctivity of the material and J is the current density in z-direction, which is known from the currents in the coils. In order to be able to solve Eq. 15 the boundary conditions have to be known. In magnetic bearings, it is assumed that no flux penetrates outside the stator of the magnetic bearing, therefore homogeneous Dirichlet boundary condition is applied on the outer boundary.

In this work, Galerkin's method is used in the discretisation of the two-dimensional field Eq. 15. In Galerkin's method, the shape functions connected to the free nodes are used one by one as the weight function. The Newton-Raphson iteration is used for solving the nonlinear system of equations. The nonlinear magnetisation of laminated and solid iron core is modelled with single-valued monotonic reluctivity curves. The second-order isoparametric elements are used in this work. The vector potential and flux density is calculated from the nodal values

$$A(x,y) = \sum_{j=1}^{N_n} N_j(x,y) a_j \tag{16}$$

$$\boldsymbol{B} = \nabla \times A \tag{17}$$

where a_j is a nodal value associated with the node j of the finite element mesh, N_j is a shape function associated with the node j and N_n is the number of nodes in the finite element mesh. The shape function N_j is a real-valued function having a value different from zero only in those elements that are connected to the mesh point j. The summation index j runs over all the node points of the mesh including also the points with fixed nodal values on the boundary.

In Galerkin's method, the two-dimensional differential equation is multiplied by a weight function W and integrated over the volume V of the solution region.

$$\int_V [-W \nabla \cdot (\nu \nabla A) - JW] dV = 0 \tag{18}$$

Using the identity

$$\nabla \cdot (\nu \nabla A) W = \nabla \cdot (W \nu \nabla A) - \nu \nabla W \cdot \nabla A \tag{19}$$

and Gauss's theorem the higher derivatives are eliminated from 18

$$\int_V [\nu \nabla A \cdot \nabla W - JW] dV = \oint_S \nu W \frac{\partial A}{\partial n} dS \tag{20}$$

Because there is no z-dependence and the surface integral vanishes at the end surfaces of the integration cylinder V and the volume integral can be changed to a surface integral over the cross section of the bearing by integrating over the z-coordinate

$$\int_\Omega [\nabla A \cdot \nabla W - JW] d\Omega = \oint_\Gamma \nu W \frac{\partial A}{\partial n} d\Gamma \tag{21}$$

where Ω denotes the two-dimensional solution region and Γ the boundary of Ω. The right-hand side vanishes on the Dirichlet boundary.

In Galerkin's method , the vector potential is approximated by Eq. 17 and the shape functions connected to the free nodes are used one by one as the weight function. Thus, the number of equations is equal to the number of unknown nodal values in the approximation. The system equations for this is

$$\int_\Omega \left\{ \nu \left[\sum_{j=1}^{N_n} a_j \nabla N_j \right] \cdot \nabla N_i - J N_i \right\} d\Omega = 0 \qquad\qquad i = 1 \cdots N_f \tag{22}$$

The nonlinear system of equations is solved by the Newton-Raphson iteration

$$\boldsymbol{P}(\boldsymbol{a}^k) \Delta \boldsymbol{a}^k = -\boldsymbol{r}(\boldsymbol{a}^k) \tag{23}$$

$$\boldsymbol{a}^{k+1} = \boldsymbol{a}^k + \Delta \boldsymbol{a}^k \tag{24}$$

where $\boldsymbol{r}$ is the vector of the residual functions r_i, $\boldsymbol{P}$ is the Jacobian of the system equations, k is the number of an iteration step, $\boldsymbol{a}^k$ is the vector of nodal values at the iteration step k and $\Delta \boldsymbol{a}^k$ is the correction added to $\boldsymbol{a}^k$ at the iteration step k. The elements of the Jacobian are the derivatives of the residual functions

$$P_{im} = \frac{\partial r_i(a_1^k, \cdots, a_N^k)}{\partial a_m^k} \tag{25}$$

$$= \int_\Omega \left\{ \sum_{j=1}^{N_n} \left(\frac{\partial \nu}{\partial a_m} \nabla N_l \cdot \nabla N_j a_j \right) + \nu \nabla N_l \cdot \nabla N_m \right\} d\Omega \tag{26}$$

The reluctivity ν can be expressed as a function of the square of the flux density

$$P_{lm} = \int_{\Omega} \left\{ \sum_{j=1}^{N_n} \left(\frac{\partial \nu}{\partial \boldsymbol{B}^2} \frac{\partial (\boldsymbol{B}^2)}{\partial a_m} \nabla N_l \cdot \nabla N_j a_j \right) + \nu(\boldsymbol{a}) \nabla N_l \cdot \nabla N_m \right\} d\Omega \tag{27}$$

The square of the flux density and its derivative are written

$$\boldsymbol{B}^2 = \sum_{i=1}^{N_n} \sum_{j=1}^{N_n} \nabla N_i \cdot \nabla N_j a_i a_j \tag{28}$$

$$\frac{\partial (\boldsymbol{B}^2)}{\partial a_m} = 2 \sum_{i=1}^{N_n} \nabla N_m \cdot \nabla N_i a_i \tag{29}$$

Thus, the Jacobian is now written

$$P_{lm} = \int_{\Omega} \left\{ 2 \sum_{j=1}^{N_n} \sum_{i=1}^{N_n} \left(\frac{\partial \nu}{\partial \boldsymbol{B}^2} [\nabla N_l \cdot \nabla N_j][\nabla N_m \cdot \nabla N_i] a_i a_j \right) + \nu \nabla N_l \cdot \nabla N_m \right\} d\Omega \tag{30}$$

where indexes i, j, l, m denote the nodes. The nonlinear magnetisation of laminated and solid iron core is modelled with a single-valued monotonic reluctivity cubic spline curve. A finite element mesh and a field plot are shown in Figs. 6 and 7.

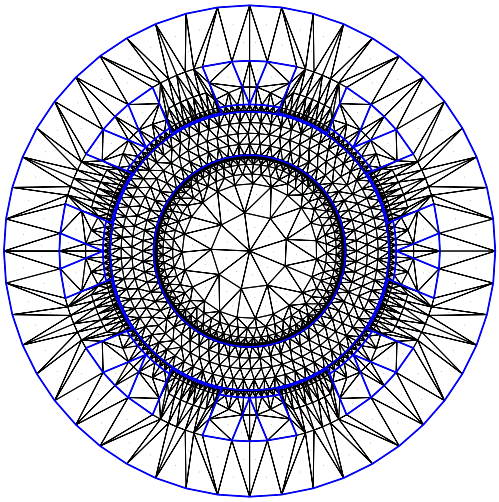

Figure 6: Finite element mesh plot of the radial magnetic bearing.

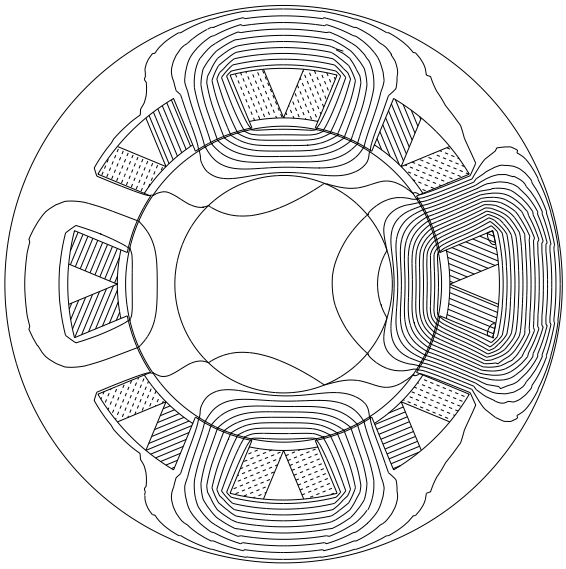

Figure 7: Field plot of the radial magnetic bearing based on the finite element solution.

2.2 Calculation of force and inductance

2.2.1 Maxwell's stress tensor

Methods based on Maxwell's stress tensor are commonly used in the calculation of forces and torques in the finite element analysis of electric devices [Reichert et al. 1976]. The electromagnetic force is obtained as a surface integral

$$\boldsymbol{F} = \oint_S \boldsymbol{\sigma} \cdot dS \tag{31}$$

$$\boldsymbol{F} = \oint_S \left[\frac{1}{\mu_0} (\boldsymbol{B} \cdot \boldsymbol{n}) \boldsymbol{B} - \frac{1}{2\mu_0} \boldsymbol{B}^2 \boldsymbol{n} \right] dS \tag{32}$$

where $\boldsymbol{\sigma}$ is Maxwell's stress tensor and $\boldsymbol{n}$ is the unit normal vector of the integration surface S. When Eq. 32 is applied to the calculation of the magnetic bearing forces, a closed integration surface that surrounds the rotor in free space must be chosen. In the two-dimensional model, the surface integral is reduced to a line integral along the air gap. If a circle of radius r_i is taken as the integration path, the force is obtained from the equation

$$F = \int_0^{2\pi} \left[\frac{1}{\mu_0} B_r B_\phi e_\phi - \frac{1}{2\mu_0} (B_r^2 - B_\phi^2) e_r \right] r d\phi \tag{33}$$

where B_r, B_ϕ are the r- and ϕ-components of the flux density. If the solution would be exact the force would be independent of the integration radius r_i when r_i varies within the air gap. However, the calculated force depends greatly on the choice of the integration radius and to achieve satisfactory accuracy the force is calculated over the whole area of the air gap. Due to the fact that the true force is independent of the radius integrating Eq. 33 results in

$$\boldsymbol{F}(r_s - r_r) = \int_{r_r}^{r_s} \int_0^{2\pi} \left[\frac{1}{\mu_0} B_r B_\phi e_\phi - \frac{1}{2\mu_0} (B_r^2 - B_\phi^2) e_r \right] r d\phi dr \tag{34}$$

$$\boldsymbol{F}(r_s - r_r) = \int_{S_{ag}} \left[\frac{1}{\mu_0} B_r B_\phi e_\phi - \frac{1}{2\mu_0} (B_r^2 - B_\phi^2) e_r \right] dS \tag{35}$$

$$\boldsymbol{F} = \frac{1}{r_s - r_r} \int_{S_{ag}} \left[\frac{1}{\mu_0} B_r B_\phi e_\phi - \frac{1}{2\mu_0} (B_r^2 - B_\phi^2) e_r \right] dS \tag{36}$$

where r_s and r_r are the outer and inner radii of the air gap respectively and S_{ag} is the cross sectional area of the air gap [Arkkio 1987]. This method is easy to implement into the FEM code. The drawback of the above method is the assumption of rotational symmetry. In case the rotor is eccentric, the previous method is not valid. At small eccentricities however, an approximate solution can be calculated

$$\Delta r(\phi) = r_s(\phi) - r_r(\phi) \tag{37}$$

$$\boldsymbol{F} = \int_{S_{ag}} \left[\frac{1}{\mu_0} B_r B_\phi e_\phi - \frac{1}{2\mu_0}(B_r^2 - B_\phi^2) e_r \right] \frac{1}{\Delta r(\phi)} dS \tag{38}$$

2.2.2 Virtual work

Another way to calculate the forces from a finite element field solution is based on the principle of virtual work [Coulomb 1983]. In this method, the force is calculated as a partial derivative of the coenergy functional with respect to virtual movement

$$W_c = \int_V \left(\int_0^{\boldsymbol{H}} \boldsymbol{B} d\boldsymbol{H} \right) dV \tag{39}$$

$$\boldsymbol{F} = \frac{\partial W_c}{\partial \boldsymbol{p}} = [\frac{\partial W_c}{\partial x} \quad \frac{\partial W_c}{\partial y}]^{\mathrm{T}} \tag{40}$$

where W_c is the coenergy functional and $\boldsymbol{F}$ is the force vector. The force in the direction of x is calculated as follows

$$F_x = \sum_e \int_{\Omega_e} \left[-[B_x \;\; B_y] \boldsymbol{G}_{\mathrm{J}}{}^{-1} \frac{\partial \boldsymbol{G}_{\mathrm{J}}}{\partial x} [H_x \;\; H_y]_{\mathrm{T}} + \int_0^{\boldsymbol{H}} \boldsymbol{B} d\boldsymbol{H} |\boldsymbol{G}_{\mathrm{J}}|^{-1} \frac{\partial \boldsymbol{G}_{\mathrm{J}}}{\partial x} \right] d\Omega \tag{41}$$

where the summation is done over virtually distorted finite elements. When applying this method to active magnetic bearings, the summation is over the air gap elements. $\boldsymbol{G}_{\mathrm{J}}$ is the Jacobian matrix which couples the local coordinates and the global ones. In this work, the force was calculated by Eqs. 38 and 41.

2.2.3 Dynamic inductance, current and position stiffness

The self and mutual inductances of the coils depend on the operation point of the bearing. In the dynamic model of Eq. 6, the dynamic inductance of the coil is needed. The dynamic inductance is defined

$$\boldsymbol{L}_{\mathrm{dyn}} = \frac{\partial \boldsymbol{\Psi}}{\partial \boldsymbol{i}} \tag{42}$$

where $\boldsymbol{\Psi}$ is the vector of the flux linkages and $\boldsymbol{i}$ is the vector of the coil currents. The flux of the coils is calculated from the solution of the vector potential according to Eq. 44.

$$\phi_k = \oint_{\boldsymbol{L}_w} \boldsymbol{A} \cdot d\boldsymbol{L}_w = l(A_{1k} - A_{2k}) \tag{43}$$

$$\Psi_k = \sum_{j=1}^{N_w} \phi_j = l \sum_{j=1}^{N_w} (A_{j1k} - A_{j2k}) \tag{44}$$

where $\boldsymbol{L}_w$ is the winding path, l is the axial length of the bearing, ϕ_k is the flux of the k^{th} coil, A_{1k} and A_{2k} are the vector potentials on the positive and negative sides of a winding

Table 1: Main dimensions of the test machines

Main dimensions of the AMB's of the test machines		
	Test machine 1	Test machine 2
Weight of rotor [N]	300	200
Stator diameter [mm]	164	135
Core length [mm]	45	45
Rotor diameter [mm]	93	54
Shaft diameter [mm]	64.3	40
Geometric air gap [mm]	0.4	0.5
Magnetic air gap [mm]	0.44	0.57
Number of turns per pole	100	100
Width of teeth [mm]	18	10
Slot to slot diameter [mm]	127	113
Thickness of stator lamination [mm]	0.5	0.5
Thickness of rotor lamination [mm]	0.35	0.35
Sheet material	Bochum V270	Bochum V270
Conductivity of the material [S]	$1.55 * 10^6$	$1.55 * 10^6$

turn of coil k, respectively. N_w is the number of turns in the winding. The inductance matrix is calculated based on the numerical derivatives of Eq. 42. In the same manner, the current stiffness and position stiffness matrices are calculated by numerical derivatives from Eqs. 45, 46.

$$\boldsymbol{h}_\mathrm{f} = \frac{\partial \boldsymbol{F}}{\partial \boldsymbol{i}} \tag{45}$$

$$\boldsymbol{c} = \frac{\partial \boldsymbol{F}}{\partial \boldsymbol{p}} \tag{46}$$

2.3 Experiments

2.3.1 Test setup of force measurement

The measurements were done with two motors equipped with active magnetic bearings. The first one is a high-speed test machine and the other one is a high-speed electric motor for compressor applications. The main parameters of the radial bearings are shown in Table 1.

In the force measurements, a pulley system was attached to one end of the shaft. A strain gauge was included in the pulley system to measure the applied load. The accuracy of the force measurement was 0.5 % $\pm$ 2 N. The applied force at the bearing position was

then calculated and the effect of the mass of the rotor was subtracted in order to solve the magnetic bearing force. The load was applied in the direction of one coordinate axis, both the x and y directions were measured. The bearing currents were measured with separate shunt resistors and voltage meters.

The first task in the measurement process was to find the central position for the rotor. This could be found by mounting the test machine vertically and moving the rotor until the current references in the radial directions were zero. In practice, such a situation is hard to find due to the hysteresis in the magnetic circuits. At every radial coordinate axis, the rotor was moved into a position were the current reference varied in the neighbourhood of zero when an applied force in a positive direction was removed and then an applied force in a negative direction was removed. This position was considered to be the central position. After that the wanted position and eccentricity was tuned from the electronics and measured also by micrometers. All the measurements were done following the same procedure. First, the maximum load was applied to the bearing and then the load was gradually decreased towards zero. In this way, the effect of hysteresis on the slope of force-control current curve was controlled. Thus, hysteresis produces a small offset to the force-control current curve. However, this offset is small compared to the range of interests of this work and the offset is not shown in the results.

2.3.2 Test setup of dynamic inductance measurement

The dynamic inductance measurements were done with the second test machine i.e. the high-speed compressor. In the measurements, the position of the rotor was fixed with mechanical wrenches, and the bearing controller was turned off. However, the position of the rotor was measured from the electronics. The dynamic inductance measurements were done with a single radial magnetic bearing coil. The measurement configuration is shown in Fig 8. A DC-current and a small AC-component of 50 Hz is supplied into the coil. The current is measured by a shunt resistor R_{S} and the voltage over the coil is measured. From the AC-component of the measured voltage the effect of coil resistance is reduced according to Eq. 47.

Thus, the inductive component of the measured voltage is calculated and the dynamic inductance can be solved according to Eq. 47.

$$L_{\mathrm{dyn}} = \frac{\boldsymbol{u}_{\mathrm{AC}} - \boldsymbol{i}_{\mathrm{AC}} R}{j\omega \boldsymbol{i}_{\mathrm{AC}}} \tag{47}$$

where $\boldsymbol{i}_{\mathrm{AC}}$, is the phasor of the AC-current, $\boldsymbol{u}_{\mathrm{AC}}$ is the phasor of the AC-voltage, R_{C} is the resistance of the coil, ω is the angular frequency of the AC-components and L_{dyn} is the dynamic inductance. The measurements were done with DC-currents varying from 0 to 3.3 A. The airgap was fixed to 0.188 mm.

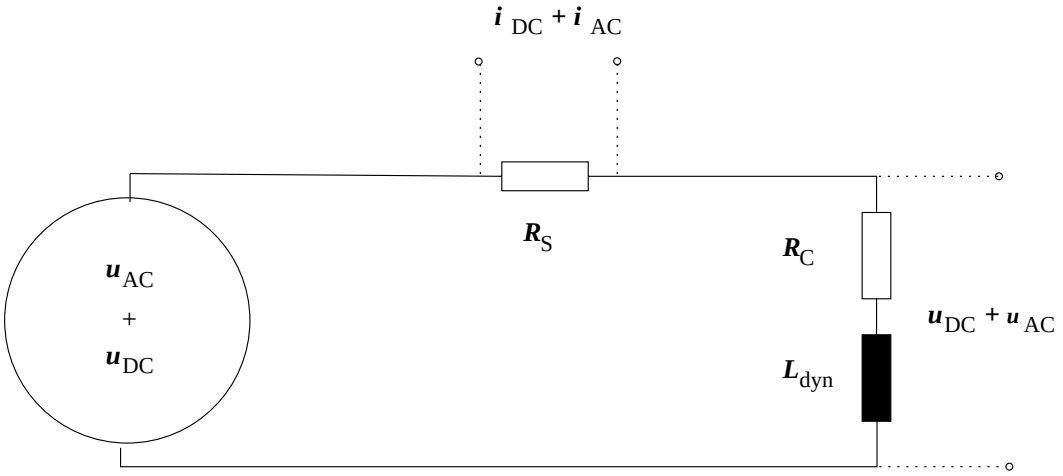

Figure 8: Measurement system of dynamic inductance of radial magnetic bearing coil.

2.3.3 Verification of the finite element calculations

In order to verify the finite element method, the force vs. control current characteristics were measured with two different bias currents. Fig. 9 presents the force measurement of test machine 1 with bias currents of 1.4 A and 2.0 A. In the same figure, the force calculations made by FEM and linear method of Eq. 1 are compared.

Fig. 10 presents the comparison of the measured and calculated forces of test machine 2. In Table 1, the magnetic and geometric air gaps are not equal. The value of the magnetic air gap is estimated so that the measured and calculated forces are almost equal in the linear region. In test machine 1, the difference is estimated as 0.04 mm. In test machine 2, the

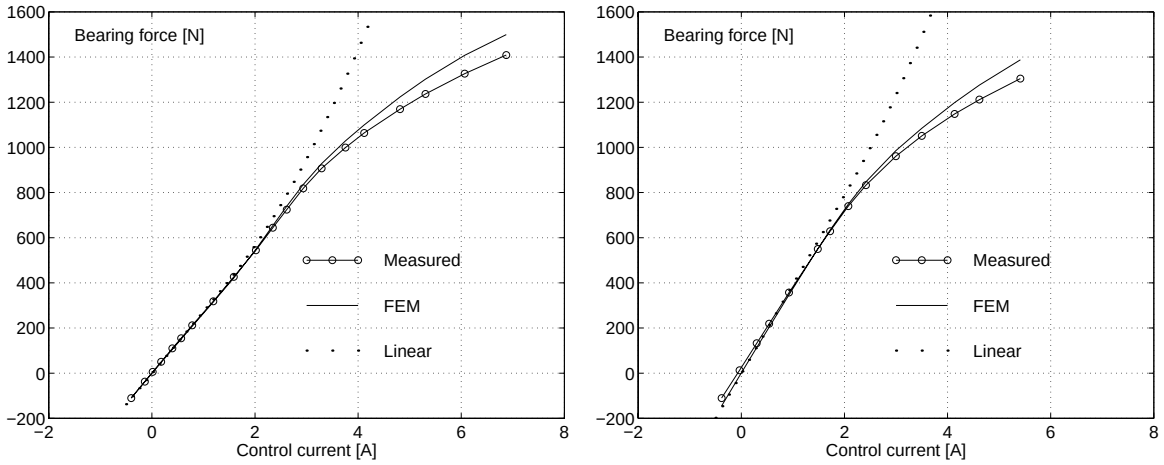

(a) Bias current is 1.4 A.

(b) Bias current is 2.0 A

Figure 9: Force vs. control current characteristics of test machine 1.

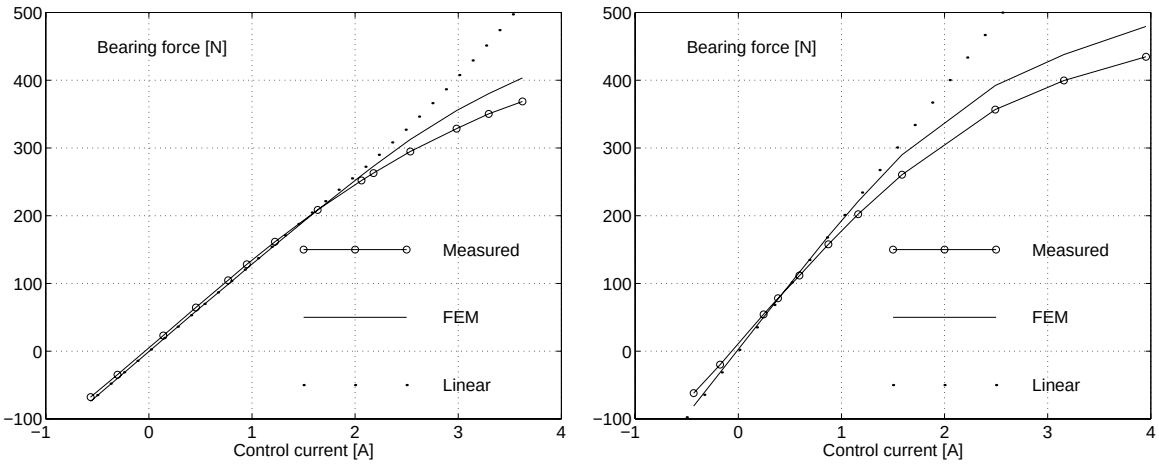

(a) Bias current is 2.0 A. *(b) Bias current is 3.0 A.*

Figure 10: Force vs. control current characteristics of test machine 2.

nonmagnetic layer is estimated to be 0.07 mm. There are some reasons why the geometric and magnetic air gap are not equal. First, when manufacturing the bearing steel sheets by punching the magnetic properties of the sheet may change in a narrow layer. Typically, the nonmagnetic layer due to punching is 0.05-0.1 mm. Secondly, the inner radius of the stator is difficult to measure accurately. The two-dimensional model neglects also the effects of the end-fields. In FEM calculations, the length of the bearing was assumed to be the core length plus two times the radial air gap length. In this work, the main interest is the nonlinear region of the magnetic circuit. Thus, the adjustment of the magnetic air gap can be reasoned. In practice, due to manufacturing tolerances and thermal enlargements, even larger variations of the air gap have to be considered when designing AMBs for series production. Fig. 11 presents the force vs. control current characteristics of test machine 1 with eccentricities of 110 μm and -110 μm. This corresponds to relative eccentricity of 25 % .

Positive eccentricity means that the rotor has been moved in the direction of the bearing force. In the linear region, the difference between the FEM model and the linear method is less than five percent. The difference can be explained by the finite reluctivity of the iron, which is modelled in FEM, but in the linear model reluctivity is assumed to be infinite. As expected, the linear model fails when the magnetic circuit is saturated. These measurements verify that the accuracy of the FEM model in the highly saturated flux densities is about 7 to 8 %. Both methods of the force calculation from a FEM field solution (Eq. 38 and 40) give results within 0.1 %, at relative eccentricity of 25 % and identical results, at zero eccentricity. The accuracy of the FEM model is suitable for the purpose of AMB design.

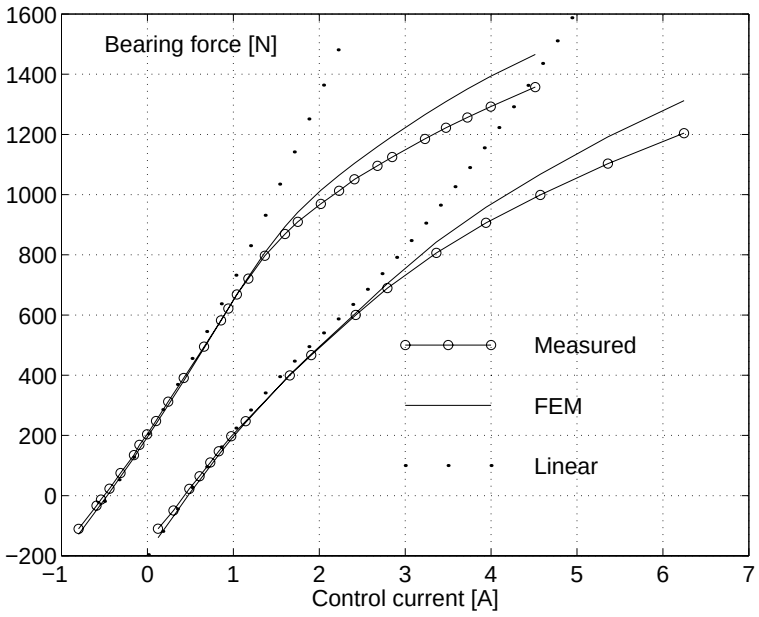

Figure 11: Force vs. control current characteristics of test machine 1 at eccentricities of 110 μm (upper curves) and -110 μm (lower curves) and bias current of 2.0 A.

The same measurements are used for verifying the current and position stiffness calculations. The current stiffness h_{f} is the derivative of the force-control current curve. As the measurements were done by first applying the maximum load and then decreasing the load, the measurements follow the upper range of the hysteresis loop. A single valued monotonic reluctivity curve is used for FEM calculations. This curve is derived from the initial reluctivity curve and does not strictly correspond to the upper curve of the hysteresis loop. However, the hysteresis is small compared to the whole range of reluctivity curve and the comparison between calculated and measured stiffnesses is reasonable.

Fig. 12(a) presents the measured and calculated current stiffnesses of the first test machine, at the bias current of 2.0 A. The deviation between the measured and FEM values is less than ten percent at low values of control current. This deviation is largely caused by the uncertainty of the magnetic airgap. In the saturation region, the deviation is 10-15 percent as expected from the analysis of the force measurements. The linear model of Eq. 1 shows that when the control current is larger than the bias current (the current in the other coil is zero), the current stiffness is no longer constant but increases approximately linearly with the control current and bearing force.

The position stiffness c is measured from the difference of two force-control current curves. In the first one, the rotor is moved 50 μm to the positive direction and 50 μm to the negative direction in the second one. The force difference at every control current is divided by the position difference of the two measurements to calculate the position stiffness at zero

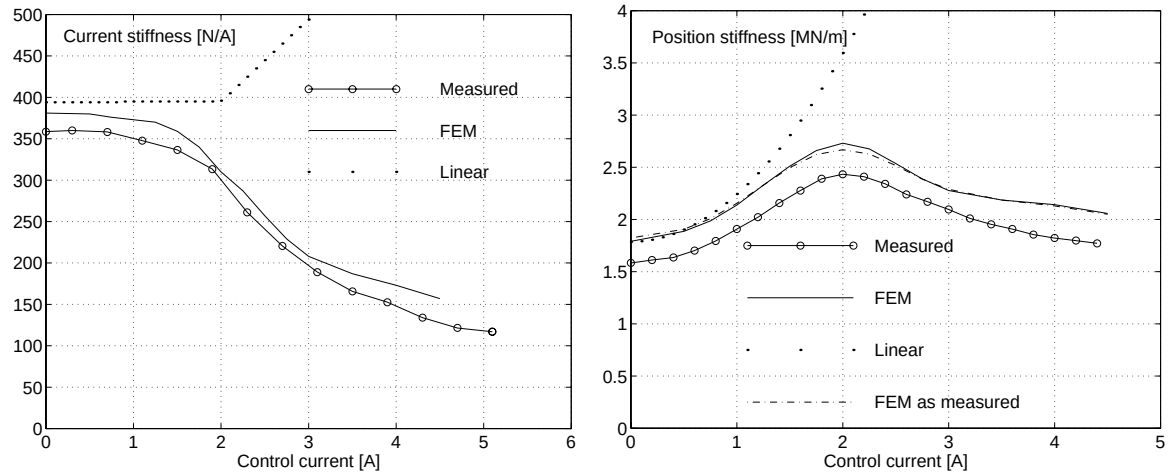

(a) Current stiffness h_{f}. *(b) Position stiffness c.*

Figure 12: Measured and calculated parameters vs. the control current of test machine 1. Bias current is 2.0 A.

eccentricity. However, the position stiffness depends nonlinearly on the displacement of the shaft, as can be seen from Eq. 3. Thus, the method of measurement is not exactly accurate. For this reason, in Fig. 12(b) the measured results with FEM calculations done exactly as in the measurements are compared. In addition, the FEM calculations of the exact position stiffness are compared. As can be seen, the difference between the exact calculated value and the calculated value as measured is almost negligible. The deviation between measured and calculated values are around ten percent.

The dynamic inductance L_{dyn} was measured from the second test machine. In Fig. 13, the comparison between calculated and measured values is shown.

The deviation is at its largest where the magnetic circuit begins to saturate due to the *DC* current. This is due to the hysteresis of the magnetic circuit. As a result, the measured dynamic inductance depends on the amplitude of the *AC* component. During the measurement, the amplitude was chosen as follows. In the linear region of the magnetic circuit, the amplitude was chosen large enough so the measurement cycle would not follow a small minor hysteresis loop. In practice, this means amplitudes of the same size as the *DC* current. This configuration would correspond to the calculation where a single valued monotonic reluctivity curve is used. In the heavily saturated region, the smallest measurable amplitude is used because the effect of hysteresis is negligible. In the region between the two extremes, the amplitude was chosen to be in between the minimum and maximum amplitudes. This caused the measurement cycle to follow an arbitrary minor loop and as the calculations are done with a single valued reluctivity curve, the deviation between measured

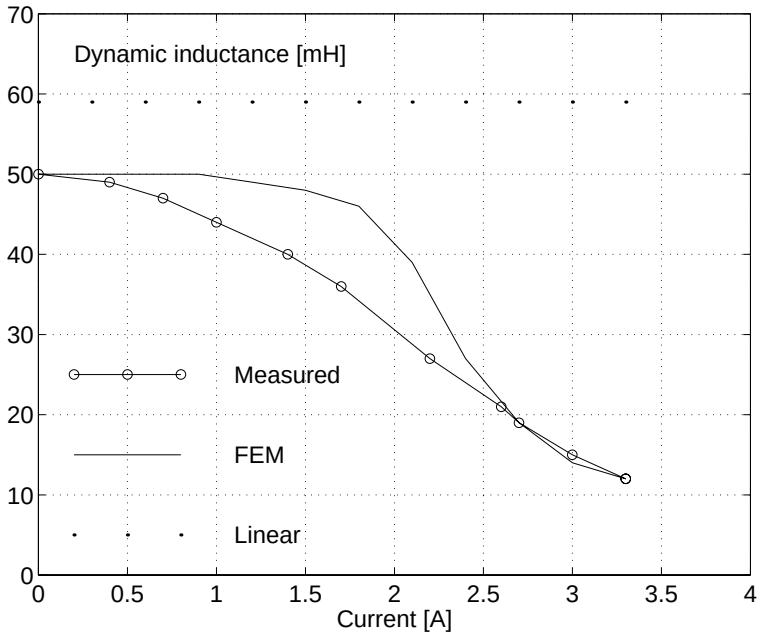

Figure 13: Measured and calculated dynamic inductances L_{dyn} of test machine 2, the air gap is 0.188 mm.

and calculated values is relatively large. However, in this work most interesting is the whole range of the linearised parameters. As can be seen, the agreement between measured and calculated dynamic inductances at the ends of the region is good. Thus, the stationary nonlinear FEM is a suitable method for determining the dynamic inductance of radial active magnetic bearing. The linear model estimates the dynamic inductance to be constant and this value deviates from the measured and FEM values of zero DC-current. This happens because the linear model neglects the magnetomotive force needed to magnetise the iron circuit.

One can conclude that the linear magnetic circuit model does not satisfactorily predict the performance of radial active magnetic bearings. The nonlinear FEM model of the radial AMB is accurate enough in the nonlinear region.

2.4 Linearised parameters in radial AMB

2.4.1 Calculated linearised parameters

In this section, the current stiffness h_{f}, the position stiffness c and dynamic inductance L_{dyn} of test machine 2, calculated by FEM, are presented at several operation points. The stiffnesses are calculated by applying a finite difference either in the currents of the coils or in the position of the rotor and calculating the difference in the force. The calculation is compared with the linear model of Eq. 1.

Fig. 14(a) shows the current stiffness at three bias currents and zero eccentricity as a function of the bearing force. As can be seen, the current stiffness at zero force depends almost linearly on the bias current, as in Eq. 3. At zero force, the difference between linear and FEM model is due to the finite reluctivity of iron in the magnetic circuit and on the other hand the flux fringing in the neighbourhood of the airgap. The effective airgap area is somewhat larger than the geometric airgap and the effect of finite reluctivity and the flux fringing almost cancel each other at zero force. Due to the saturation, the current stiffness drops and is almost independent of the bias current at large bearing loads. As expected, the linear model totally neglects the saturation.

Fig. 14(b) presents the position stiffness c at the same operation points as in Fig. 13. At zero force, the position stiffness depends quadratically on the bias current as expected from Eq. 3. However, the position stiffness saturates and decreases with an increasing bearing force. At larger bias currents, the position stiffness remains somewhat larger also at high bearing forces. This is because the perpendicular magnets have an effect on the position

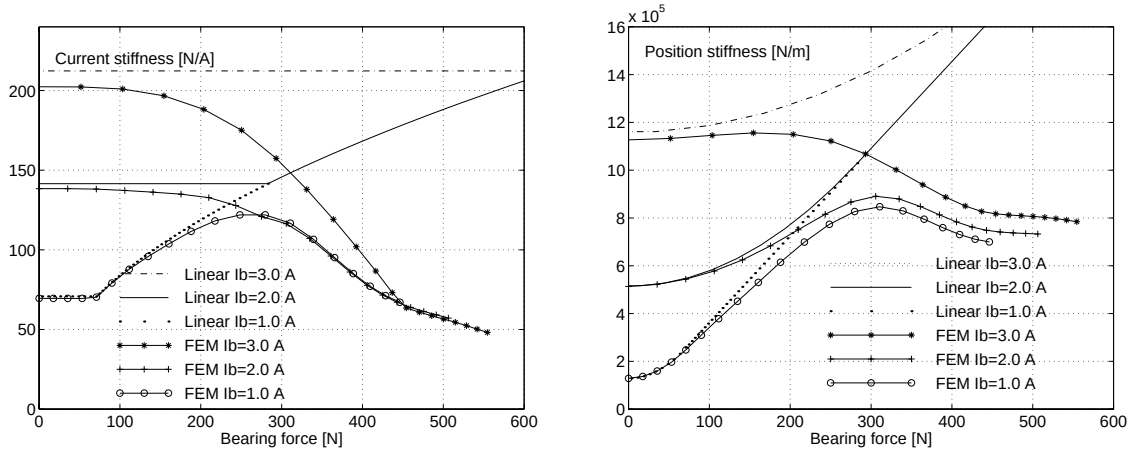

(a) Current stiffness h_{f}. *(b) Position stiffness c.*

Figure 14: Calculated parameters of test machine 2 as a function of the bearing force at three bias currents and zero eccentricity.

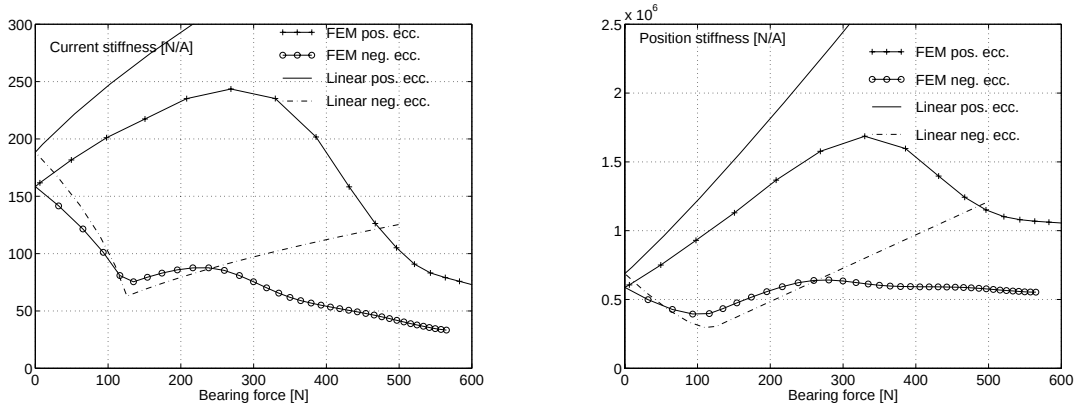

(a) Current stiffness h_f. *(b) Position stiffness c.*

Figure 15: Calculated parameters of test machine 2, at the bias current of 2.0 A and eccentricities of 275 μm and -275 μm.

stiffness. Thus, the larger the bias current in the perpendicular magnets is, the larger the position stiffness at high bearing loads.

In Fig. 15(a) and Fig. 15(b), the current stiffness h_f and the position stiffness c are shown as a function of the bearing force, at two eccentricities and with the bias current of 2.0 A. When the control current is less than the bias current, the current stiffness is not constant anymore as it is at zero eccentricity when neglecting the saturation. With a positive eccentricity, the current stiffness increases as the flux density increases in the magnet of the smaller air gap, and flux density decreases in the magnet of the larger air gap. With the negative eccentricity the situation is opposite. The increment of the position stiffness, when the bearing is loaded, is larger with the positive eccentricity than with the negative eccentricity. The eccentricity of 275 μm corresponds to relative eccentricity of 50 %.

Fig. 16(a), 16(b) presents the dynamic inductance L_dyn of the first test machine. The dynamic inductance is calculated for the positive magnet at the bias current of 1.0 A, 2.0 A and 3.0 A. The inductance is almost independent of the bias current, but drops, due to the saturation as the bearing force and current of the magnet increase. In Fig. 16(a), 16(b) no end winding effects are taken into account.

So, both the current stiffness and position stiffness decrease as the bearing force increases. The ratio of the current and position stiffness is also an important factor when considering the control system. Fig. 16(a), 16(b) presents this ratio at the bias currents of 1.0A, 2.0 A, 3.0 A and zero eccentricity, calculated with FEM. As can be seen, this ratio decreases as the bearing load increases. Thus, at certain load, the designed control system does not operate satisfactorily anymore and the stability can be lost.

By calculating the linearised parameters at different operation points, the designer can

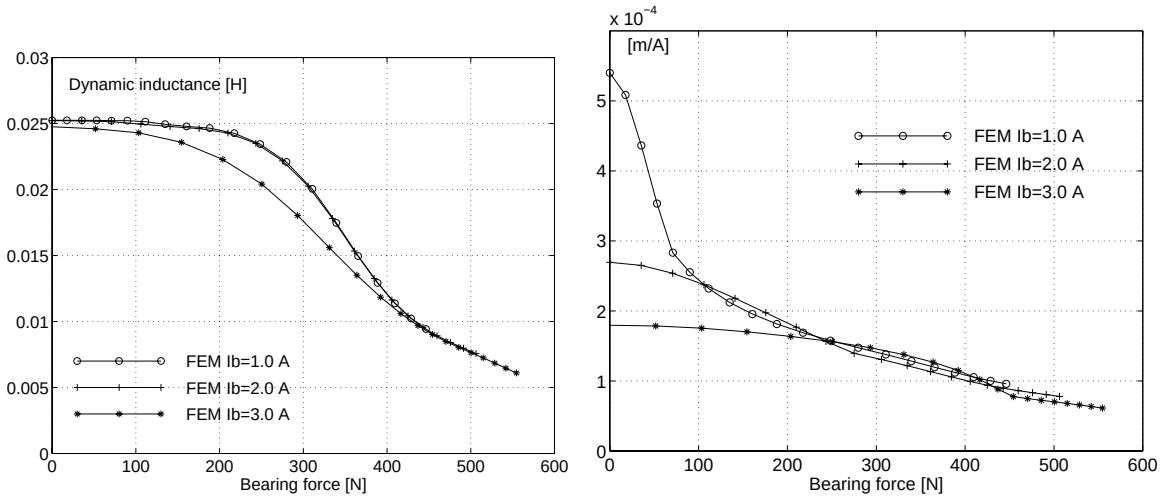

(a) Dynamic inductance L_{dyn}.

(b) Ratio of the current stiffness and position stiffness.

Figure 16: Dynamic inductance and the stiffness ratio of test machine 2 at the bias currents of 1.0 A, 2.0 A , 3.0 A and zero eccentricity as a function of the bearing force.

simulate the performance of the designed control system with the dynamic model of Eq. 6 and get an estimation of the performance of the AMB. Anyhow, the wide variation of the linearised parameters at the operation range of the bearing should be noticed. For test machine 2, the current stiffness has values from 250 to 60 N/A, position stiffness from 0.3E6 to 1.6E6 N/m and the dynamic inductance from 25 to 8 mH at a bias current of 2.0 A.

2.4.2 Effect of the parameter variations on the bearing dynamics

As was seen in the previous section, the parameters of the magnet actuators change, due to eccentricity and saturation of the magnetic circuit. Other reasons for parameter variations could be, for example, the temperature differences in the stator and rotor and centrifugal stresses in rotor laminations at high rotational speeds. These phenomena change the airgap of the bearing and therefore the parameters change. Thus, the robustness of the controller against these variations is of primary importance, both for stability and for performance. In this section, the effect of the variation of actuator parameters due to eccentricity and nonlinearity of magnetic circuit on the bearing dynamics are studied. The emphasis is to analyze the effects, not to synthesize appropriate controllers. This study is divided into three categories. First, one dimensional case is studied. Second, rigid body modes of nonrotational rotor and last the bending modes of the rotor are studied. In this section, test machine 2 is studied.

One dimensional effects

In this case, the AMB system of a pointmass is studied. The simple case clearly demonstrates the effect of the magnetic saturation on the bearing dynamics and gives the reader an intuitive understanding of the effect. The controller is PID-controller with a second order low pass filter, whose parameters are shown in App. A.1. The pointmass corresponds to the reduced mass of the test machine two in D-end bearing.

In the transfer functions of the point mass system the following actuator model is used

$$\Delta F_{\mathrm{b}} = \boldsymbol{h}_{\mathrm{f}}^{\mathrm{T}} \Delta \boldsymbol{i}_{\mathrm{c}} + cx \tag{48}$$

$$\Delta \boldsymbol{u}_{\mathrm{c}} = s\boldsymbol{L}_{\mathrm{dyn}} \Delta \boldsymbol{i}_{\mathrm{c}} + \boldsymbol{R} \Delta \boldsymbol{i}_{\mathrm{c}} + s\boldsymbol{h}_{\mathrm{f}} x \tag{49}$$

$$\boldsymbol{h}_{\mathrm{f}} = [h_{\mathrm{fu}} \;\; h_{\mathrm{fd}}]^{\mathrm{T}} \tag{50}$$

$$\boldsymbol{L}_{\mathrm{dyn}} = \begin{bmatrix} L_{\mathrm{dynu}} & 0 \\ 0 & L_{\mathrm{dynd}} \end{bmatrix} \tag{51}$$

where h_{fu} and h_{fd} are the current stiffnesses of the upper and lower magnets, L_{dynu} and L_{dynd} are the dynamic inductances of the upper and lower magnets. c is the position stiffness, $\boldsymbol{R}$ is the diagonal resistance matrix. $\Delta \boldsymbol{u}_{\mathrm{c}}$ and $\Delta \boldsymbol{i}_{\mathrm{c}}$ are the control voltage vector and control current vector. m is the reduced mass of the rotor corresponding to D-end bearing.

Fig. 17(a) presents the Nyquist diagrams of the one dimensional system with the nominal bias current of 2.0 A. Only the positive frequnecies of the diagram are drawn. The fact that AMB is open loop unstable is clearly seen as the imaginary part of the diagram is negative at low frequencies. For the closed loop stability one encirclement anticlockwise around point

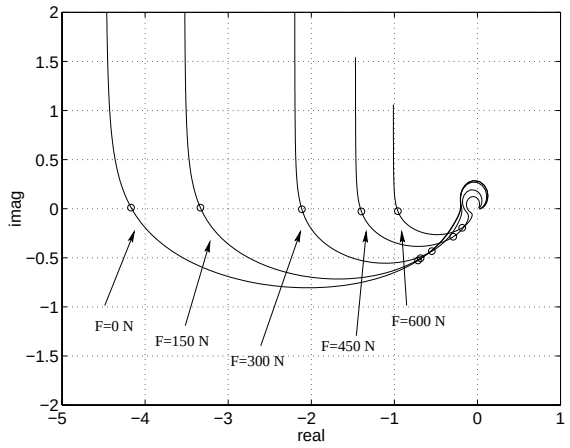

(a) The Nyquist diagram at the bearing loads of 0, 150, 300, 450 and 600 N. The circles are plotted at the frequencies of 10 and 100 Hz. The bias current is 2.0 A.

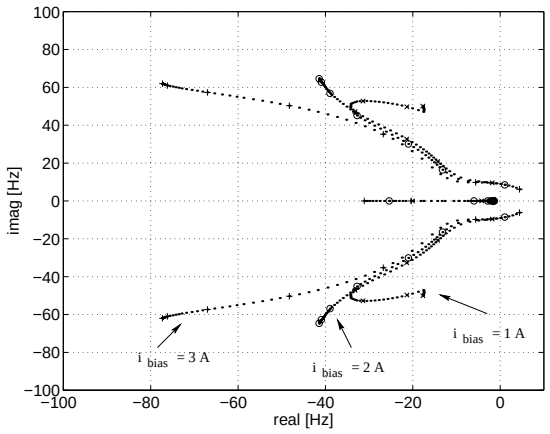

(b) The root locus diagram of the closed loop system as a function of the bearing force. The diagram are plotted at the bias currents of 1.0 A, 2.0 A and 3.0 A.

Figure 17: Diagrams of the one dimensional model corresponding to the D-end of test machine 2.

-1 is necessary. The diagrams are plotted at the bearing loads of 0, 150, 300, 450 and 600 N. The circles in the diagram are at the frequencies of 10 and 100 Hz. It is seen that the system remains stable until the bearing load is around 600 N. As the bearing load is increased, the gain of the loop decreases as the magnetic circuit saturates and the bearing parameters change. The primary cause is the decrement of the ratio of the current and position stiffness. The linearised model estimates instability, when the inverse of the ratio of the current and position stiffness is as large as the proportional gain of the controller.

Fig. 17(b) shows the root locus diagrams of the closed loop as a function of the bearing force, with bias currents of 1.0, 2.0 and 3.0 A. The poles are adequately damped until the stiffness ratio is in the neighborhood of the corresponding inverse of the proportional gain. As soon as the load is so large that the current flows only in the other coil, the system behavior is almost independent of the bias current. The main difference is that at high bias currents the position stiffness remains higher at high loads. This happens because the magnets of the y-direction have a small effect on the position stiffness of the x-direction. Thus, the stability limit of the static force is lower at higher bias currents.

Rigid body mode effects

In this section, the rigid body modes of one coordinate plane are studied. It means that the nonrotational rotor is considered and the gyroscopic coupling is neglected. First, two special cases of bearing load combinations are studied. The bearing load is applied to either

the center of mass (CM) or to the D-end bearing. If the load is at the CM, the bearing loads are similar at both ends of the rotor and the bearing parameters are the same. If the load is at the D-end, only the parameters of the D-end bearing change. The controller is PID-controller with 2nd order low pass filters and a small cross coupling between the drive end and the nondrive end channels. The parameters of the controller and the rotor model are presented in Apps. A.2, B.1.

The state space model of the system can be easily formed from the rotor model of Eqs. $8 \cdots 14$ and from the following actuator model.

$$\Delta \boldsymbol{F}_{\mathrm{b}} = \boldsymbol{h}_{\mathrm{f}}^{\mathrm{T}} \Delta \boldsymbol{i}_{\mathrm{c}} + c\boldsymbol{p} \tag{52}$$

$$\Delta \boldsymbol{u}_{\mathrm{c}} = s\boldsymbol{L}_{\mathrm{dyn}} \Delta \boldsymbol{i}_{\mathrm{c}} + \boldsymbol{R} \Delta \boldsymbol{i}_{\mathrm{c}} + s\boldsymbol{h}_{\mathrm{f}} \boldsymbol{p} \tag{53}$$

$$\boldsymbol{h}_{\mathrm{f}}^{\mathrm{T}} = \begin{bmatrix} h_{\mathrm{fuD}} & h_{\mathrm{fdD}} & 0 & 0 \\ 0 & 0 & h_{\mathrm{fuN}} & h_{\mathrm{fdN}} \end{bmatrix}, \boldsymbol{c} = \begin{bmatrix} c_{\mathrm{D}} & 0 \\ 0 & c_{\mathrm{N}} \end{bmatrix} \tag{54}$$

$$\boldsymbol{L}_{\mathrm{dyn}} = \begin{bmatrix} L_{\mathrm{dynuD}} & 0 & 0 & 0 \\ 0 & L_{\mathrm{dyndD}} & 0 & 0 \\ 0 & 0 & L_{\mathrm{dynuN}} & 0 \\ 0 & 0 & 0 & L_{\mathrm{dyndN}} \end{bmatrix}, \boldsymbol{p} = [x_{\mathrm{D}} \;\; x_{\mathrm{N}}]^{\mathrm{T}} \tag{55}$$

where the linearised parameters are the same as in Eqs. $50 \cdots 51$ with the exceptions that the parameters may have different values at D- or N-end of the machine. $\Delta \boldsymbol{F}_{\mathrm{b}}$ is the vector of control forces in both ends of the rotor.

Fig. 18(a) presents the root locus diagram of the closed loop system as a function of the bearing force, at the nominal bias current of 2.0 A, when the bearing load is applied to the CM. In this case, the rigid modes remain the same and the poles of the cylindrical mode move towards origo. This is equivalent to the one dimensional case. The conical mode remains well damped until the gain of the control loop is so low that the eigenfrequency of the mode is in the neighborhood of the integrator bandwidth. The load at which this linear system becomes unstable is 455 N at both ends. It is worth noticing that the cross coupling in the controller between N- and D-ends decrease the gain of the control loop, thus without cross coupling the system would tolerate even higher static forces. However, overall performance, considering resonances and damping, is superior with the cross coupling included.

In Fig. 18(b) the load is applied only to the D-end. The poles remain properly damped through a larger range than in the previous case. As the bearing system becomes asymmetrical, due to this loading, the rigid body modes are conical modes with asymmetrical amplitudes in the N- and D-end. At this loading, a larger static force range is achieved than in the previous case. This happens due to the fact that the conical mode is stabilized by the nominal N-end bearing. The stability limit is 555 N at D-end. These stability limits are purely calculational and based on this linearized model.

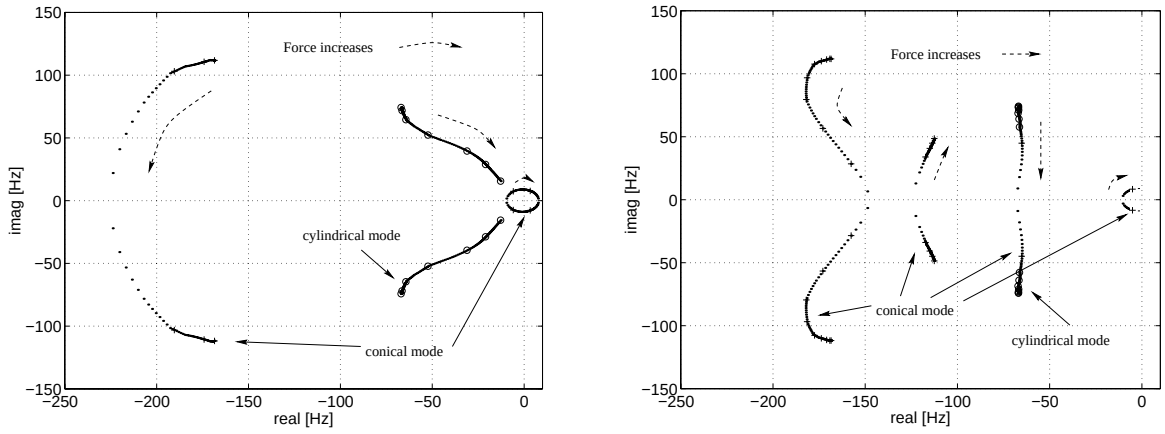

(a) The bearing load is applyed to the center of mass.

(b) The bearing load is applyed to the D-end.

Figure 18: Root locus diagrams of test machine 2 with respect to a bearing load. The bias current is the nominal 2.0 A.

Fig. 19(a) presents the root locus diagram as a function of the eccentricity at the bias current of 2.0 A. The control currents are chosen so that the bearing force is zero at every eccentricity. The relative eccentricity is from zero to 60 percent. In practice, larger eccentricities are unlikely due to the fact that the retainer bearings limit the mechanical airgap. As can be seen, eccentricity has a small increasing effect on the resonance frequency of the bearing system. This is due to an increment in the ratio of current and position stiffness and in the current stiffness. A more pronounced effect of the eccentricity is the reduced damping of the system. This is almost solely due to the variation of the dynamic inductance. The majority of the current stiffness, in an eccentric case, is from the magnet where the airgap is smaller. Then the dynamic inductance of that magnet is larger as well. This causes additional phase lag in the current control circuit which can be seen in the closed loop poles. However, at large eccentricities, the system is still quite well damped. This effect can be diminished by increasing the gain of the current control loop.

Fig. 19(b) shows the root locus diagram as a function of the bearing load, at the relative eccentricity of 50 percent. The bearing force range is from -550 N to 650 N. The eccentricity is in the direction of positive load. In the negative loads, the behavior of the system is dominated by the magnet with large airgap. Thus, both the stiffnesses have relatively small values and the imaginary parts of the poles are quite small. Also, the inductance is relatively low. At zero bearing force, the poles are not equally damped as in the nominal position as was seen in Fig. 19(a). At positive loads, the performance is dominated by the magnet with a small airgap. Thus, the stiffnesses are large resulting in a large resonance frequency and the inductance is large causing the damping to be at its minimum. Above 260 N the

magnetic circuit begins to saturate, thus lowering the resonance frequency. The dynamic inductance drops from 40 mH at 260 N to 15 mH at 400 N resulting in an increment in the damping of the poles. The stability limits are -400 N and 510 N.

These special cases do not justify to draw conclusions about stability and performance at arbitrary bearing load and eccentricity combinations. However, these cases indicate the possibility to extend the operation range of the AMB system into the saturation region with the simple linear controller topology.

Bending mode effect

Fig. 20 shows stiffness range of the D-end bearing when the bearing loads at the both ends vary from zero to 400 N. As the bearing force increases, the magnitude of the stiffness decreases because the magnetic circuit saturates. Moreover, the phase of the stiffness varies several tens of degrees, depending on the frequency, as the force is increased. At the higher frequencies, this is due to the decrement of the dynamic inductance as the bearing force is increased. The range from 600 Hz to 1400 Hz is especially critical as the first bending mode of high-speed machines usually lies in that range. For example, at 1190 Hz, the phase varies from -200 degrees close to -180 degree as the force increases from zero to 400 N. In this controller, a low pass filter is used to drop the phase of the stiffness curve below -180 degrees at a frequency which is lower than the first bending critical speed. This stabilizes the first bending mode. As the force is increased, the phase of the actuator rises and the phase margin can be lost and the bending mode is destabilized. In this case, the first bending mode (1192 Hz) is almost destabilized. On the other hand, in the model the internal damping of

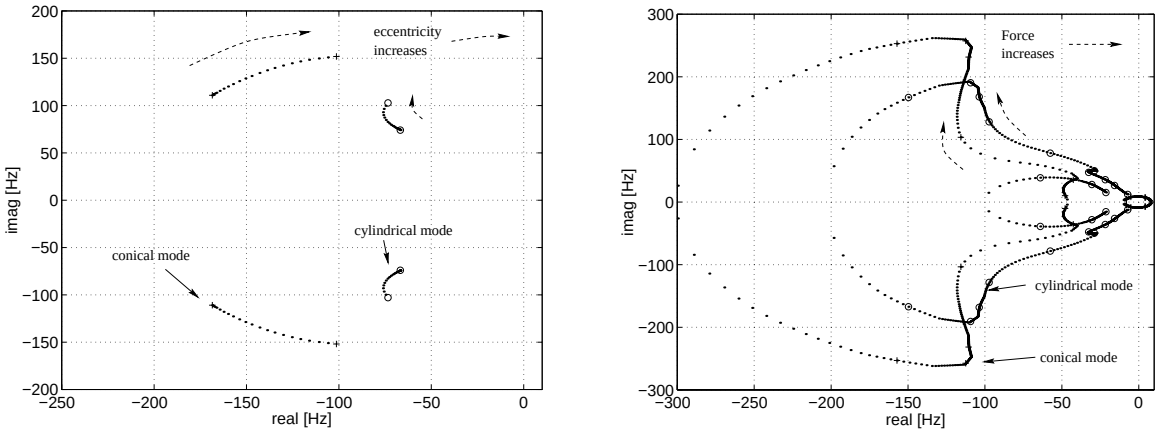

(a) The relative eccentricity varies from zero to 60 %. The bearing load is zero.

(b) The bearing load applyed to the CM varies from -550 N to 650 N. The relative eccentricity is 50 %.

Figure 19: Root locus diagrams of test machine 2. The bias current is the nominal 2.0 A.

the rotor is neglected, which in practise increases the stability margin. Also, the magnitude of the stiffness is higher at larger bearing forces at high frequencies. This is also due to the strong nonlinear property of dynamic inductance.

The linearized parameters for the dynamic model of AMBs at different operation points can be accurately determined by FEM. Thus, the designer of the control system has a set of parameters at every operation point and he can estimate the performance of the controller at different bearing loads, eccentricities and air gaps and check the local stability in the neighborhood of the operation point.

For the design point of view, one can conclude that the choice of the bias current is quite free and almost independent of the static load capacity. It is not necessary to use a large bias current to achieve large stiffness either, as this can be accomplished by the controller. On the other hand, if a large bias current is chosen, the current stiffness varies at a large range when the magnetic circuit saturates. This is not preferred when designing the control system. In order to minimize the current stiffness variation, one should choose the bias current in such a way that at zero bearing force the current stiffness is not larger than the maximum current stiffness. This maximum is approximately at the point where the flux density at the tooth (and airgap) corresponds to the flux density value where the material begins to saturate. In addition, in applications where the low-pass filters are used to stabilize the rotor-bending modes, a large bias current increases the phase of the control loop already at small DC-loads, thus endangering the stability of the bending mode. On the

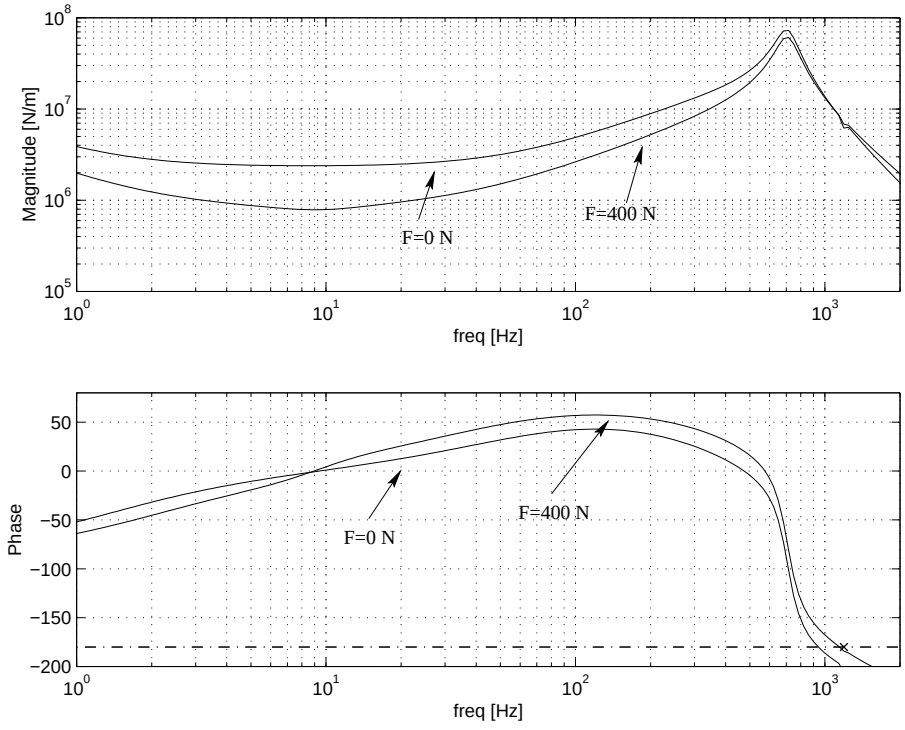

Figure 20: Stiffness curves of the D-end bearing. The bearing force is 0 N and 400 N.

other hand, if one chooses a small bias current value, the position stiffness at zero bearing force is small, compared with the maximum value of the position stiffness. Thus, the classical way of choosing the bias current to produce an airgap flux density which is half of the flux density where the material begins to saturate is valid and an appropriate way. However, it should be noticed that bearing system is not very sensitive to the bias current value as long as the bias flux density is at a reasonable range 0.3 T$< B_{\mathrm{bias}} <$0.6 T. Also, when the bearing should operate at the saturation region, the system is almost indifferent to the bias current value, assuming the bias current is within a reasonable range.

Another important design factor which affects the linearized parameters is the airgap. In series production of AMB machines, one should choose the radial length of the airgap in such a way that the relative variations of the airgap are reasonable. The main sources of the variations are, for example, thermal enlargements, manufacturing tolerances and centrifugal stresses caused by high rotational speeds. As can be seen from Eq. 2 the current stiffness is inversely proportional to the square of the airgap and the position stiffness to the cubic of the airgap. The dynamic inductance is proportional to the inverse of the airgap. The variations of the airgap should be less than ten percent. Then the variation of the current stiffness is less than twenty percent and the variation of the position stiffness less than thirty percent at the nominal point. It should be noticed that in the saturation region the iron part of the magnetic circuit plays a larger role than in the linear region. Thus, the effect of airgap variations is at its largest in the linear region.

In this analysis, the optimal topology of the controller, when extending the operation range into the saturation region, is left as an open question. However, as the main effects are the gain variations, a relatively simple gain scheduling controller would result in a wide operation range of the AMB system. The gain of the controller would depend on the control current as well as the current feedback coefficient.

Another possibility to reduce the effects of the nonlinearities would be a flux controller. This can be realised using a simple flux measurement coil [Brunet 1988], [Hara et al. 1996].

2.5 Cross coupling in radial AMB

2.5.1 Introduction to cross coupling phenomena

By cross coupling it is meant that a control action in x-direction also causes a force in the y-direction. In order to realize the importance of the cross coupling in the magnetic bearing and high-speed rotor system, the equation of motion of a rigid high-speed rotor is studied.

$$\boldsymbol{M}_{\mathrm{rot}}\ddot{\boldsymbol{q}}_X + \Omega\boldsymbol{G}_{\mathrm{rot}}\dot{\boldsymbol{q}}_Y + \boldsymbol{K}_{\mathrm{stiff}}\boldsymbol{q}_X = 0 \tag{56}$$

$$\boldsymbol{M}_{\mathrm{rot}}\ddot{\boldsymbol{q}}_Y - \Omega\boldsymbol{G}_{\mathrm{rot}}\dot{\boldsymbol{q}}_X + \boldsymbol{K}_{\mathrm{stiff}}\boldsymbol{q}_Y = 0 \tag{57}$$

where $\boldsymbol{M}_{\mathrm{rot}}$ is the mass matrix, $\boldsymbol{G}_{\mathrm{rot}}$ describes the gyroscopic coupling. The solution of this equation is stable if the stiffness matrix $\boldsymbol{K}_{\mathrm{stiff}}$ is positive definite and symmetric. Thus, when there are diagonal positive bearing stiffnesses the system is stable with any positive damping. However, when there is cross coupling between the bearing forces (or any other cross coupling) the stability can be lost and one has to study the eigenvalues of the system to guarantee stability. This problem is well known for people involved in rotordynamics of turbomachinery, where the origin can be, for example, fluid pressure forces around a turbine wheel, centrifugal impeller or a fluid seal [Vance 1988]. In high-speed technology, the compressors manufactured so far have been of low pressure ratio and the radial compressor forces are relatively low [Antila et al. 1996]. Thus, cross coupling due to the compressor forces are negligible.

When designing an AMB control system, it is usually assumed that the radial channels in x and y-direction interfere with each other only through the gyroscopic coupling at high speeds. This is an almost valid assumption as far as the bearing magnets operate in the neighborhood of the nominal point, that is with relatively low control currents and low eccentricities. Thus, the control design process is usually performed assuming the system to have negligible cross coupling in xy-plane and afterwards checking the cross coupling effects, such as gyroscopic coupling. In the applications where the cross couplings are small, a control topology without cross coupling the x- and y-planes produces, if not totally optimal, at least satisfactory results. However, when extending the operation range into the saturation region, the cross coupling between the x and y channels may become significant. This would be undesirable from the control point of view, because control in x-direction would also cause an unmodelled force in y-direction.

In this study, the origin of the cross coupling is visualised by field plots. The effect of the operation point on the cross coupling parameters is studied, that is the cross coupling of the current to force transfer function and the cross coupling of the position stiffness. Based on these studies, the importance of cross coupling phenomena is deduced. Finally, some facts

to aid the design process of the magnetic bearings are concluded. The linearised parameter matrices in one end of the machine are

$$\boldsymbol{L}_{\mathrm{dyn}} = \begin{bmatrix} L_{\mathrm{dyn11}} & \cdots & L_{\mathrm{dyn14}} \\ \vdots & \ddots & \vdots \\ L_{\mathrm{dyn41}} & \cdots & L_{\mathrm{dyn44}} \end{bmatrix}, \boldsymbol{R} = \begin{bmatrix} R_1 & \cdots & 0 \\ \vdots & \ddots & \vdots \\ 0 & \cdots & R_4 \end{bmatrix} \tag{58}$$

$$\boldsymbol{h}_{\mathrm{f}}^{\mathrm{T}} = \begin{bmatrix} h_{\mathrm{fx1}} & \cdots & h_{\mathrm{fx4}} \\ h_{\mathrm{fy1}} & \cdots & h_{\mathrm{fy4}} \end{bmatrix}, \boldsymbol{c} = \begin{bmatrix} c_{\mathrm{xx}} & c_{\mathrm{xy}} \\ c_{\mathrm{yx}} & c_{\mathrm{yy}} \end{bmatrix} \tag{59}$$

where $\boldsymbol{R}$ is the diagonal resistance matrix, $\boldsymbol{L}_{\mathrm{dyn}}$ is the 4x4 dynamic inductance matrix, $\boldsymbol{h}_{\mathrm{f}}$ is the 2x4 current stiffness matrix, $\boldsymbol{c}$ is the 2x2 position stiffness matrix,

So far, only the classical NNSSNNSS pole configuration, usually used in conventional eight pole bearings, is considered. In this section, the NNSS and NSNS pole orders are compared. It should be noticed that the saturation effects on the parameters and dynamics presented in the previous section are qualitatively similar for both configurations. The main difference is that the saturation happens at different bearing loads depending on the geometry of the bearing and the pole configuration. Fig. 21 presents the bearing force of test machine 2 with bias-current of 2.0 A in both x- and y-directions. Both NNSS and NSNS pole configurations are shown. Two cases for both configurations are shown. In the first one, the solid shaft of the bearing is modeled with solid iron corresponding to a nonrotational rotor. The second one corresponds to a rotational rotor. In this case, the shaft is modeled as air because when the rotor rotates eddy currents push the flux out of the solid shaft. The figures are made in such a way that the control currents in x- and y-direction are equal at the corners of the force curves. The curves correspond to maximum currents of 3.5 A, 5.0 A, 6.5 A and 8.0 A.

Fig. 21 clearly demonstrates the superiority of the NSNS -pole configuration over NNSS -configuration. At small bearing loads, the force curves remain square and the pole configurations have identical properties. In NNSS configuration for nonrotational rotor, there is some cross coupling already at maximum currents of 5.0-6.5 A. The situation becomes more serious for rotational rotor. On the other hand, in the NSNS -configuration the cross coupling remains small also for rotational rotor. The reason can be demonstrated by the field plots of the bearing.

Fig. 22 presents the equipotential lines of vector potential ($\boldsymbol{a}_1$) of both configurations for rotational rotor. The currents of the operation point are 4.0 A and 6.0 A in the positive x and y coils, respectively. Also, the corresponding control fields of the operation point are presented. These control flux density plots ($\Delta\boldsymbol{B}_{\mathrm{c}}$) are made by adding a small control current to the x coil current of the operation point and calculating the vector potential ($\boldsymbol{a}_2$). The control flux density can be calculated from the difference of these solutions

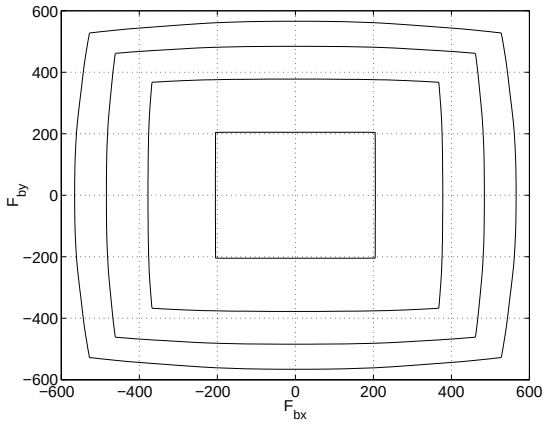

(a) NNSS -pole configuration, shaft modeled as iron.

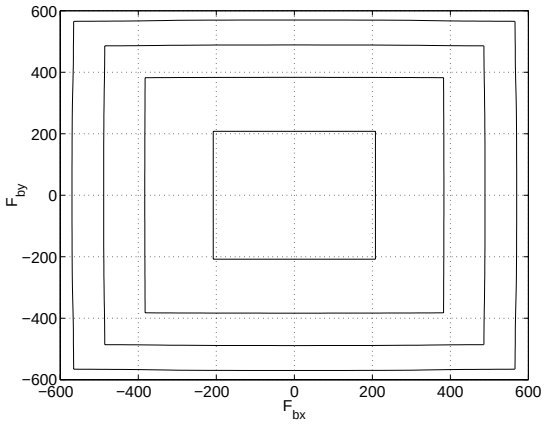

(b) NSNS -pole configuration, shaft modeled as iron.

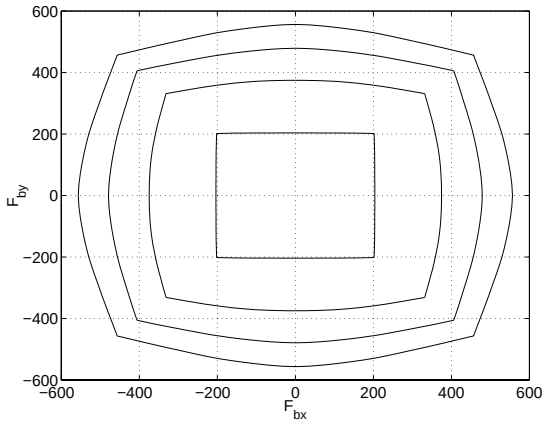

(c) NNSS -pole configuration, shaft modeled as air.

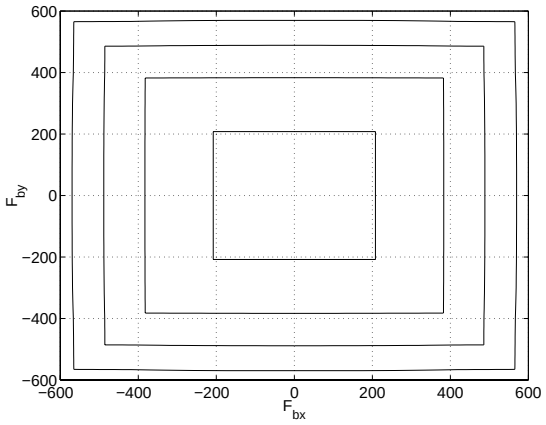

(d) NSNS -pole configuration, shaft modeled as air.

Figure 21: Curves of the tip of the force vector. The curves are drawn in such a way that the control current is constant (minimum or maximum) in one direction and in the other direction the control current varies from the minimum to the maximum value. The curves are drawn for test machine 2 and correspond to absolute maximum control currents of 1.5 A, 3.0 A, 4.5 A and 6.0 A. Eccentricity is zero and the bias-current is 2.0 A.

($\Delta \boldsymbol{B}_\mathrm{c} = \nabla \times (\boldsymbol{a}_2 - \boldsymbol{a}_1)$). Fig. 22 shows that the stator yoke and the rotor lamination are already quite saturated with the above currents in NNSS configuration. Thus, the control flux cannot easily flow through these parts anymore. A part of the control flux flows through the teeth of the negative y-magnet and another part through the other tooth of the positive y-magnet. However, this control flux density is opposite to the flux density of the operation point and the net effect is not only increasing force in x-direction, but also the decreasing force in y-direction. In the NSNS -configuration, the flux flows quite evenly through poles and the magnetic circuit is not severely saturated. The control flux does not flow through the positive y-magnet and the cross coupling is negligible.

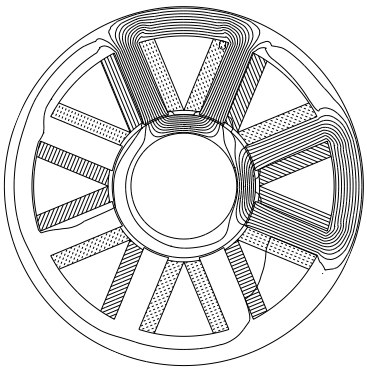

(a) Field plot of the operation point, NNSS -pole configuration, shaft modeled as air.

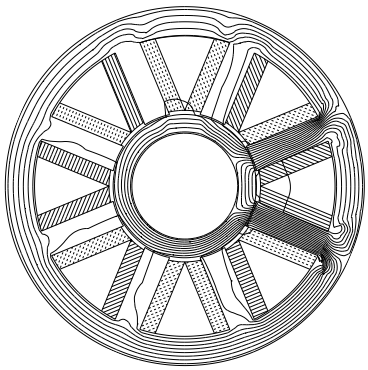

(b) Control field plot, NNSS -pole configuration, shaft modeled as air.

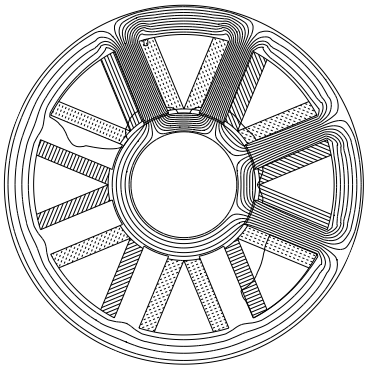

(c) Field plot of the operation point, NSNS -pole configuration, shaft modeled as air.

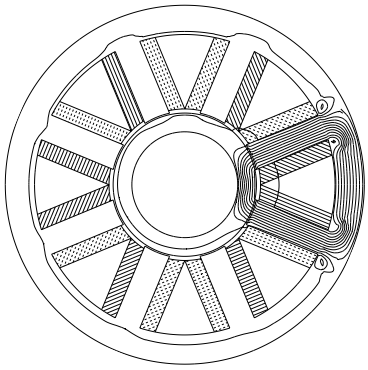

(d) Control field plot, NSNS -pole configuration, shaft modeled as air.

Figure 22: Cross section of test machine 2. The equipotential lines of the vector potential of the operation point and the control field. The currents of the operation point are 4.0 A and 6.0 A in positive x- and y-coils, respectively.

The benefits of the NSNS-configuration is obvious, when the number of poles in the stator and rotor yokes are studied. The number of poles is double the number of the NNSS-configuration. Therefore, the yokes can be made thinner in NSNS-configuration, still retaining the electromagnetic properties. This is an important aspect for the sake of the high-speed technology. One of the major measures determining the bending critical speeds of the rotor, is the diameter of the solid shaft inside the rotor lamination of the radial bearing. Because the NSNS-configuration allows the rotor lamination to be made thinner, the designer has a greater latitude to adjust the bending critical speeds.

2.5.2 Cross coupling parameters

Fig. 23 presents the ratio of cross coupling position stiffness and diagonal position stiffness as a function of control currents in x- and y -direction. For NNSS -configuration, the ratio is positive. Thus, a small displacement in positive x-direction not only increases the force in x-direction, but also decreases the force in y-direction. The absolute value of the maximum is 25 percent at the current of 6.5 A in the positive y-coil. NSNS -configuration shows only maximum amplitude of about 3 percent for position stiffness ratio.

It turns out that the cross coupling in the position stiffness has neglible effect on the bearing dynamics. This can be reasoned when studying the equation of motion of a pointmass in Laplace domain.

$$(s^2\boldsymbol{M} - \boldsymbol{c})\boldsymbol{p}^{\mathrm{T}} = \boldsymbol{h}_{\mathrm{f}}^{\mathrm{T}}\Delta\boldsymbol{i}_{\mathrm{c}} + \boldsymbol{F} \tag{60}$$

$$\boldsymbol{p} = [x\ y]^{\mathrm{T}} \tag{61}$$

where $\boldsymbol{M}$ is the diagonal mass matrix of the pointmass, $\boldsymbol{c}$ is the position stiffness matrix, $\boldsymbol{h}_{\mathrm{f}}^{\mathrm{T}}$ is the current stiffness matrix and $\boldsymbol{F}$ is the force vector due to any other forces. For a properly designed AMB system, the contribution from the current stiffness is dominant, especially at high frequencies. From Eq. 60 it is seen that the position stiffness components are negligible compared to the diagonal mass matrix components already at relatively low frequencies. For test machine 2 at 100 Hz, the mass matrix contribution is 4-8 times larger than the position stiffnesses. From now on, the cross coupling in control current to force transfer function is studied.

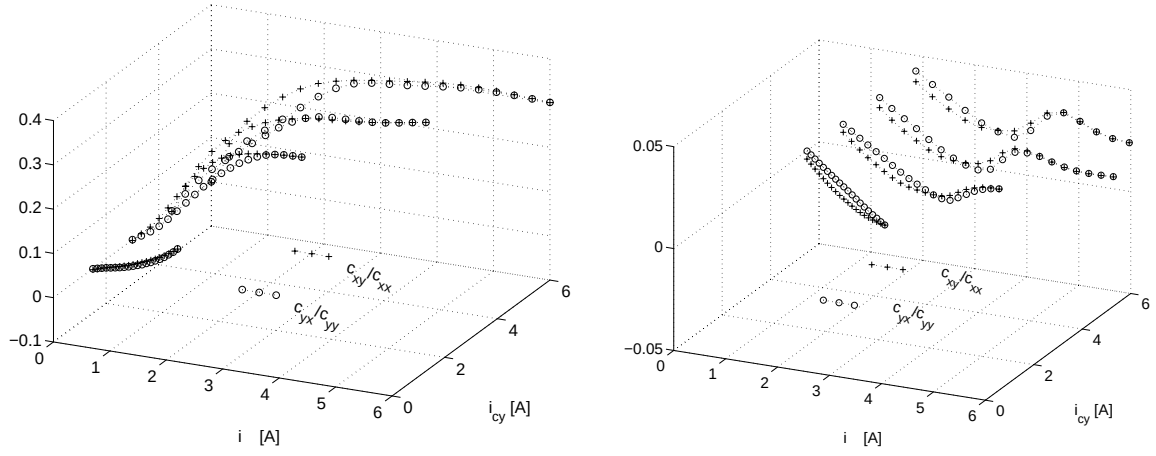

(a) NNSS -pole configuration.

(b) NSNS -pole configuration.

Figure 23: Ratios of the cross coupling position stiffness and the diagonal position stiffness. The relative cross coupling parameters.

The bearing control forces can be written based on the linearised model

$$\Delta \boldsymbol{F}_{\mathrm{b}} = \boldsymbol{h}_{\mathrm{f}}^{\mathrm{T}}(k_{\mathrm{cf}}\boldsymbol{I} + s\boldsymbol{L}_{\mathrm{dyn}} + \boldsymbol{R})^{-1}(k_{\mathrm{cf}}\Delta \boldsymbol{i}_{\mathrm{ref}} - s\boldsymbol{h}_{\mathrm{f}}^{\mathrm{T}}\boldsymbol{p}) \quad (62)$$

$$\Delta \boldsymbol{i}_{\mathrm{ref}} = [\Delta i_{\mathrm{ref1}} \quad \cdots \quad \Delta i_{\mathrm{ref4}}]^{\mathrm{T}} \quad (63)$$

To simplify the model, the velocity induced term $s\boldsymbol{h}_{\mathrm{f}}^{\mathrm{T}}\boldsymbol{p}$ can be neglected for two reasons. First of all, its magnitude is small compared with the current reference term $k_{\mathrm{cf}}\Delta \boldsymbol{i}_{\mathrm{ref}}$. Secondly, it has the phase lead effect similar to the derivative term of the controller and so the effect is stabilising. Thus, without sacrificing the generality, the term can be neglected and bearing control force can be written

$$\Delta \boldsymbol{F}_{\mathrm{b}} = \boldsymbol{h}_{\mathrm{f}}^{\mathrm{T}}(k_{\mathrm{cf}}\boldsymbol{I} + s\boldsymbol{L}_{\mathrm{dyn}} + \boldsymbol{R})^{-1}k_{\mathrm{cf}}\Delta \boldsymbol{i}_{\mathrm{ref}} \quad (64)$$

Typically, the current control loop (k_{cf}) is sized clearly faster than the position control loop. Keeping that in mind, it can be concluded that the major cross coupling effects are due to the cross coupling in the current stiffness matrix $\boldsymbol{h}_{\mathrm{f}}^{\mathrm{T}}$.

Fig. 24 shows the current stiffness parameters of test machine 2, with both pole configurations. The curves show the ratio of the cross coupling current stiffness, h_{fxy} or h_{fyx}, and diagonal current stiffness, h_{fxx} or h_{fyy}. For NNSS -configuration, the absolute maximum of the current stiffness ratio is at around a point where the control current in x-direction reaches the value of bias current. So, in the negative coil the current becomes zero. Thus, a small increment in the current of the positive x-coil decreases the force in y-direction. This situation is demonstrated in Fig. 22. The magnitude of the cross coupling increases as the currents and the saturation increase and, for example, at the current of 6.5 A in the positive y-coil it is 40 percent. It is obvious from Fig. 21 that cross coupling is symmetric with respect to origo. Thus, at negative bearing force in x-direction, the cross coupling is positive and so on. The same applies also for the NSNS- configuration but the magnitude is only about 3 percent at the current of 6.5 A in the positive y-coil.

Fig. 25 presents the same cross coupling parameters at the same operation points as were presented in Fig. 24 with the exception, that the rotor is displaced to positive x- and y-direction from the zero eccentricity to 25 percent relative eccentricity, in respect to mechanical airgap. This is considered to be the largest eccentricity the bearings have to face in practice. This eccentricity combined with positive bearing forces are considered to be the worst case scenario with respect to cross coupling phenomena, because at these operation points the airgaps of dominating magnets are small, thus increasing the parameters, and the saturation phenomena are stronger than at zero eccentricity.

For NNSS -configuration, the phenomena are qualitatively the same as in Fig. 24, with the exception that the symmetry with respect to origo does not exist. The absolute magnitudes

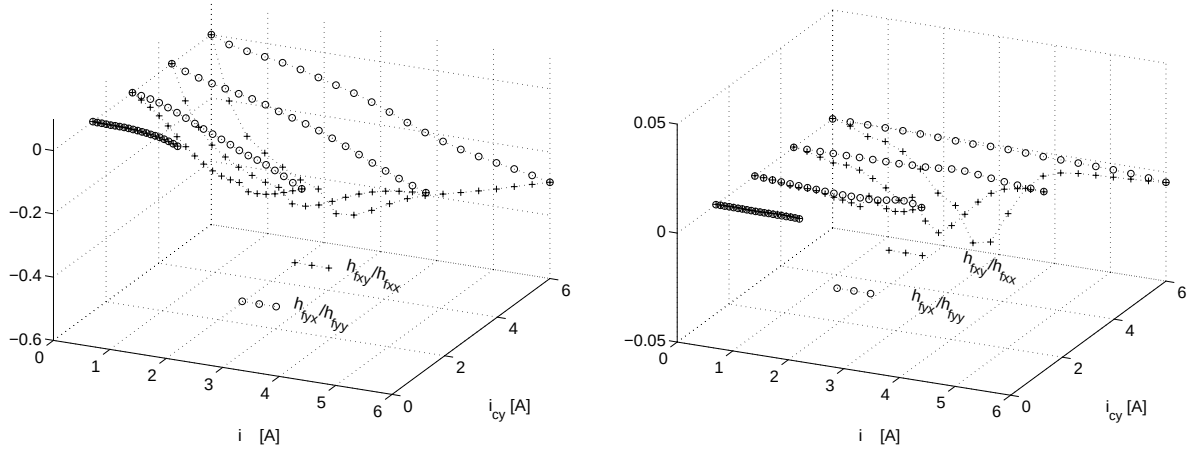

(a) NNSS -pole configuration. *(b) NSNS -pole configuration.*

Figure 24: Relative cross coupling current stiffnesses.

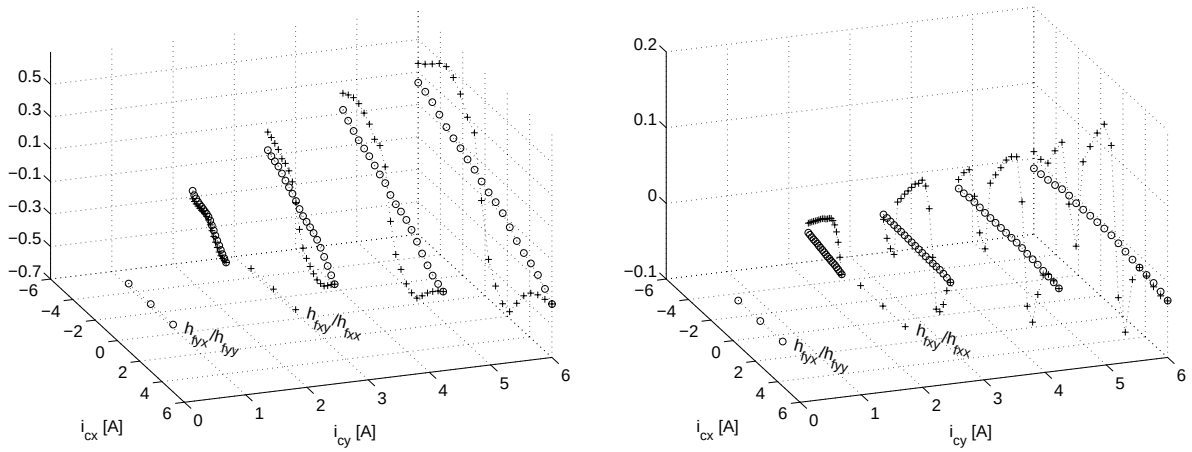

(a) NNSS -pole configuration. *(b) NSNS -pole configuration.*

Figure 25: Relative cross coupling current stiffnesses. The relative eccentricity is 25 % in positive x- and y- direction.

are about 25 percent higher than at zero eccentricity. For NSNS -configuration the situation is a bit different. The ratio of current stiffnesses remains relatively low throughout the load range. The maximum positive values of around 10 percent are reached at bearing currents of 0 A in x- direction and 8 A in y-direction. At zero eccentricity, the coupling was negligible at these loads. The reason for the positive coupling is that the control flux of the positive x-magnet flows through the pole of the positive y-magnet because of the small airgap. In NSNS-configuration, these fluxes are in the same direction and the coupling is positive. At high loads, the negative cross coupling is due to the fact that a part of the control flux goes through the poles of the negative y-magnet.

2.5.3 Effect of cross coupling on the bearing dynamics

The assumptions presented in the previous section, lead to an uncertainty model of AMB-system shown in Fig. 26. In this model, the controller is assumed to be the designed controller $\boldsymbol{G}_{\mathrm{C}}$ without any uncertainties. In addition, the position sensors are assumed ideal and are not drawn. The mechanical rotor model is in practice very precise and has no uncertainty. The bearing model $\boldsymbol{G}_{\mathrm{B}}$ is based on the Eq. 58 at nominal parameter values with some small modifications. The nominal parameter values are values at zero bearing force and eccentricity. The model is modified so that the nominal position stiffnesses are included in the rotor model $\boldsymbol{G}_{\mathrm{R}}$. The bearing model has uncertainties due to the parameter variations shown in the previous sections. These are described by uncertain gain matrix $\mathbf{K}_{\mathrm{B}} = \begin{bmatrix} k_{11} & k_{12} \\ k_{21} & k_{22} \end{bmatrix}$. The cross couplings are refererred as uncertainties and are included in $\mathbf{K}_{\mathrm{B}}$.

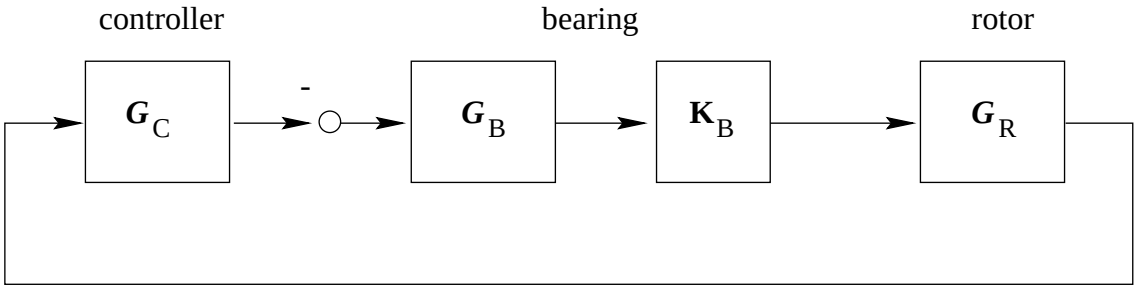

Figure 26: Uncertainty model of the AMB-system.

The effect of cross coupling is clearly demonstrated by studying a pointmass system of two dimensions. In this case all the matrices of the uncertainty model in Fig. 26 except the matrix $\mathbf{K}_{\mathrm{B}}$ are diagonal. Thus, the cross coupling can be studied purely based on the uncertainty matrix. To quantify the effects, the response on the rotational control is calculated. The complex notation is used, in which the real part corresponds to the x-direction and imaginary part corresponds to the y-direction. Let U be an arbitrary rotational control $U = U_0 e^{j\alpha}$ on the system. Then the relative force response f_{r} in complex notation is calculated as follows

$$f_{\mathrm{r}} = [1\ j]\ \mathbf{K}_{\mathrm{B}}[\frac{1}{2}(U + U^{\mathrm{H}}) \quad \frac{1}{2j}(U - U^{\mathrm{H}})]^{\mathrm{T}} \tag{65}$$

The average force response f_{ave} over the control of one rotation can be used to determine the cross coupling effects

$$f_{\mathrm{ave}} = \frac{1}{2\pi}\int_0^{2\pi} f_{\mathrm{r}} e^{-j\alpha} d\alpha \tag{66}$$

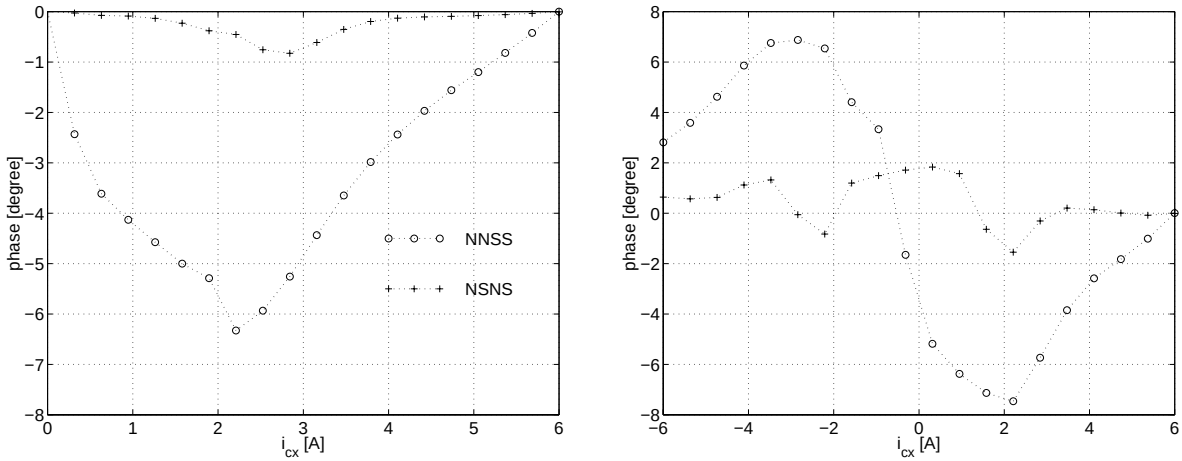

(a) Eccentricity is zero. *(b) Relative eccentricity is 25 %.*

Figure 27: Phase of the average force response $\boldsymbol{F}_{\mathrm{ave}}$ of test machine 2. The control current in y-direction is 6.0 A.

$$
\begin{aligned}
&= \frac{1}{2\pi}\int_0^{2\pi}[1\ j]\ \mathbf{K}_{\mathrm{B}}[\frac{1}{2}(U+U^{\mathrm{H}}) \quad \frac{1}{2j}(U-U^{\mathrm{H}})]^{\mathrm{T}}e^{-j\alpha}d\alpha \\
&= \frac{1}{2}U_0[k_{11}+k_{22}+j(k_{21}-k_{12})]
\end{aligned}
$$

Eq. 66 shows that the cross coupling can be regarded as an additional phase error. The error is interpreted either as phase lag or phase lead, depending on whether the rotational mode is forward or backward mode. This interpretation also depends on the sign of the cross coupling terms.

Fig. 27 presents the phase of the average force response of test machine 2. Both pole-configurations are shown. The cross coupling in NSNS-configuration is negligible. In NNSS-configuration the phase error of eight degree is possible. The main factor is the saturation of the magnetic circuit as, on the other hand, a reasonable relative eccentricity of 25 % has a relatively small effect.

The phase error in NNSS-configuration is unlikely to induce instability, provided the phase margins are reasonable. However, the dynamic properties can be severely impaired. The obvious conclusion is that when the operation range is extended into magnetic saturation region, the NSNS-pole configuration should be used.

2.6 Effect of power amplifier saturation

So far, the effects of the static unidealities of the bearing magnets on the bearing parameters and dynamics have been studied. In this section, the changes of the bearing dynamics, when the power amplifier properties are limited, are investigated.

The AMB amplifier is basically a voltage source driving an inductance. The voltage and current of the power amplifier are limited. Thus, at lower frequencies power amplifier current limits the bearing force and at higher frequencies the bearing force is limited by the power amplifier voltage. In section 1.2.4, it was shown how the dynamic bearing force depends on the maximum voltage and current of the power amplifier. This was based on the assumption of the linearity of the system and is valid for small amplitudes. In a small signal case, the power amplifier is qualitatively a first order low pass filter.

At high frequencies and at large signal (current reference) amplitudes, the voltage needed to drive the wanted current to the coils exceeds the power amplifier voltage. The power amplifier saturates and the coil current and bearing force are distorted from the linear power amplifier estimations. This feature has been previously studied by [Maslen et al. 1989, Satoh et al. 1990, Ahrens and Kucera 1995]. In these studies, the dynamic inductance was considered to be constant and the deviation of the coil current from the control signal was studied. The nonlinearity is studied by simulations based on the model shown in Fig. 28. The nonlinear current-force relationship and the nonlinear flux-current relationship are also taken into account. An especially interesting case is what happens to the low frequency response, when a high frequency component saturates the amplifier.

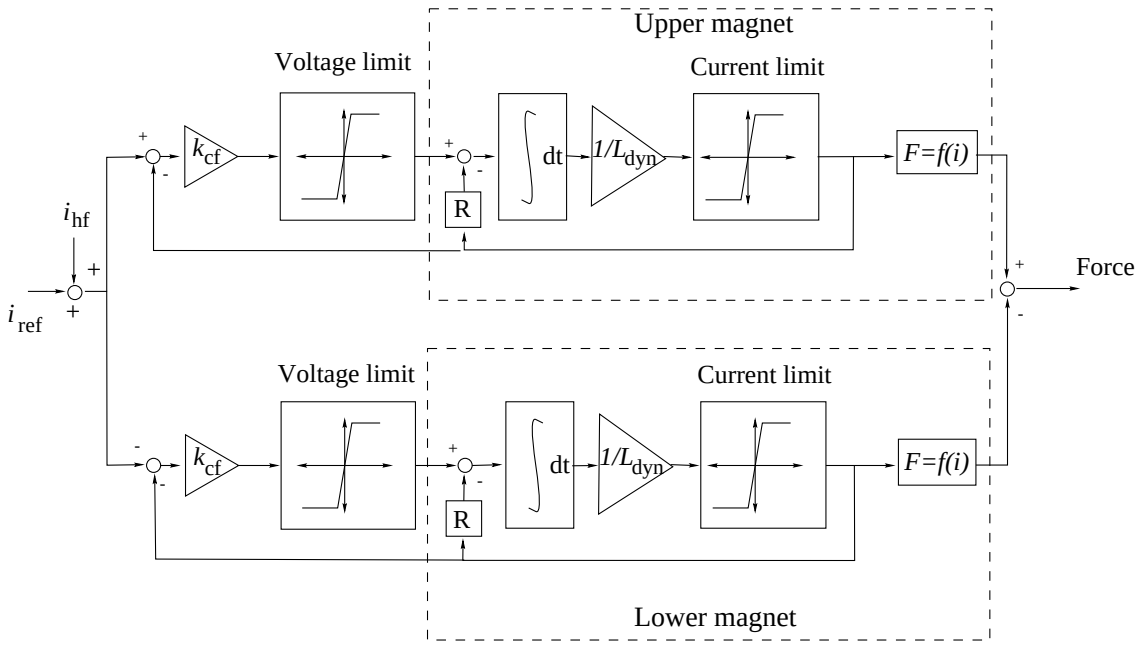

Figure 28: Nonlinear simulation model for analysing the power amplifier saturation.

In the simulations, a sinusoidal control current reference i_{ref} of varying frequency and amplitude is supplied to the model. The describing function of the current reference to the bearing force relationship is calculated and used to study the nonlinear effects. The describing function $g_{\mathrm{h}}(i_{\mathrm{amp}}, \omega)$ is the first harmonic response of the system and is calculated as follows.

$$i_{\mathrm{ref}}(t) = \mathrm{Real}(i_{\mathrm{amp}} e^{j\omega t}) \tag{67}$$

$$F_{\mathrm{b}}(t) = \mathrm{Real}(\sum_{n=1}^{\infty} F_{\mathrm{nb}} e^{jn\omega t}) \tag{68}$$

$$g_{\mathrm{h}}(i_{\mathrm{amp}}, \omega) = \frac{F_{1\mathrm{b}}}{i_{\mathrm{amp}} h_{\mathrm{f0}}} \tag{69}$$

In this section, the describing function is the relative value with respect to the nominal linearised current stiffness h_{f0}, which is 138 N/A.

2.6.1 Large amplitude response

In this section, the high frequency component i_{hf} of the Fig. 28 is zero and only the low frequency component is fed to the model. In Fig. 29, the large amplitude response of test machine 2 is presented. The response is calculated at frequencies of 50, 100, 200, 300, 400, 500, 600, 700 Hz and up to 10 A amplitudes. The response is calculated at current feedback coefficient k_{cf} of 75 and 375 V/A. In the same figure, the small signal response is plotted by the half circle. The normalised curves are the large amplitude response relative to the small signal response and they describe the deviation from the small signal behaviour.

At small frequencies, at 50 and 100 Hz, the amplitude decreases as the current to force relationship decreases, due to the saturation in the magnetic circuit. The phase actually increases somewhat, because the dynamic inductance decreases at large currents. At higher frequencies, the voltage limit becomes the limiting factor and consequently phase drop occurs. The larger current feedback coefficient k_{cf} does not improve the situation. In fact, the phase deviation from small signal response is even larger and begins at considerably lower amplitudes. This effect is a relative phenomenon and the absolute responses at high frequencies are relatively independent of the current feedback coefficient.

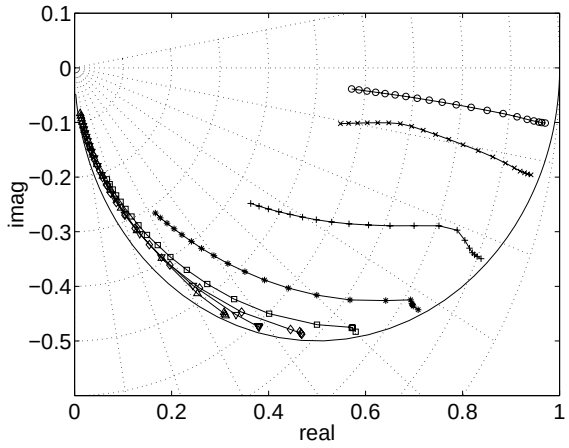

(a) k_{cf}=75 V/A.

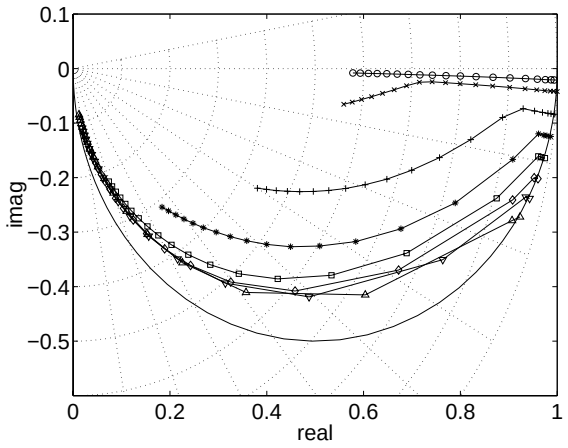

(b) k_{cf}=375 V/A.

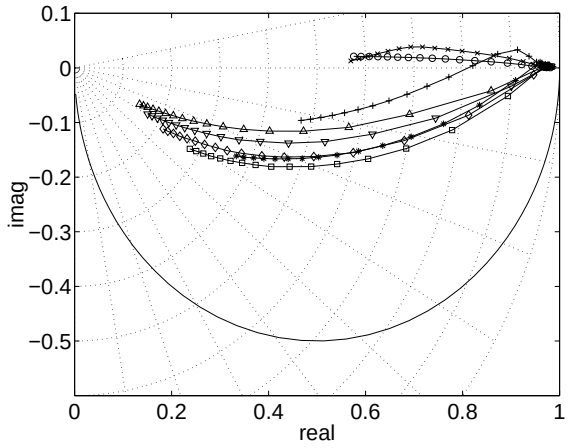

(c) Normalised response k_{cf}=75 V/A.

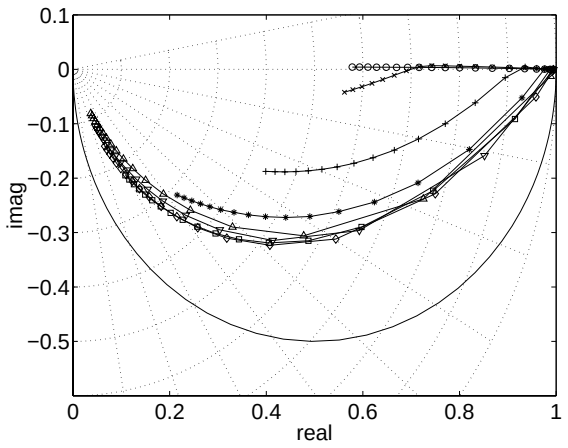

(d) Normalised response k_{cf}=375 V/A.

Figure 29: Large amplitude response $g_{\mathrm{h}}(i_{\mathrm{amp}}, \omega)$ of test machine 2. The solid half circle is the small signal response of a first order low pass filter. The sector lines are drawn with ten degree steps. The curves are calculated at frequencies 50, 100, 200, 300, 400, 500, 600, 700 Hz. The normalised response is the large amplitude response divided by the small signal response.

2.6.2 Effect of high frequency large amplitude disturbance

The power amplifier may saturate due to high frequency disturbance. This can happen, for example, in high-speed machines if the unbalance compensator fails to remove the rotational synchronous component from the control voltage. Another possibility is an unknown sharp mechanical stator resonance at unwanted frequency range [Lantto et al. 1996]. In this case, the power amplifier saturation is not caused by external disturbance, but is due to the properties of the AMB system. In any case, the saturation effects are identical. In this section, it is assumed that the high frequency disturbance is at the frequency of 700 Hz. This is close to the maximum rotational speed of test machine 2. The high frequency input to the amplifier is $i_{\mathrm{hf}}(t) = i_{\mathrm{rel}}\mathrm{Real}(i_1 e^{j2pi700t})$, where i_{rel} is a kind of saturation level and i_1 is the amplitude which causes the maximum control voltage $u_{\mathrm{c}} = u_{\mathrm{max}} = 100V$. $i_1 = 1.614A$ for $k_{\mathrm{cf}} = 75V/A$ and $i_1 = 0.9477A$ for $k_{\mathrm{cf}} = 375V/A$.

Fig. 30 presents the actuator response while high frequency disturbance is present. The saturation levels i_{rel} are 0, 1.25, 1.5, 2 and 3. The response is calculated with current feedback coefficients of 75 V/A and 375 V/A. The current reference amplitude i_{ref} at low frequencies is 0.2 A, so the response can be regarded as a small signal response. Fig. 30 shows that considerable phase lag at low frequencies is caused by high frequency saturation. The larger current feedback coefficient has a marginally better response, but has no practical significance. From this figure, it can be concluded that high frequency saturation can destabilise the AMB system, as experienced by [Larsonneur 1990].

Fig. 31 presents the large amplitude response at low frequencies, when high frequency large amplitude disturbance is present. The responses are calculated at low frequencies of 100 and 200 Hz. The saturation levels i_{rel} are 0, 1, 1.25, 1.5, 2 and 3 and $k_{\mathrm{cf}} = 75V/A$. When the saturation level is above 1.5, the low frequency component reduces the effect of saturation and the phase increases. It is obvious that this type of behaviour makes limit cycle oscillations possible.

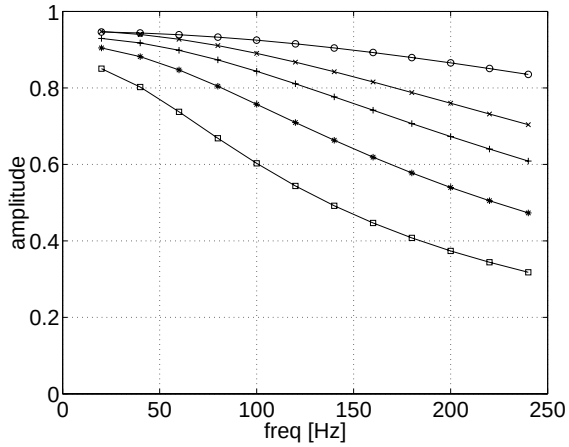

(a) k_{cf}=75 V/A.

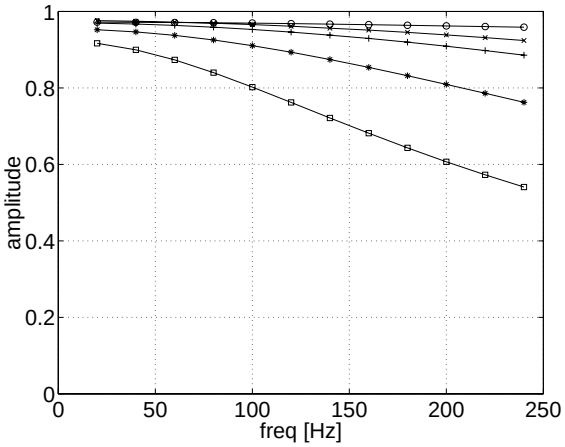

(b) k_{cf}=375 V/A.

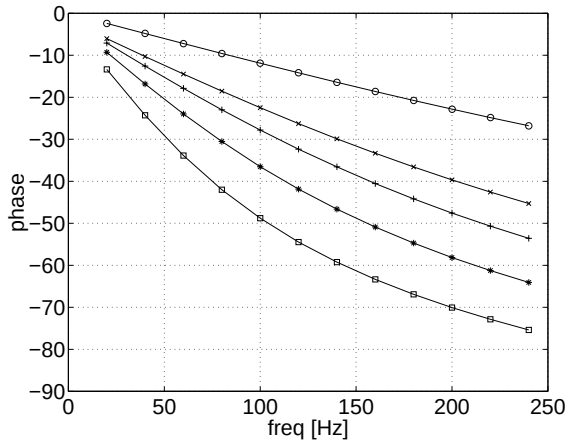

(c) k_{cf}=75 V/A.

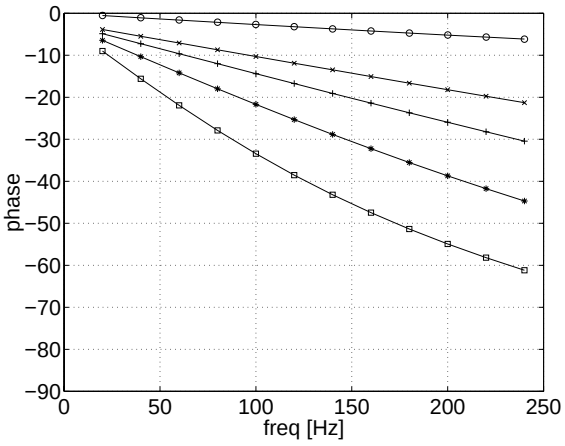

(d) k_{cf}=375 V/A.

Figure 30: Small amplitude response at low frequency, when high frequency large amplitude disturbance is present. The saturation levels i_{rel} due to the high frequency component are 0, 1.25, 1.5, 2 and 3. The larger the saturation, the lower the curve goes.

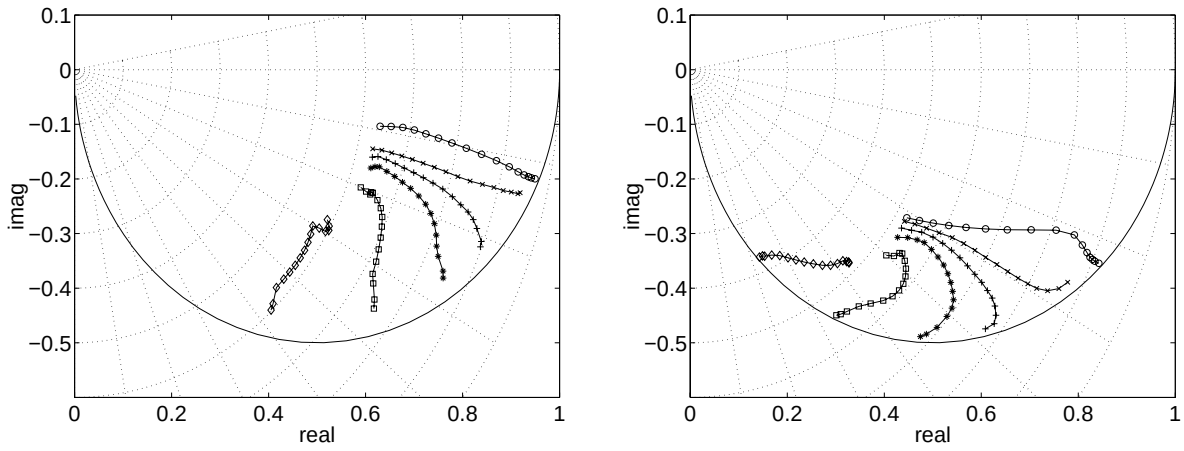

(a) Frequency is 100 Hz.

(b) Frequency is 200 Hz.

Figure 31: Large amplitude response at low frequency, when high frequency large amplitude disturbance is present. The saturation levels i_{rel} due to the high frequency component are 0, 1, 1.25, 1.5, 2 and 3. $k_{\mathrm{cf}} = 75V/A$. The sets are calculated at one saturation level. The phase lag increases as the saturation level increases.

3 Dynamic parameters of radial AMB based on the reluctance network model

3.1 Introduction

In chapter 2, the analysis based on the static magnetic field theory neglected the effect of eddy currents and hysteresis. The modelling and measuring of these effects are extensively studied by the research scientists of electric machines. An excellent review of recent methods and results is presented in the report by Saitz [Saitz 1997]. The problem can be tackled in two ways. The first approach is to neglect the eddy currents and hysteresis when calculating the magnetic field distribution, which is usually done by FEM. Afterwards the losses are calculated by semiempirical loss formulas. In the second approach, the effects are taken into account already when solving the magnetic field distribution. Both these methods involve large numeric calculation tasks as is the case with FEM and time stepping simulation.

In that field, the main interest is the losses caused by hysteresis and eddy currents. These unideal properties of magnetic circuits cause effects which are usually neglected when designing the AMB system and controller. Furthermore, in the machine there are a lot of possible unmodeled eddy current paths. One is on the rotor surface where the sheets may have small short circuit paths due to the machining of the rotor. Another one is the interlaminate currents due to inhomogeneities in the isolation and the high pressure when the sheets are stacked. These phenomena are of course stochastic by nature and difficult to model. The main interest in this study is not the losses but the unmodeled dynamics these properties cause to the AMB system.

In this chapter, these phenomena based on models and measurements are studied. The aim of this chapter is to quantify the phase errors produced by the eddy currents, hysteresis and possible unmodeled eddy current paths in radial AMB.

The magnetic circuit of radial AMB is relatively simple and the reluctance network method is chosen to describe the spatial magnetic field distribution. This is a tradeoff between the simplicity and accuracy of the model. But this can be done keeping in mind the results of the previous chapter, where the FEM was found suitable to determine the static parameters of radial AMB, which can be considered to be the limit values for dynamic parameters at zero frequency.

The eddy currents may have a significant effect on the bearing dynamics, especially, if the bearing system is supposed to have a large bandwidth [Hara et al. 1996]. The exact analysis of eddy currents in the laminations with FEM would require a three dimensional field solution. This is computationally a large task and to study the effect of the design parameters would be even larger. In this section, the effect of eddy currents is analysed based on the one-dimensional eddy current model [Stoll 1974, Meeker and Maslen 1996]. This formulation is

implemented into the reluctance network model of radial magnetic bearing. As a result, a linear model including the effect of eddy currents is produced. The linear model can be directly used when designing the control system of magnetic bearing. As in the previous chapter, the nonlinearity of the magnetic circuit can be taken into account by linearising the system to the static operation point of the bearing.

The hysteresis is the dominating effect at low frequencies. To model this effect a model based on the reluctance network is created. The model combines the nonlinear flux and magnetomotive equations and electric circuit equations. The equation of motion and the controller models can be included as well. The time dependence is modelled with backward Euler method. As a hysteresis model, we use a simple scalar model developed by Tellinen [Tellinen 1998]. Based on the time domain simulation, the linearised dynamic parameters are determined by describing function approach.

3.2 Reluctance network model of the radial AMB

3.2.1 Introduction

In the reluctance network model, Maxwell's field equations are reduced to a set of magnetic circuit equations. The magnetic field distribution can be determined by solving a nonlinear and relatively small set of algebraic equations. The magnetic circuit is divided into reluctances the values of which depend on the geometry and the magnetisation of the material. It is worth noticing the assumptions used in the reluctance network model.

- The direction of the flux density is assumed to be known beforehand.
- The flux density is assumed to be constant on every flux carrying cross section.
- The leakage flux is assumed to flow only in the modelled leakage paths.
- The flux fringing in the vicinity of the airgap is taken into account by increasing the effective area of the airgap.
- The saturation of the magnetic circuit does not change the distribution of the magnetic field.

When these assumptions are taken into account, the Maxwell's equations and the material equation connecting magnetic field and flux density can be reduced to a set of nonlinear algebraic equations. In this section, the stationary reluctance network formulation is presented, which is needed in the eddy current and hysteresis models.

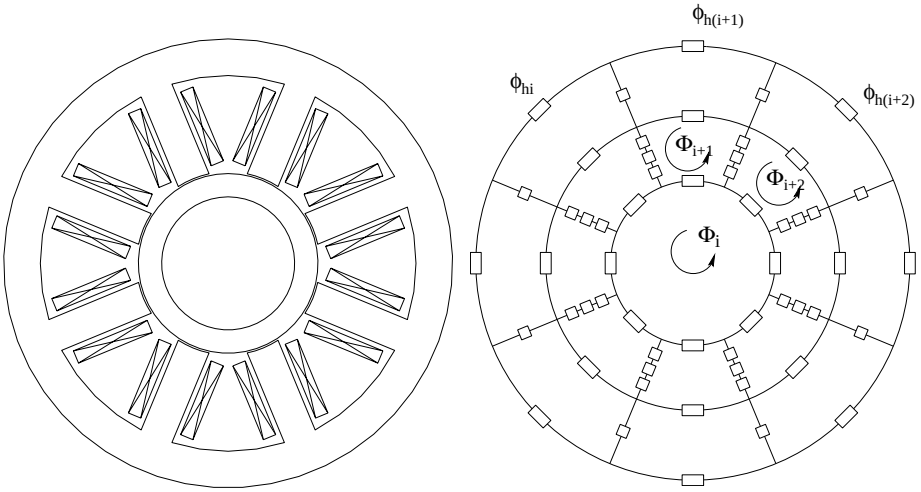

Figure 32: Geometry and reluctance network of an 8-pole radial active magnetic bearing.

3.2.2 Solution of the fluxes

A typical geometry of an eight-pole radial magnetic bearing and its reluctance network model with loop-fluxes are shown in Fig. 32. In this example, the stray flux between teeth is modelled with one stray flux reluctance and the reluctance of the tooth is divided into two parts. In the reluctance network model, the solution of the loop-fluxes shown in Fig. 32 is found. The branch magnetic fluxes in the reluctances can be calculated from the loop-fluxes as follows

$$\boldsymbol{\phi}_{\mathrm{h}} = \mathbf{T}^{\mathrm{T}} \boldsymbol{\Phi} \tag{70}$$

where $\mathbf{T}$ is a loop-set matrix, $\boldsymbol{\phi}_{\mathrm{h}}$ is a vector containing the branch fluxes and $\boldsymbol{\Phi}$ is a vector containing the loop-fluxes. The loop-set matrix $\mathbf{T}$ is formed as follows:

- $\mathrm{T}_{ij} = 1$, if branch j belongs to the route of loop- flux i and the branch-flux has the same direction as the loop-flux.
- $\mathrm{T}_{ij} = -1$, if branch j belongs to the route of loop- flux i and the branch-flux has the opposite direction from the loop-flux.
- $\mathrm{T}_{ij} = 0$, otherwise.

The same loop-set matrix also connects the loop-magnetomotive forces and the branch-magnetomotive forces

$$\boldsymbol{T}\boldsymbol{f}_{\mathrm{h}} = \boldsymbol{M}_{\mathrm{f}} \tag{71}$$

where $\boldsymbol{M}_{\mathrm{f}}$ is a vector whose components are the loop-magnetomotive forces and vector $\boldsymbol{f}_{\mathrm{h}}$ contains the magnetomotive forces in the branch-reluctances. The loop-magnetomotive

force vector is calculated from coil currents and the number of coil turns per pole. The loop-magnetomotive vector entries are

$$\boldsymbol{M}_{\mathrm{f}} = \boldsymbol{N}\boldsymbol{i} \tag{72}$$

$$\boldsymbol{i} = [i_1 \cdots i_k]^{\mathrm{T}} \tag{73}$$

where $\boldsymbol{i}$ is a vector of the coil currents and $\boldsymbol{N}$ is a coupling matrix, coupling the coil currents into magnetomotive forces of the loops. Thus, the entries of $\boldsymbol{M}_{\mathrm{f}}$ describe the total current flowing through the loop i. On the other hand, the magnetomotive forces and fluxes are connected to each other by diagonal reluctance matrix $\boldsymbol{R}_{\mathrm{m}}$

$$\begin{aligned} \boldsymbol{f}_{\mathrm{h}} &= \boldsymbol{R}_{\mathrm{m}}\boldsymbol{\phi}_{\mathrm{h}} \\ \boldsymbol{R}_{\mathrm{m}} &= \begin{bmatrix} R_{\mathrm{m1}} & & 0 \\ & \ddots & \\ 0 & & R_{\mathrm{mN}} \end{bmatrix} \\ R_{\mathrm{m}i} &= R_{\mathrm{m}i}(\phi_{\mathrm{h}i}) \end{aligned} \tag{74}$$

where $R_{\mathrm{m}i}$ is the reluctance of branch i. Due to the saturation of the core material, the reluctance of branch i depends on the flux density and the geometry of the branch. The nonlinear magnetisation curve is modelled by a single-valued monotonic reluctivity curve for the core material used. The reluctivity curve is formed from the peak magnetisation curve given by the manufacturers of electric steel sheets. The values of the rectangular reluctances can be calculated from the following formula.

$$R_{\mathrm{m}i} = \frac{l_i \nu_i(B_i)}{A_{\mathrm{h}i}} \tag{75}$$

where l_i is the length of the reluctance in the direction of the flux density, $A_{\mathrm{h}i}$ is the cross sectional area of the reluctance, $\nu_i(B_i)$ is the reluctivity and B_i is the flux density of the rectangular branch i. All other reluctances but the stray flux reluctance are assumed to be rectangular. The stray flux reluctance of a symmetrical conventional radial magnetic bearing is found to be,

$$R_{\mathrm{m}i} = \frac{2\alpha\pi h_{\mathrm{s}}\nu_0}{z_i[(y_{n+1} - y_n) - r_{\mathrm{s}}\ln(\frac{y_{n+1}}{y_n})]} \tag{76}$$

where α is the angle between two teeth, h_{s} is the height of the slot, ν_0 is the reluctivity of vacuum, z_i is the axial length of the branch-reluctance i, r_{s} is the radius of the tooth tip, y_{n+1} and y_n are the upper and lower distances of stray reluctance n from the tooth tip.

The whole nonlinear system of equations can be expressed by the loop-fluxes and the loop-magnetomotive forces. This non-linear system is solved by Newton-Raphson iteration

$$\mathbf{T}\boldsymbol{R}_{\mathrm{m}}(\boldsymbol{\phi}_{\mathrm{h}})\ \mathbf{T}^{\mathrm{T}}\boldsymbol{\Phi} = \boldsymbol{M}_{\mathrm{f}} \tag{77}$$

$$\Longrightarrow \tag{78}$$

$$\boldsymbol{r}^k = \mathbf{T}\boldsymbol{R}_{\mathrm{m}}(\boldsymbol{\phi}_{\mathrm{h}}{}^k)\ \mathbf{T}^{\mathrm{T}}\boldsymbol{\Phi}^k - \boldsymbol{M}_{\mathrm{f}} \tag{79}$$

where $\boldsymbol{r}^k$ is the residual vector after k iteration steps. In the iteration process, the next values of the loop-fluxes are calculated from the previous values of residuals, loop-fluxes and Jacobian matrix

$$\boldsymbol{\Phi}^{k+1} = \boldsymbol{\Phi}^k - \boldsymbol{P}^{-1}\boldsymbol{r}^k \tag{80}$$

$$\boldsymbol{P}^k = \mathbf{T}\frac{\partial(\boldsymbol{R}_{\mathrm{m}}(\boldsymbol{\phi}_{\mathrm{h}})\boldsymbol{\phi}_{\mathrm{h}})}{\partial\boldsymbol{\phi}_{\mathrm{h}}}\ \mathbf{T}^{\mathrm{T}} \tag{81}$$

$$\frac{\partial(\boldsymbol{R}_{\mathrm{m}}(\boldsymbol{\phi}_{\mathrm{h}})\boldsymbol{\phi}_{\mathrm{h}})}{\partial\boldsymbol{\phi}_{\mathrm{h}}} = \begin{bmatrix} \frac{\partial f_{\mathrm{h1}}}{\partial\phi_{\mathrm{h1}}} & & 0 \\ & \ddots & \\ 0 & & \frac{\partial f_{\mathrm{hN}}}{\partial\phi_{\mathrm{hN}}} \end{bmatrix}$$

where f_{hi}, $\phi_{\mathrm{h}i}$ are the ith component of the vectors $\boldsymbol{f}_{\mathrm{h}}$ and $\boldsymbol{\phi}_{\mathrm{h}}$ respectively. The iteration has converged when the following condition is reached

$$\frac{\left\|\boldsymbol{r}^k\right\|_2}{\left\|\boldsymbol{M}_{\mathrm{f}}\right\|_2} < \epsilon \tag{82}$$

where ϵ is a positive real number.

3.2.3 Calculation of forces and linearised parameters

From the magnetic field solution, the static electromagnetic characteristics of a radial bearing can be derived. This section deals with the determination of forces, current stiffness, position stiffness, self and mutual inductances.

Force

The force of the radial bearing is calculated based on the principle of virtual work.

$$\boldsymbol{F}_{\mathrm{b}} = -[\frac{\partial W_m}{\partial x}\ \ \frac{\partial W_m}{\partial y}]^{\mathrm{T}} = -\frac{\partial W_m}{\partial \boldsymbol{p}} \tag{83}$$

$$\boldsymbol{F}_{\mathrm{b}} = [F_{\mathrm{x}}\ F_{\mathrm{y}}]^{\mathrm{T}} \tag{84}$$

$$\boldsymbol{p} = [x\ y]^{\mathrm{T}} \tag{85}$$

where W_m is the magnetic energy of the system. The magnetic energy can be derived from the magnetic field solution and the derivative of the energy with respect to a virtual displacement $\boldsymbol{p}$ can be derived from the same solution

$$W_m = \int_V \int_0^B H dB dV \tag{86}$$

$$W_m = \int_0^{\boldsymbol{\phi}_\mathrm{h}} \boldsymbol{f}_\mathrm{h}{}^\mathrm{T} d\boldsymbol{\phi}_\mathrm{h} \tag{87}$$

$$W_m = \int_0^{\boldsymbol{\Phi}} \boldsymbol{\Phi}^T \ \mathbf{T}\boldsymbol{R}_\mathrm{m} \ \mathbf{T}^\mathrm{T} d\boldsymbol{\Phi} \tag{88}$$

$$\boldsymbol{F}_\mathrm{b} = -\frac{\partial W_m}{\partial \boldsymbol{p}} \tag{89}$$

$$\boldsymbol{F}_\mathrm{b} = -\frac{1}{2}\boldsymbol{\phi}_\mathrm{h}{}^\mathrm{T} \frac{\partial \boldsymbol{R}_\mathrm{m}}{\partial \boldsymbol{p}} \boldsymbol{\phi}_\mathrm{h} \tag{90}$$

$$\boldsymbol{F}_\mathrm{b} = -\frac{1}{2}\boldsymbol{\Phi}^\mathrm{T} \ \mathbf{T}\frac{\partial \boldsymbol{R}_\mathrm{m}}{\partial \boldsymbol{p}} \ \mathbf{T}^\mathrm{T} \boldsymbol{\Phi} \tag{91}$$

It should be noticed that the partial differentiation with respect to the virtual displacement affects only the airgap reluctances. This means that the nonlinear energy integral of Eq. 87 reduces to a linear integral. Thus, implementation of this method is straightforward. The force can be calculated from the loop-flux solution after the matrix $\frac{\partial \boldsymbol{R}_\mathrm{m}}{\partial \boldsymbol{p}}$ is formed.

Current and position stiffness

In a similar fashion, the current stiffness matrix, which consist of the current stiffnesses for every individual coil can be calculated from the magnetic field solution

$$\boldsymbol{h}_\mathrm{f} = -\frac{\partial^2 W_m}{\partial \boldsymbol{i} \partial \boldsymbol{p}} \tag{92}$$

$$\boldsymbol{h}_\mathrm{f} = -\boldsymbol{\phi}_\mathrm{h}{}^\mathrm{T} \frac{\partial \boldsymbol{R}_\mathrm{m}}{\partial \boldsymbol{p}} \frac{\partial \boldsymbol{\phi}_\mathrm{h}}{\partial \boldsymbol{i}} \tag{93}$$

$$\boldsymbol{h}_\mathrm{f} = -\boldsymbol{\phi}_\mathrm{h}{}^\mathrm{T} \frac{\partial \boldsymbol{R}_\mathrm{m}}{\partial \boldsymbol{p}} \ \mathbf{T}^\mathrm{T} \boldsymbol{P}^{-1} \frac{\partial \boldsymbol{M}_\mathrm{f}}{\partial \boldsymbol{i}} \tag{94}$$

$$\boldsymbol{h}_\mathrm{f} = -\boldsymbol{\Phi}^\mathrm{T} \ \mathbf{T}\frac{\partial \boldsymbol{R}_\mathrm{m}}{\partial \boldsymbol{p}} \ \mathbf{T}^\mathrm{T} \boldsymbol{P}^{-1} \boldsymbol{N} \tag{95}$$

$$\boldsymbol{h}_\mathrm{f} = \begin{bmatrix} h_{\mathrm{fx1}} & \cdots & h_{\mathrm{fxk}} \\ h_{\mathrm{fy1}} & \cdots & h_{\mathrm{fyk}} \end{bmatrix}$$

where $\boldsymbol{P}^{-1}$ is the inverse matrix of the Jacobian in Eq. 81 at the final iteration step. The derivative vector of the magnetomotive force with respect to coil current is as in Eq. 72. Thus, the current stiffness is calculated in one operation point for each individual coil and

the current stiffness in one coordinate direction is the sum of the current stiffnesses of the opposite coils.

Also, the position stiffness is calculated from the reluctance network field solution

$$\boldsymbol{c} = -\frac{\partial^2 W_m}{\partial \boldsymbol{p} \partial \boldsymbol{p}} \tag{96}$$

$$\boldsymbol{c} = -{\boldsymbol{\phi}_\mathrm{h}}^\mathrm{T} \frac{\partial \boldsymbol{R}_\mathrm{m}}{\partial \boldsymbol{p}} \frac{\partial {\boldsymbol{\phi}_\mathrm{h}}^\mathrm{T}}{\partial \boldsymbol{p}} \tag{97}$$

$$\boldsymbol{c} = -{\boldsymbol{\Phi}}^\mathrm{T}\ \mathbf{T} \frac{\partial \boldsymbol{R}_\mathrm{m}}{\partial \boldsymbol{p}}\ \mathbf{T}^\mathrm{T} \frac{\partial \boldsymbol{\Phi}}{\partial \boldsymbol{p}} \tag{98}$$

$$\boldsymbol{c} = \begin{bmatrix} c_{xx} & c_{xy} \\ c_{yx} & c_{yy} \end{bmatrix}$$

The partial derivative of the diagonal reluctance matrix and the loop- fluxes are calculated separately with respect to the Cartesian coordinates. The partial derivative of the loop-fluxes is calculated numerically with respect to a real displacement, while keeping the magnetomotive force constant.

Self and mutual inductances

The self and mutual inductances of the coils depend on the operation point of the bearings. In the dynamic model of a radial bearing, the dynamic inductance is needed. The dynamic inductance is defined

$$\boldsymbol{L}_\mathrm{dyn} = \frac{\partial \boldsymbol{\Psi}}{\partial \boldsymbol{i}} \tag{99}$$

$$\boldsymbol{\Psi} = \left[\Psi_1 \ \cdots \ \Psi_k\right]^\mathrm{T} \tag{100}$$

where $\boldsymbol{\Psi}$ is the vector of coil fluxes. The dynamic inductance matrix containing the self and mutual inductances can also be calculated directly from the branch-fluxes and the Jacobian. By the definition of the dynamic inductance, it can written

$$\boldsymbol{L}_\mathrm{dyn} = \boldsymbol{N}^\mathrm{T} \boldsymbol{P}^{-1} \boldsymbol{N} \tag{101}$$

$$\boldsymbol{L}_\mathrm{dyn} = \begin{bmatrix} L_{11} & \cdots & L_{1k} \\ \vdots & \ddots & \vdots \\ L_{k1} & \cdots & L_{kk} \end{bmatrix}$$

3.3 Eddy current model of the radial AMB

3.3.1 One-dimensional model

As in the reluctance network model, all flux is assumed to flow perpendicular to the surface of the lamination as in Fig. 33. Because the width of the lamination is much larger than the thickness d, the end effects are neglected. Thus, the eddy currents are assumed to flow only in the direction perpendicular to the surface. It is assumed that the material is homogenous, that is, the reluctivity is constant in the lamination. In a nonlinear analysis, the value of the reluctivity depends on the operation point of the bearing. Thus, the eddy current model can be seen as a small signal model in the neighbourhood of the operation point. At large amplitudes, the saturation along the width of the lamination has a significant effect on the eddy current distribution and losses [Bottauscio 1996]. It is worth noticing that this model describes only so called classical eddy current losses. This loss is due to the macroscopic conductivity of the iron sheet. Another eddy current loss component of equal importance is the excess loss [Saitz 1997]. This component is neglected in this analysis. In practice, these loss components are of the same magnitude, so this method is likely to underestimate the dynamic effects of eddy currents in AMB.

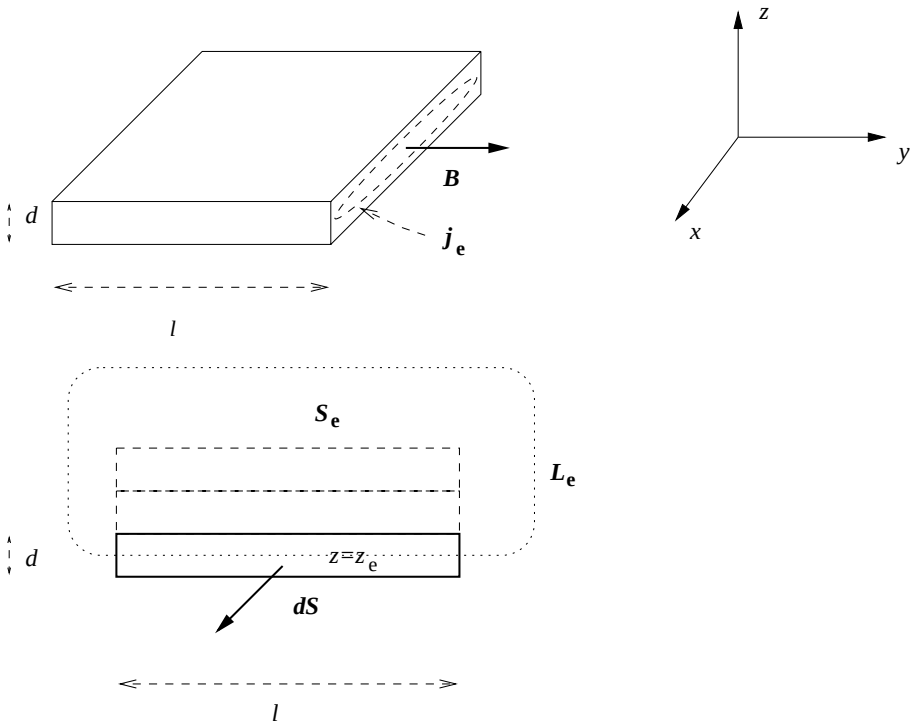

Figure 33: Eddy currents in one lamination and the integration area.

Under these assumptions, the solution of the flux density in the lamination can be found. In the Laplace domain, the average flux density can be expressed

$$B_{\mathrm{ave}} = B_{\mathrm{s}} \frac{\tanh(\sqrt{s\sigma\mu}\frac{d}{2})}{\sqrt{s\sigma\mu}\frac{d}{2}} \tag{102}$$

where B_{s} is the flux density at the surface of the lamination, σ is the conductivity, μ is the permeability, d is the thickness of the lamination and B_{ave} is the average flux density across the lamination thickness. Thus, as the frequency is increased, the flux is pushed towards the edges of the lamination. In order to be able to include the eddy current formulation in the reluctance network model, a relation between the (i^{th}) branch- magnetomotive force f_{hi} and the average flux density B_{ave} must be formed. This relation is formed from the integral form of Maxwell's fourth equation.

$$\oint_L \boldsymbol{H} \cdot d\boldsymbol{L} = \int_S \boldsymbol{J} \cdot d\boldsymbol{S} \tag{103}$$

The surface integration is done over an area S_{e} which splits the lamination of interest into two parts at certain $z = z_{\mathrm{e}}$. The integration area is chosen in such a way that all the other laminations are totally covered by the area. Thus, the contribution from the other laminations is zero. The only contribution to the right hand side of Eq. 103 comes from the area of the particular lamination enclosed by the integration surface. The magnetomotive force $f_{\mathrm{h}i}$ of a reluctance network branch i depends on the eddy current density

$$f_{\mathrm{h}} = \oint_{L_e} \boldsymbol{H} \cdot d\boldsymbol{L_e} + \int_{S_e} \boldsymbol{J}_{\mathrm{e}} \cdot d\boldsymbol{S} \tag{104}$$

where all the quantities correspond to branch i. For the simplicity of the notation the subscript i is dropped and for a moment only a single branch-reluctance is considered. The line integral L_e is taken over the boundary of S_e. As it is assumed that the flux density $\boldsymbol{B}$ and the eddy current density $\boldsymbol{J}_{\mathrm{e}}$ do not vary along the length of the lamination, Eq. 104 can be written

$$f_{\mathrm{h}} = lH(z_{\mathrm{e}}) + l\int_{z_{\mathrm{e}}}^{\frac{d}{2}} J_{\mathrm{e}}(z)dz \tag{105}$$

$$f_{\mathrm{h}} = lH(z_{\mathrm{e}}) + l\int_{z_{\mathrm{e}}}^{\frac{d}{2}} \frac{\partial H}{\partial z}dz \tag{106}$$

$$f_{\mathrm{h}} = l(\frac{B_{\mathrm{s}}}{\mu} - \int_{z_{\mathrm{e}}}^{\frac{d}{2}} \frac{\partial H}{\partial z}dz) + l\int_{z_{\mathrm{e}}}^{\frac{d}{2}} \frac{\partial H}{\partial z}dz \tag{107}$$

$$f_{\mathrm{h}} = \frac{l}{\mu}B_{\mathrm{s}} \tag{108}$$

where B_{s} is the flux density at the surface of the lamination of particular reluctance network branch i. Eq. 108 can be transformed into the frequency domain and the magnetomotive force can be expressed as a function of Laplace variable s and average flux density

$$f_{\mathrm{h}}(s) = \frac{l}{\mu(s)} B_{\mathrm{ave}} \tag{109}$$

$$\mu(s) = \mu \frac{\tanh \sqrt{s\sigma\mu}\frac{d}{2}}{\sqrt{s\sigma\mu}\frac{d}{2}} \tag{110}$$

Frequency response of the permeability can be calculated from Eq. 110. However, the complex permeability is not very convenient for control design purposes, because the network solution would have to be solved for every frequency. Thus, a model in Laplace domain is preferred. The magnetomotive force of Eq. 109 is defined in another way

$$f_{\mathrm{h}}(s) = \frac{l}{\mu} B_{\mathrm{ave}} - i_{\mathrm{ec}}(s) \tag{111}$$

The i_{ec} is the effect of eddy currents in the lamination and can be interpreted as a one-turn coil, around the particular reluctance network branch i, carrying an arbitrary current. The electric circuit equations of pole winding are written assuming that i_{ec}'s are arbitrary inputs to the system. The current i_{ec} is then determined by the transfer function

$$\frac{i_{\mathrm{ec}}(s)}{\phi_{\mathrm{h}}(s)} = \left(\frac{l}{A_{\mathrm{h}}\mu} - \frac{l}{A_{\mathrm{h}}\mu(s)}\right) \tag{112}$$

$$\phi_{\mathrm{h}} = B_{\mathrm{ave}} A_{\mathrm{h}} \tag{113}$$

where ϕ_{h} is the total flux flowing through the lamination of branch i and A_{h} is the cross sectional area of the branch i. The hyperbolic tangent can be expanded in continued fraction form as

$$\tanh(x) = \cfrac{x}{1 + \cfrac{x^2}{3 + \cfrac{x^2}{5 + \cdots}}} \tag{114}$$

This can be substituted into Eq. 112 to yield

$$\frac{i_{\mathrm{ec}}(s)}{\phi_{\mathrm{h}}(s)} = -\left(\frac{l}{A_{\mathrm{h}}\mu}\right) \cfrac{s\gamma^2}{1 + \cfrac{s\gamma^2}{3 + \cfrac{s\gamma^2}{5 + \cdots}}} \tag{115}$$

$$\gamma = \sqrt{\sigma\mu}\frac{d}{2} \tag{116}$$

This can be rearranged into the form

$$\frac{i_{\mathrm{ec}}(s)}{\phi_{\mathrm{h}}(s)} = \cfrac{-s}{R_{\mathrm{ec1}} + \cfrac{1}{\cfrac{1}{sL_{\mathrm{ec1}}} + \cfrac{1}{R_{\mathrm{ec2}} + \cfrac{1}{\cfrac{1}{sL_{\mathrm{ec2}}} + \cdots}}}} \tag{117}$$

$$L_{\mathrm{ecj}} = \frac{A_{\mathrm{h}}\mu}{(4j+1)l} \tag{118}$$

$$R_{\mathrm{ecj}} = \frac{4(4j-1)A_{\mathrm{h}}}{\sigma l d^2}. \tag{119}$$

Fig. 34 presents the interpretation of Eq. 117. Eq. 117 can be viewed as a chain of inductances and resistances driven by a one-turn coil. Thus, the effect of eddy currents can be viewed as a parasitic winding around each section of the iron flux path. For a finite-state model, the chain is truncated after an arbitrary number of resistances and inductances.

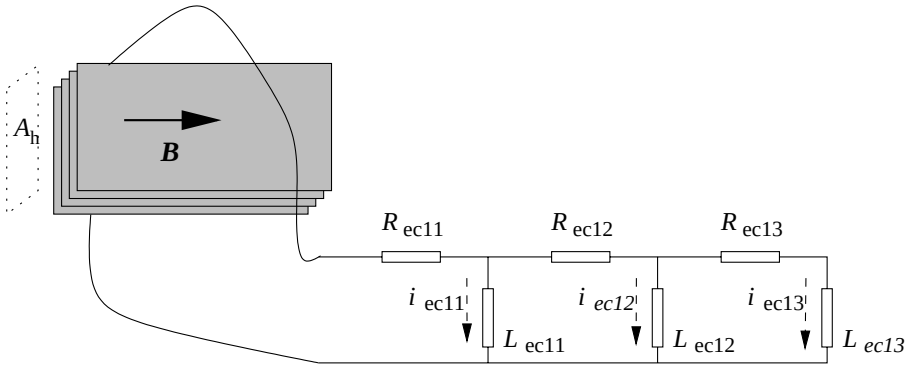

Figure 34: Interpretation of the eddy current model in one branch reluctance.

3.3.2 Implementation into the reluctance network model

It is possible to implement the above model into the reluctance network model of radial magnetic bearings. As a result, a model of relatively low order (at least compared to 3-D FEM) is formed. The model is a linearised model, which can be effectively included in the control system design and it can take into account both the saturation of the magnetic circuit and the eddy current effects. It is worth noticing that the saturation is taken into account by linearising the system at a certain operation point. Thus, the model is a small-signal model and the validity at larger amplitudes is at least questionable. In the model presented in this thesis, the regular eight pole radial bearing is considered.

The nature of the model is similar to the standard linearised dynamic model of the magnetic bearings in the sense that the induced voltage term is divided into current and velocity induced terms

$$\boldsymbol{u} = \frac{d\,\boldsymbol{\Psi}}{dt} + \boldsymbol{R}\boldsymbol{i} \tag{120}$$

$$\boldsymbol{u} = \boldsymbol{N}^{\mathrm{T}}\frac{d\,\boldsymbol{\Phi}}{dt} + \boldsymbol{R}\boldsymbol{i} \tag{121}$$

$$\boldsymbol{\Phi} = \boldsymbol{K}_1\boldsymbol{i} + \boldsymbol{K}_2\boldsymbol{p} - \boldsymbol{K}_3\boldsymbol{i}_{\mathrm{ec}} \tag{122}$$

where $\boldsymbol{u}$ is the vector of the coil voltages, $\boldsymbol{i}$ is the vector of the coil currents, $\boldsymbol{p}$ is the displacement of the rotor, $\boldsymbol{i}_{\mathrm{ec}}$ is the vector of the eddy currents of the model, $\boldsymbol{R}$ is the diagonal resistance matrix, $\boldsymbol{\Psi}$ is the vector of the coil fluxes, $\boldsymbol{\Phi}$ is the vector of the loop-fluxes, $\boldsymbol{N}$ is the matrix coupling the loop-fluxes and the coil voltages, $\boldsymbol{K}_1$ is the matrix of the linearised current to loop-flux coefficients, $\boldsymbol{K}_2$ is the matrix of the linearised displacement to loop- flux coefficients, $\boldsymbol{K}_3$ is the matrix coupling the eddy currents of the model and the loop-fluxes. The coupling matrices are calculated from the reluctance network field solution of the magnetic bearing in the following way

$$\boldsymbol{K}_1 = \frac{\partial \boldsymbol{\Phi}}{\partial \boldsymbol{i}} = \boldsymbol{P}^{-1}\frac{\partial \boldsymbol{M}_{\mathrm{f}}}{\partial \boldsymbol{i}} = \boldsymbol{P}^{-1}\boldsymbol{N} \tag{123}$$

$$\boldsymbol{K}_2 = \frac{\partial \boldsymbol{\Phi}}{\partial p} \tag{124}$$

$$\boldsymbol{K}_3 = \frac{\partial \boldsymbol{\Phi}}{\partial \boldsymbol{i}_{\mathrm{ec}}} = \boldsymbol{P}^{-1}\frac{\partial \boldsymbol{M}_{\mathrm{f}}}{\partial \boldsymbol{i}_{\mathrm{ec}}} = \boldsymbol{P}^{-1}\ \mathbf{T} \tag{125}$$

where the notation is the same as in the previous section. It should be noticed that in Eq. 125 the partial differentiation is presented as if eddy currents flowed in all the branch-reluctances. However, it is obvious that e.g. in the airgap reluctances no eddy currents exist.

The model of the eddy currents consists of the chain of inductances and resistances as can be seen from Fig. 34 . Every flux path through iron acts as a source of its chain of inductor-resistor pair. Thus, for the network model a system of equations is

$$\frac{d\boldsymbol{\phi}_{\mathrm{hfe}}}{dt} = \boldsymbol{L}_{\mathrm{ec}}\frac{d\boldsymbol{i}_{\mathrm{ecfe}}}{dt} + \boldsymbol{R}_{\mathrm{ec}}\boldsymbol{i}_{\mathrm{ecfe}} \tag{126}$$

$$\boldsymbol{\phi}_{\mathrm{hfe}} = [\phi_{\mathrm{hf1}}\ \overbrace{0\ \cdots\ 0}^{o-1}\ \phi_{\mathrm{hf2}}\ \overbrace{0\ \cdots\ 0}^{o-1}\ \cdots\ \phi_{\mathrm{hfm}}\ \overbrace{0\ \cdots\ 0}^{o-1}]^{\mathrm{T}} \tag{127}$$

$$i_{\mathrm{ecfe}} = [i_{\mathrm{ec}11}\ i_{\mathrm{ec}12}\ \cdots\ i_{\mathrm{ec}1o}\ \cdots\ i_{\mathrm{ec}m1}\ i_{\mathrm{ec}m2}\ \cdots\ i_{\mathrm{ec}mo}]^{\mathrm{T}} \tag{128}$$

$$\boldsymbol{i}_{\mathrm{ec}} = \left[\sum_{j=1}^{o}\boldsymbol{i}_{\mathrm{ec}1j}\ \sum_{j=1}^{o}i_{\mathrm{ec}2j}\ \cdots\ 0\ 0\ 0\ \cdots\ \sum_{j=1}^{o}i_{\mathrm{ec}mj}\ \cdots\ 0\ 0\ \cdots\right]^{\mathrm{T}} \tag{129}$$

where $\boldsymbol{\phi}_{\mathrm{hfe}}$ is a modified branch-flux vector, where $\boldsymbol{\phi}_{\mathrm{hf}}$ are only those branch-reluctances where eddy currents exist. The $\boldsymbol{i}_{\mathrm{ecfe}}$ is the vector of the eddy currents in the model and corresponds to the currents flowing through the inductors in Fig. 34. The $\boldsymbol{i}_{\mathrm{ec}}$ is a vector of size n, thus an element for every branch (also for airgap elements). o is the number of the inductor-resistor pairs of the model used, n is the total number of branch-reluctances of the model and m is the number of iron branch-reluctances.

The transformation matrices are defined

$$\boldsymbol{\phi}_{\mathrm{hfe}} = \mathbf{K}_{\mathrm{tf1}}\boldsymbol{\phi}_{\mathrm{h}} \tag{130}$$

$$\boldsymbol{i}_{\mathrm{ec}} \;=\; \mathbf{K}_{\mathrm{tf2}}\,\boldsymbol{i}_{\mathrm{ecfe}} \tag{131}$$

The inductance and resistance matrices of Eq. 126 are as follows

$$\boldsymbol{L}_{\mathrm{sub1}} = \begin{bmatrix} L_{\mathrm{ec11}} & 0 & \cdots & \cdots & 0 \\ -L_{\mathrm{ec11}} & L_{\mathrm{ec12}} & \ddots & & \vdots \\ 0 & -L_{\mathrm{ec12}} & L_{\mathrm{ec13}} & \ddots & \vdots \\ \vdots & \ddots & \ddots & \ddots & 0 \\ 0 & \cdots & 0 & -L_{\mathrm{ec1}(o-1)} & L_{\mathrm{ec1}o} \end{bmatrix}$$

$$\boldsymbol{L}_{\mathrm{ec}} = \begin{bmatrix} L_{\mathrm{sub1}} & 0 & \cdots & 0 \\ 0 & L_{\mathrm{sub2}} & \ddots & \vdots \\ \vdots & \ddots & \ddots & 0 \\ 0 & \cdots & 0 & L_{\mathrm{sub}m} \end{bmatrix} \tag{132}$$

$$\boldsymbol{R}_{\mathrm{sub1}} = \begin{bmatrix} R_{\mathrm{ec11}} & R_{\mathrm{ec11}} & \cdots & \cdots & R_{\mathrm{ec11}} \\ 0 & R_{\mathrm{ec12}} & \cdots & \cdots & R_{\mathrm{ec12}} \\ 0 & 0 & R_{\mathrm{ec13}} & \cdots & R_{\mathrm{ec13}} \\ \vdots & & \ddots & \ddots & \vdots \\ 0 & \cdots & \cdots & 0 & R_{\mathrm{ec1}o} \end{bmatrix}$$

$$\boldsymbol{R}_{\mathrm{ec}} = \begin{bmatrix} R_{\mathrm{sub1}} & 0 & \cdots & 0 \\ 0 & R_{\mathrm{sub2}} & \ddots & \vdots \\ \vdots & \ddots & \ddots & 0 \\ 0 & \cdots & 0 & R_{\mathrm{sub}m} \end{bmatrix} \tag{133}$$

The values of the matrix components are calculated from Eqs. 118 and 119. Based on the Eqs. $120 \cdots 133$ a linear model in state-space form can be written.

$$\dot{\boldsymbol{X}}_{\mathrm{B}} \;=\; \boldsymbol{A}_{\mathrm{B}}\boldsymbol{X}_{\mathrm{B}} + \boldsymbol{B}_{\mathrm{B}}\boldsymbol{U}_{\mathrm{B}} \tag{134}$$

$$\boldsymbol{Y}_{\mathrm{B}} \;=\; \boldsymbol{C}_{\mathrm{B}}\boldsymbol{X}_{\mathrm{B}} + \boldsymbol{D}_{\mathrm{B}}\boldsymbol{U}_{\mathrm{B}} \tag{135}$$

$$\boldsymbol{X}_{\mathrm{B}} \;=\; [i_1 \;\cdots\; i_k \;\; i_{\mathrm{ec11}} \;\cdots\; i_{\mathrm{ec1}(o)} \;\cdots\; i_{\mathrm{ec}m1} \;\cdots\; i_{\mathrm{ec}m(o)} \;\; \boldsymbol{p}^{\mathrm{T}}]^{\mathrm{T}} \tag{136}$$

$$\boldsymbol{Y}_{\mathrm{B}} \;=\; [i_1 \;\cdots\; i_k \;\; \boldsymbol{F}_{\mathrm{B}}^{\mathrm{T}}]^{\mathrm{T}} \tag{137}$$

$$\boldsymbol{U}_{\mathrm{B}} \;=\; [u_1 \;\cdots\; u_k \;\; \dot{\boldsymbol{p}}^{\mathrm{T}}]^{\mathrm{T}} \tag{138}$$

$$\boldsymbol{A}_{\mathrm{B}} \;=\; \begin{bmatrix} -\boldsymbol{I}_{\mathrm{B}}\boldsymbol{R} & -\boldsymbol{I}_{\mathrm{B}}\boldsymbol{N}^{\mathrm{T}}\boldsymbol{K}_3\;\mathrm{K}_{\mathrm{tf2}}\boldsymbol{I}_{\mathrm{A}}\boldsymbol{R}_{\mathrm{ec}} & \boldsymbol{0} \\ -\boldsymbol{I}_{\mathrm{A}}\;\mathrm{K}_{\mathrm{tf1}}\;\mathbf{T}^{\mathrm{T}}\boldsymbol{K}_1\boldsymbol{I}_{\mathrm{B}}\boldsymbol{R} & -\boldsymbol{I}_{\mathrm{A}}\boldsymbol{R}_{\mathrm{ec}} - \boldsymbol{I}_{\mathrm{A}}\;\mathrm{K}_{\mathrm{tf1}}\boldsymbol{T}^{\mathrm{T}}\boldsymbol{K}_1\boldsymbol{I}_{\mathrm{B}}\boldsymbol{N}^{\mathrm{T}}\boldsymbol{K}_3\;\mathrm{K}_{\mathrm{tf2}}\boldsymbol{I}_{\mathrm{A}}\boldsymbol{R}_{\mathrm{ec}} & \boldsymbol{0} \\ \boldsymbol{0} & \boldsymbol{0} & \boldsymbol{0} \end{bmatrix} \tag{139}$$

$$\boldsymbol{B}_{\mathrm{B}} = \begin{bmatrix} \boldsymbol{I}_{\mathrm{B}} & \boldsymbol{I}_{\mathrm{B}}(\boldsymbol{h}_{\mathrm{f}}{}^{\mathrm{T}} - \boldsymbol{N}^{\mathrm{T}}\boldsymbol{K}_3\ \mathrm{K}_{\mathrm{tf2}}\boldsymbol{I}_{\mathrm{A}}\ \mathrm{K}_{\mathrm{tf1}}\ \mathrm{T}^{\mathrm{T}}\boldsymbol{K}_2) \\ \boldsymbol{I}_{\mathrm{A}}\ \mathrm{K}_{\mathrm{tf1}}\ \mathrm{T}^{\mathrm{T}}\boldsymbol{K}_1\boldsymbol{I}_{\mathrm{B}} & \boldsymbol{I}_{\mathrm{A}}\ \mathrm{K}_{\mathrm{tf1}}\ \mathrm{T}^{\mathrm{T}}\boldsymbol{K}_1\boldsymbol{I}_{\mathrm{B}}(\boldsymbol{h}_{\mathrm{f}}{}^{\mathrm{T}} - \boldsymbol{N}^{\mathrm{T}}\boldsymbol{K}_3\ \mathrm{K}_{\mathrm{tf2}}\boldsymbol{I}_{\mathrm{A}}\ \mathrm{K}_{\mathrm{tf1}}\ \mathrm{T}^{\mathrm{T}}\boldsymbol{K}_2) \\ \boldsymbol{0} & \boldsymbol{I} \end{bmatrix} \tag{140}$$

$$\boldsymbol{C}_{\mathrm{B}} = \begin{bmatrix} \boldsymbol{I} & \boldsymbol{0} & \boldsymbol{0} \\ \boldsymbol{h}_{\mathrm{f}} & \boldsymbol{h}_{\boldsymbol{i}_{\mathrm{cefe}}} & \boldsymbol{c} \end{bmatrix} \tag{141}$$

$$\boldsymbol{I}_{\mathrm{A}} = [\boldsymbol{L}_{\mathrm{ec}} + \mathrm{K}_{\mathrm{tf1}}\boldsymbol{T}^{\mathrm{T}}\boldsymbol{K}_3\ \mathrm{K}_{\mathrm{tf2}}]^{-1} \tag{142}$$

$$\boldsymbol{I}_{\mathrm{B}} = [\boldsymbol{L}_{\mathrm{dyn}} - \boldsymbol{N}^{\mathrm{T}}\boldsymbol{K}_3\ \mathrm{K}_{\mathrm{tf2}}\boldsymbol{I}_{\mathrm{A}}\ \mathrm{K}_{\mathrm{tf1}}\ \mathrm{T}^{\mathrm{T}}\boldsymbol{K}_1]^{-1} \tag{143}$$

$$\boldsymbol{h}_{\boldsymbol{i}_{\mathrm{ecfe}}} = \boldsymbol{\Phi}^{\mathrm{T}}\ \mathrm{T}\frac{\partial \boldsymbol{R}_{\mathrm{m}}}{\partial \boldsymbol{p}}\ \mathrm{T}^{\mathrm{T}}\boldsymbol{P}^{-1}\ \mathrm{T}\ \mathrm{K}_{\mathrm{tf2}} \tag{144}$$

where $\boldsymbol{c}$ is the position stiffness as shown in the previous section.

3.4 Hysteresis model of the radial AMB

3.4.1 Hysteresis model

In the previous sections, the magnetic nonlinearity of iron was described by a single-valued reluctivity curve. In case of hysteresis, this has to be abandoned. In order to be able to model the magnetic hysteresis in AMB, a mathematical model of hysteresis is needed. Several models starting from analytical models and extending to well known models of Preisach, Jiles and several others are presented by Ivanyi [Ivanyi 1997]. However, in this section, a hysteresis model developed by Tellinen [Tellinen 1998] is used. This model is a relatively simple scalar model and appropriate to be used in accordance with the reluctance network model. The model has the property that both magnetic field intensity and magnetic flux density can be used as an input variable. In this section, the model is used as a quasistatic model, meaning that the eddy currents are neglected in the analysis. As the input data of the model, the limiting hysteresis loop has to be known. In this thesis, a measured limiting loop shown in Fig. 35 is used. The material used is Bochum V270-35A in rotor and V270-50A in stator parts. The scalar model used is

$$\frac{dB}{dH} = \mu_0 + \frac{B_{\mathrm{H}-}(H) - B}{B_{\mathrm{H}-}(H) - B_{\mathrm{H}+}(H)}\left[\frac{dB_{\mathrm{H}+}}{dH}(H) - \mu_0\right] \quad dH > 0 \tag{145}$$

$$\frac{dB}{dH} = \mu_0 + \frac{B - B_{\mathrm{H}+}(H)}{B_{\mathrm{H}-}(H) - B_{\mathrm{H}+}(H)}\left[\frac{dB_{\mathrm{H}-}}{dH}(H) - \mu_0\right] \quad dH < 0 \tag{146}$$

$$\frac{dH}{dB} = \frac{1}{\mu_0 + \frac{B_{\mathrm{H}-}(H)-B}{B_{\mathrm{H}-}(H)-B_{\mathrm{H}+}(H)}\left[\frac{dB_{\mathrm{H}+}}{dH}(H) - \mu_0\right]} \quad dB > 0 \tag{147}$$

$$\frac{dH}{dB} = \frac{1}{\mu_0 + \frac{B-B_{\mathrm{H}+}(H)}{B_{\mathrm{H}-}(H)-B_{\mathrm{H}+}(H)}\left[\frac{dB_{\mathrm{H}-}}{dH}(H) - \mu_0\right]} \quad dB < 0 \tag{148}$$

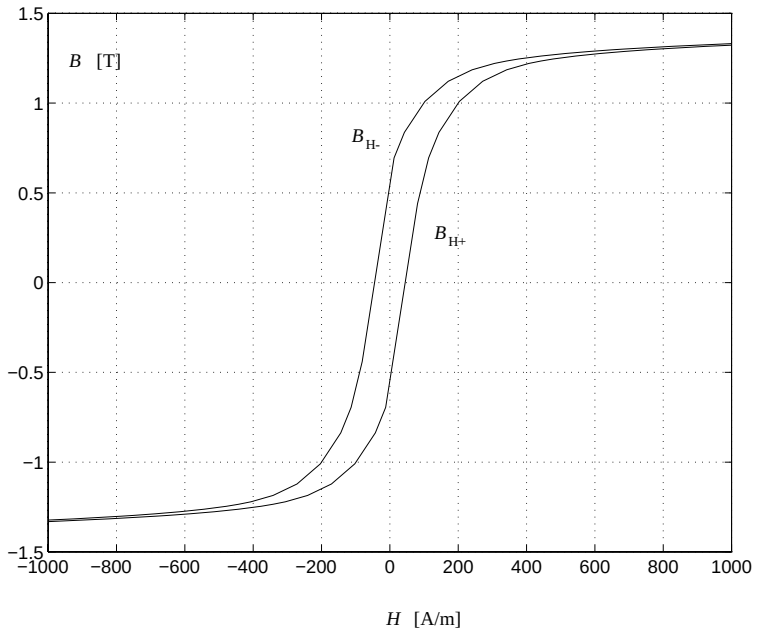

Figure 35: Measured hysteresis loop of V270-35A.

where $B_{\mathrm{H}-}$ and $B_{\mathrm{H}+}$ represent limiting hysteresis curves with decreasing and increasing magnetic field intensity, correspondingly. Similarly, $\frac{dB_{\mathrm{H}-}}{dH}$ and $\frac{dB_{\mathrm{H}+}}{dH}$ are the tangents of the limiting hysteresis curves. It should be noticed that the model has only two possible directions of changes in the BH-plane. The previous history of the magnetisation is not taken directly into account. This property, called local memory, restricts the applicability of the model. However, the simplicity of the model enables a straightforward implementation into the reluctance network.

3.4.2 Implementation of the hysteresis model into the reluctance network

The reluctance network model is a nonlinear model coupling both the magnetomotive force equations and circuit equations. In this case, it is necessary to use time stepping simulations to solve the system of equations. Also, the equation of motion of the rotor can be included in the model by changing the lengths of the airgap reluctances at every time step. The circuit and magnetomotive force equations are

$$\boldsymbol{u} = \frac{d\,\boldsymbol{\Psi}}{dt} + \boldsymbol{R}\boldsymbol{i} \tag{149}$$

$$\mathbf{T}\boldsymbol{f}_{\mathrm{h}} = \boldsymbol{M}_{\mathrm{f}} \tag{150}$$

These equations can be expressed as a function of loop-fluxes and coil currents, the notation being similar to the previous sections.

$$\boldsymbol{N}^{\mathrm{T}}\frac{d\boldsymbol{\Phi}}{dt} + \boldsymbol{R}\boldsymbol{i} = \boldsymbol{u} \tag{151}$$

$$\mathbf{T}\boldsymbol{R}_{\mathrm{m}}(\boldsymbol{\phi}_{\mathrm{h}})\ \mathbf{T}^{\mathrm{T}}\boldsymbol{\Phi} - \boldsymbol{N}\boldsymbol{i} = \boldsymbol{0} \tag{152}$$

In the time stepping formulation, the time derivatives of the loop- fluxes are approximated by first order differences known as backward Euler method

$$\frac{d\boldsymbol{\Phi}}{dt} = \frac{\boldsymbol{\Phi}_{t+1} - \boldsymbol{\Phi}_t}{\Delta t} \tag{153}$$

Finally, the time stepping nonlinear system of equations from time step t to $t+1$ can be written

$$\begin{bmatrix} \boldsymbol{N}^{\mathrm{T}} & \frac{1}{2}\boldsymbol{R}\Delta t \\ \mathbf{T}\boldsymbol{R}_{\mathrm{m}}\ \mathbf{T}^{\mathrm{T}} & -\boldsymbol{N} \end{bmatrix} \begin{bmatrix} \boldsymbol{\Phi}_{t+1} \\ \boldsymbol{i}_{t+1} \end{bmatrix} = \begin{bmatrix} \frac{1}{2}\Delta t & \boldsymbol{N}^{\mathrm{T}} & -\frac{1}{2}\boldsymbol{R}\Delta t \\ \boldsymbol{0} & \boldsymbol{0} & \boldsymbol{0} \end{bmatrix} \begin{bmatrix} \boldsymbol{u}_{t+1} + \boldsymbol{u}_t \\ \boldsymbol{\Phi}_t \\ \boldsymbol{i}_t \end{bmatrix} \tag{154}$$

$$\Longrightarrow \tag{155}$$

$$\boldsymbol{Q}\boldsymbol{z} = \boldsymbol{u}_{\mathrm{s}} \tag{156}$$

As the backward Euler method approximates the time derivative of the loop fluxes in the middle of the time steps, in Eq. 155 the averages of the current and voltage vectors between time steps t and $t+1$ are used. Above, the loop-flux and current variables are collected in vector $\boldsymbol{z}$, the right hand side of the equation into source vector $\boldsymbol{u}_{\mathrm{s}}$ and the system matrix into $\boldsymbol{Q}$.

Eq. 155 can be solved from the information of the previous time step and from the source voltage if it is known whether the flux densities in branch reluctances are increasing or decreasing. This can be found out based on the Jacobian of the previous time step. The Jacobian is formed with the aid of the hysteresis model of Eq. 145.

$$\boldsymbol{P}_t = \begin{bmatrix} \boldsymbol{N}_t & \frac{1}{2}\boldsymbol{R}\Delta t \\ \mathbf{T}\left(\frac{\partial(\boldsymbol{R}_{\mathrm{m}}(\boldsymbol{\phi}_{\mathrm{h}})\boldsymbol{\phi}_{\mathrm{h}})}{\partial\boldsymbol{\phi}_{\mathrm{h}}}\right)_t \mathbf{T}^{\mathrm{T}} & -\boldsymbol{N} \end{bmatrix} \tag{157}$$

$$\frac{\partial(R_{\mathrm{m}i}(\phi_{\mathrm{h}i})\phi_{\mathrm{h}i})}{\phi_{\mathrm{h}i}} = \frac{l_i}{A_{\mathrm{h}i}}\frac{dH_i}{dB_i} \tag{158}$$

where $\boldsymbol{P}_t$ is the Jacobian at time step t. The values of the Jacobian and variables at next time step are calculated as follows. The sign of the flux density difference is calculated from

$$sign(\Delta \boldsymbol{z}_{t+1}) = sign[(\boldsymbol{P_t})^{-1}(\Delta \boldsymbol{u}_{\mathrm{s}})_{t+1}] \quad (159)$$

$$\Delta \boldsymbol{z}_{t+1} = \boldsymbol{z}_{t+1} - \boldsymbol{z}_t \quad (160)$$

$$(\Delta \boldsymbol{u}_{\mathrm{s}})_{t+1} = (\boldsymbol{u}_{\mathrm{s}})_{t+1} - (\boldsymbol{u}_{\mathrm{s}})_t \quad (161)$$

$$(\Delta \boldsymbol{u}_{\mathrm{s}})_{t+1} = \frac{1}{2}(\boldsymbol{u}_{t+1} + \boldsymbol{u}_t) - \boldsymbol{R}\boldsymbol{i}_t \quad (162)$$

Based on this information the Jacobian at time step $t+1$ is then calculated and the values of the loop-fluxes and coil currents as well.

$$\boldsymbol{P}_{t+1} = \boldsymbol{P}_{t+1}(sign(\Delta \boldsymbol{z}_{t+1}), \boldsymbol{z}_t) \quad (163)$$

$$\Delta \boldsymbol{z}_{t+1} = (\boldsymbol{P}_{t+1})^{-1}(\Delta \boldsymbol{u}_{\mathrm{s}})_{t+1} \quad (164)$$

$$\boldsymbol{z}_{t+1} = \boldsymbol{z}_t + \Delta \boldsymbol{z}_{t+1} \quad (165)$$

It should be noticed that the Jacobian depends only on the values of the previous time step and on the sign of the flux density changes in the branch-reluctances. Thus, the model has only so called local memory and is exactly valid at an infinitesimally small time step. This feature makes the model simple as no iterative method has to be used. On the other hand, the time step has to be chosen carefully. However, the general choice of the time step is left as an open question in this thesis. A time step of $0.00002s$ is used, which has proven to be reasonable at the simulations done in this work. The force at a certain time step is calculated as was shown in Eq. 91.

An example of the results of a time stepping simulation is shown in Fig. 36. The calculations are made for the radial bearing of the test machine 2. The simulation is done for the current control circuit and the current reference value of 1.5 A at the frequency of 50 Hz. The current reference is supplied only in the x-direction. At y-direction only the bias current of 2.0 A is supplied. The initial values for the loop-fluxes are calculated by the stationary reluctance network model, where the permeability of the iron is modelled with a single valued monotonic permeability curve. The time dependence of the coil voltages, currents and bearing forces is shown. Also, the traces of the BH-curve in the stator tooth tips of the positive x-magnet are presented. The hysteresis effect is clearly seen in the trace plots. In the same plot, the limiting hysteresis curve of the material is shown. In the next section, based on these time stepping simulations the dynamic linearised parameters of radial bearing are calculated. The calculations are done by the describing function method. Thus, the components of the fundamental frequency are determined and, based on these components, the linearised parameters are calculated.

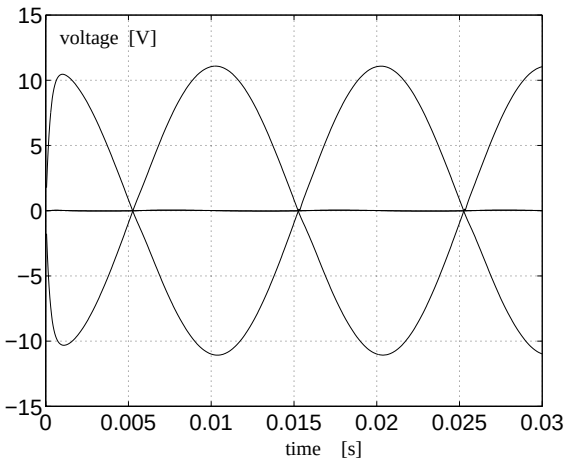

(a) The coil voltages.

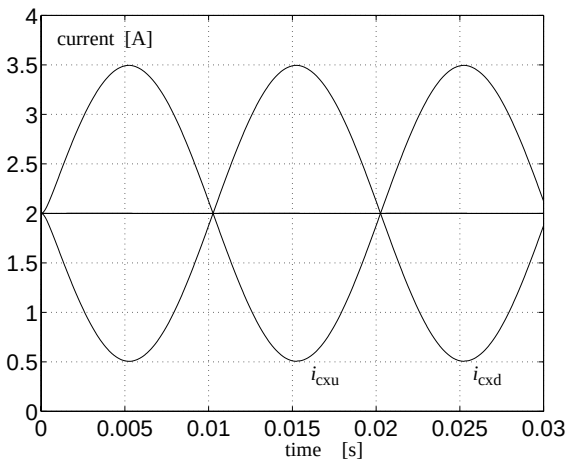

(b) The coil currents.

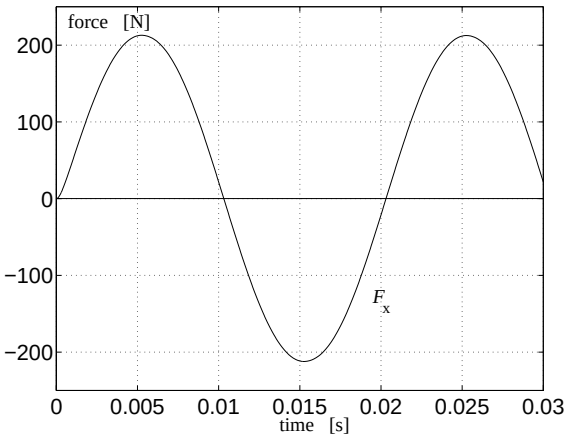

(c) The bearing forces.

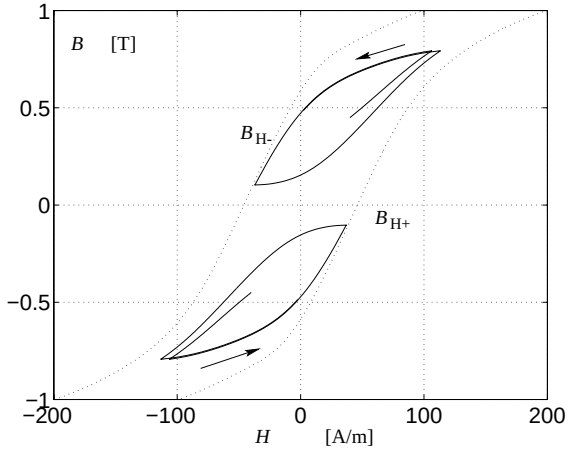

(d) The BH-trace in the stator tooth tips of the positive x-magnet.

Figure 36: Time stepping simulation with the hysteresis model of the current control circuit of the test machine 2. The current reference is 1.5 A at the frequency of 50 Hz in x-direction. The bias-currents are 2.0 A.

3.5 Experimental and calculated effects of eddy currents and hysteresis

3.5.1 Impedance measurement

As a first indication of the validity of the eddy current and hysteresis models, the dynamic inductance at two different airgaps was measured. The measurements were done with test machine 2. The frequency was swept from 50 Hz to 3 kHz. In these measurements, the rotor was locked with mechanical wrenches, hence the controller was turned off. However, the position of the rotor was measured from the electronics. Only one coil was supplied at a time. The coil was supplied by a linear power amplifier. In addition to the bias current, an AC-component of varying amplitude was supplied. The main interest in these measurements was the deviation of the phase angle of the dynamic inductance from the nominal value. Thus, with a pure inductive load the angle between voltage and current should be 90 degrees, but eddy currents reduce the phase angle by a few degrees depending on the frequency. The voltage was measured straight from the coil and the current was measured by a shunt resistor. The effect of the coil resistance was reduced from the measurements according to Eq. 166

$$L_{\mathrm{dyn}} = \frac{\boldsymbol{u}_{\mathrm{AC}} - R\boldsymbol{i}_{\mathrm{AC}}}{j\omega} \tag{166}$$

The estimation based on the eddy current model and the measured dynamic inductance of test machine 2 and is presented in Fig. 37. The impedance was measured at two airgap values. The DC-current was in both measurements 0.25 A. This corresponded to the airgap field of 0.15 T in the smaller airgap. Thus, both measurements were done in the linear region. Fig. 38 shows the same quantities calculated by the hysteresis model.

As can be seen, the calculated magnitudes of the impedance deviate from the measured ones. This is due to the inability of the reluctance network to model the airgap region properly. The proper modelling has to be done with FEM [Antila et al. 1998]. Interestingly, the hysteresis model estimates the magnitude to be about 5 % lower than the eddy current model, which is based on the single-valued reluctivity curve. As a crude estimate, one can assume the estimated phase to be the sum of eddy current and hysteresis model estimates. At higher frequencies, the agreement is not good. The main effects at higher frequencies are caused by the eddy currents. As was already mentioned, the excess loss component, which has a significant effect, was totally neglected in the analysis. The excess loss would roughly double the eddy current effect, so it is obvious that the deviation of the measured and calculated phases is not only because the excess loss is neglected.

The hysteresis model is a pseudostationary model, therefore the lowest measured frequency of 50 Hz does not strictly correspond to the model. In any case, it can be seen that

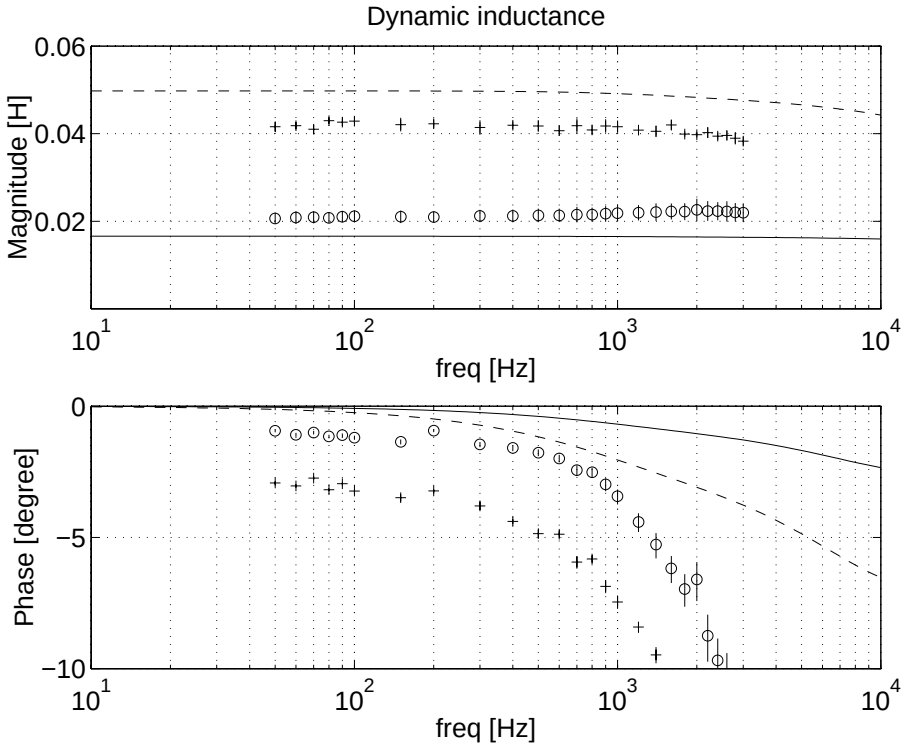

Figure 37: Dynamic inductances calculated by the eddy current model and the measured values. The '+' and 'o' are the measurements at smaller (0.216 mm) and larger airgap (0.884 mm), respectively. The dashed and solid lines are the corresponding calculated values.

the deviation of the phase from the pure inductance is larger with the smaller airgap. This is due to the fact that with the smaller airgap the iron part of the circuit plays a greater role. When assuming that the force is proportional to the time integral of voltage, this phase lag can be considered as an additional phase lag between current and bearing force.

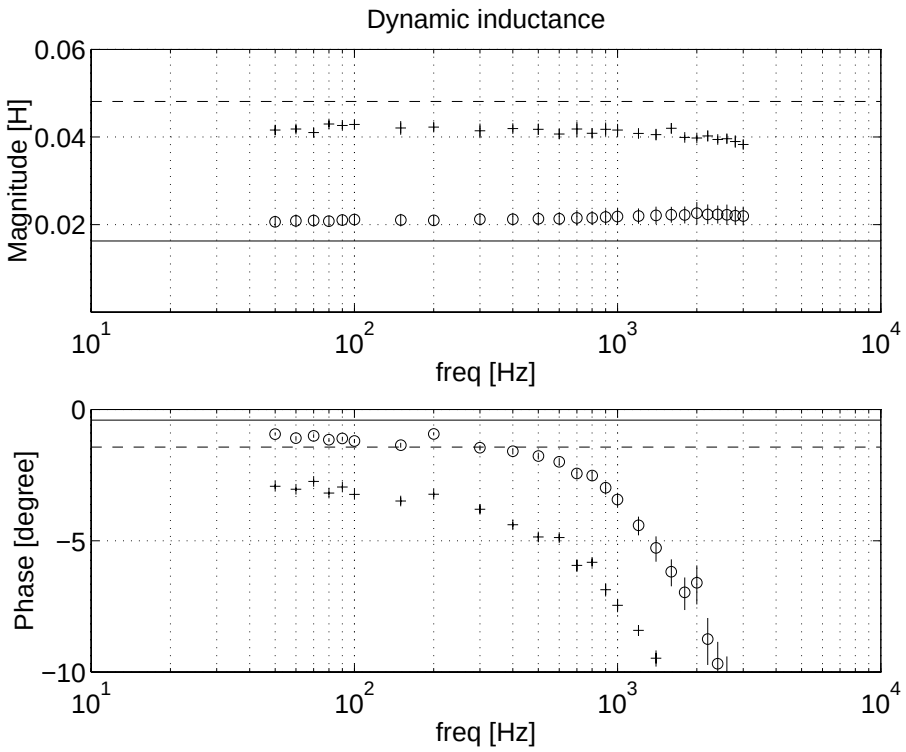

Figure 38: Dynamic inductances calculated by the hysteresis model and the measured values.The '+' and 'o' are the measurements at smaller (0.216 mm) and larger airgap (0.884 mm), respectively. The dashed and solid lines are the corresponding calculated values.

3.5.2 Dynamic force measurement

As a second measurement, the dependence of the bearing force from the coil current was measured. This measurement should reveal any additional phase lag in the current stiffness, which is the primary bearing parameter. The measurement was done by supplying disturbance at several frequencies to the controller output and measuring the acceleration of the rotor at both ends of the rotor. Thus, the bearing forces could be calculated. The voltage was measured directly from the coil ends and the current was measured by LEM-current transducers. The amplitude of the current at lower frequencies was chosen to be the same as the bias current, that is 2.0 A. The pole- configuration was NNSS. The bearing force was calculated based on the modal reduced finite element rotor model [Lantto 1997] and the values can be found in App. B.1

$$\boldsymbol{M}_{\mathrm{rot}}\ddot{\boldsymbol{q}} + \frac{\boldsymbol{K}_{\mathrm{rot}}}{s^2}\ddot{\boldsymbol{q}} = \boldsymbol{B}_{\mathrm{b}}\boldsymbol{F}_{\mathrm{b}} \tag{167}$$

$$\ddot{\boldsymbol{q}} = \boldsymbol{C}_{\mathrm{m}}\boldsymbol{a}_{\mathrm{c}} \tag{168}$$

$$\boldsymbol{F}_{\mathrm{b}} = \left[\boldsymbol{C}_{\mathrm{m}}\left(\boldsymbol{M}_{\mathrm{rot}} + \frac{\boldsymbol{K}_{\mathrm{rot}}}{s^2}\right)^{-1}\boldsymbol{B}_{\mathrm{b}}\right]^{-1}\boldsymbol{a}_{\mathrm{c}} \tag{169}$$

$$\boldsymbol{F}_{\mathrm{b}} = \left[F_{\mathrm{bD}}\ F_{\mathrm{bN}}\right]^{\mathrm{T}} \tag{170}$$

$$\boldsymbol{a}_{\mathrm{c}} = \left[a_{\mathrm{cD}}\ a_{\mathrm{cN}}\right]^{\mathrm{T}} \tag{171}$$

where $\boldsymbol{M}_{\mathrm{rot}}$, $\boldsymbol{K}_{\mathrm{rot}}$ are the modal mass and stiffness matrix in one plane, $\boldsymbol{F}_{\mathrm{b}}$ is the bearing force vector, $\boldsymbol{a}_{\mathrm{c}}$ is the vector of acceleration measurements, $\boldsymbol{B}_{\mathrm{b}}$, $\boldsymbol{C}_{\mathrm{m}}$ are coupling matrices. The model for magnetic bearing force is the familiar one dimensional form

$$F_{\mathrm{bD}} = h_{\mathrm{fD}}i_{\mathrm{cD}} + c_{\mathrm{D}}x_{\mathrm{D}} \tag{172}$$

where the quantities are at the D-end of the rotor. The primary interest is the current stiffness. Thus, the position stiffness was considered to be real valued and was estimated from the measurements by least square method. The current stiffness was then calculated from Eq. 172. In Fig. 39, comparison between the measured and calculated current stiffnesses are presented.

Both models overestimate the magnitude of the current stiffness. Once again the main source of error is the airgap area. On the one hand network model is unable to properly model the airgap area and on the other hand the magnetic airgap may deviate from the mechanical airgap [Antila et al. 1998]. The hysteresis model estimates the magnitude of five percent smaller than the eddy current model, as in case of the dynamic inductance. At low frequencies, the measured magnitude decreases. This is a purely calculational phenomenon as the position stiffness in Eq. 172 is estimated by one constant value. However, at smaller

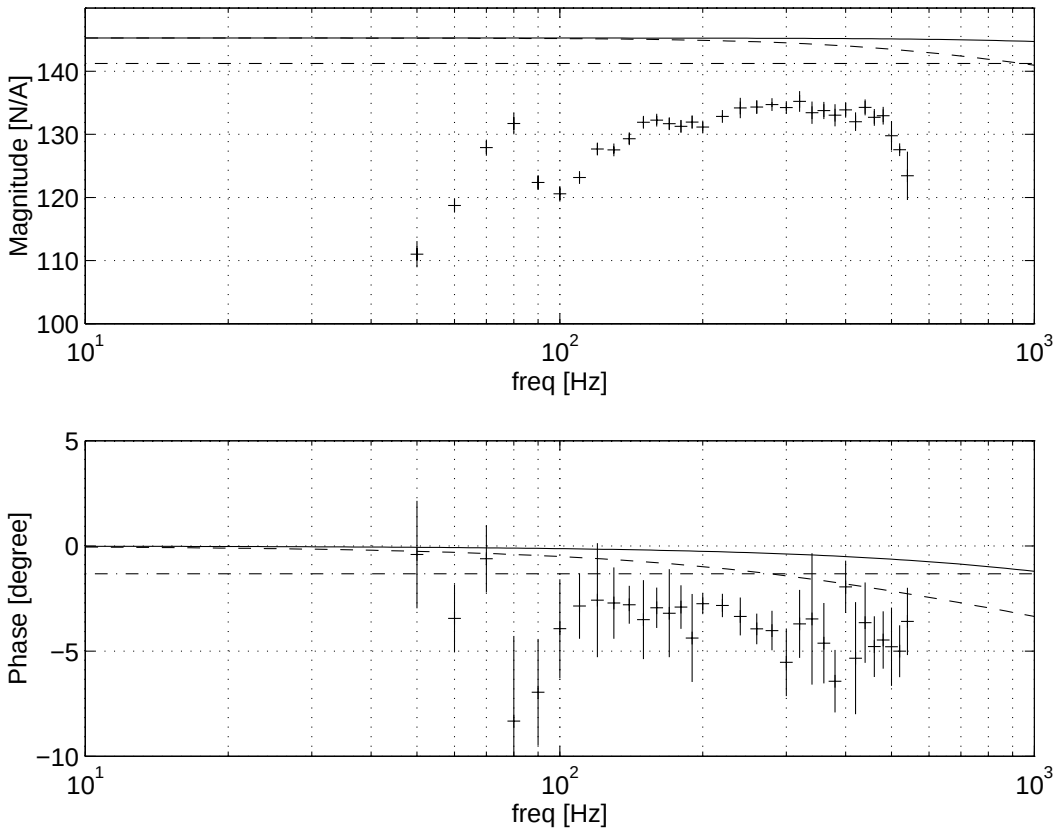

Figure 39: Current stiffness as a function of the frequency. The measured values and corresponding error margins are labelled with '+'. The solid line is the estimate based on the eddy current model. The dashed line is the eddy current estimate at double lamination thickness. The dashed-dot line is the estimate based on the hysteresis model.

frequencies, the vibration amplitudes are considerable with respect to airgap. So, the approximation of the position stiffness with one constant value is not valid at low frequencies.

The large oscillations of the measured phase at around 50-100 Hz are caused by the cylindrical and conical resonances of the system, which makes the phase measurement difficult. The agreement between the measured and calculated phases is not good. The fact that the excess loss was neglected explains some of the discrepancy. The deviation is larger at higher frequencies and could be caused by the additional unmodeled eddy current paths or the assumptions of the model. These are discussed in the conclusions.

The calculated current stiffness at the double lamination thickness are also plotted. This is purely to demonstrate the magnitude of the phase deviation. In any case, the important detail to consider is the phase lag of about five degrees between the measured current and bearing force. This causes a deterioration of the performance of the bearing system designed with the static parameters. Therefore, the designer can take this phase lag into consideration when designing the controller.

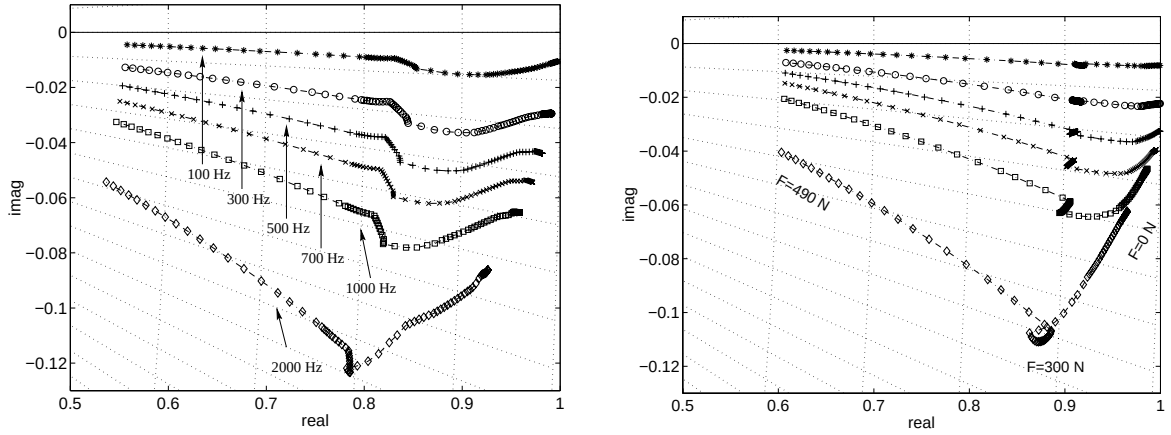

(a) NNSS -configuration.

(b) NSNS -configuration.

Figure 40: Relative dynamic current stiffness h_{frel} based on the eddy current model at several frequencies. The parameter is bearing force and it varies from zero to 490 N. The current stiffness is $h_{\mathrm{frel}} * 145N/A$. The sector lines are drawn at a half degree steps.

When designing the control system one would like to know the maximum phase lag these effects cause in realistic operation points. Based on the eddy current and hysteresis models, the dependance of the magnitude and phase lag on the operation point is studied. In Fig. 40, the relative dynamic current stiffness h_{frel} is presented. The current stiffness estimates based on the eddy current model are calculated at the lamination thicknesses 1 mm and at frequencies of 100, 300, 500, 700, 1000 and 2000 Hz.

The main interest is to find the relative changes of the phase as a function of the bearing force. The relative change is relatively independent of the frequency. Both pole- configurations are compared. In Fig. 41, the hysteresis estimates as a function of the bearing force are shown. The current amplitude of 0.3 A was used in the calculation.

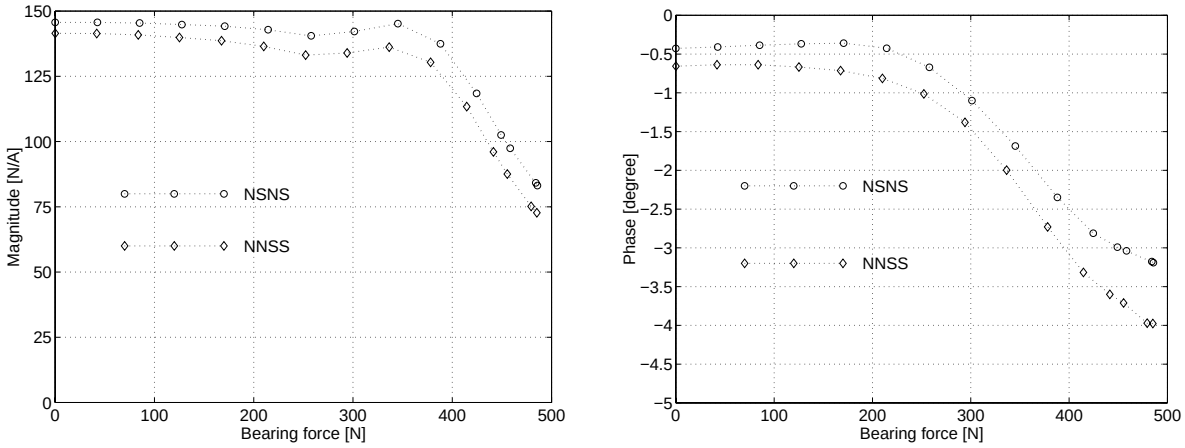

(a) Magnitude. *(b) Phase.*

Figure 41: Dynamic current stiffness based on the hysteresis model as function of the bearing force. The current amplitude is 0.3 A.

The decrement of the magnitude due to the saturation was also seen in the previous chapter. The saturation of the magnetic circuit is the major cause of the magnitude variations. The eddy current and hysteresis are of minor importance in this respect. However, the phase lag due to eddy currents increases as a function of the bearing force until the maximum is reached. This maximum is about 20-50 % higher than at the nominal point. The NSNS pole-configuration has smaller phase lag than NNSS -configuration. The phase lag due to hysteresis is at maximum at high bearing loads. Hence, one can estimate that the maximum phase lag due to a bearing load can be twice the phase lag at the nominal operation point.

3.6 Conclusions of the dynamic parameters

The reluctance network model estimates the magnitudes of dynamic impedance and current stiffness reasonably. The deviation between calculated and measured parameters is about 7-20 %. The eddy currents and hysteresis have a small effect on the magnitudes of these parameters. However, the saturation of the magnetic circuit and eccentricity of the rotor are the primary reasons for the variation of the magnitudes.

The phase estimations at lower frequencies are reasonable, indicating the validity of the hysteresis model. However, uncertainties exist which can produce errors in the hysteresis modelling. The magnetic properties of silicon iron are known to depend also on the mechanical stresses. In high-speed machines, in particular the rotor laminations are stacked with high pressure. This means that the real limiting hysteresis curve is not necessarily the one shown in Fig. 35.

At higher frequencies the agreement of the phase is not good. Part of this discrepancy is explained by the fact that we neglected the excess losses. The extra deviation is mainly due to two sources.

First, the model is inadequate to describe the eddy current effects. The main assumption is the form of the flux density inside the lamination, that is Eq. 102. This formula neglects the saturation in the lamination. At higher frequencies saturation is to happen near the surface of the sheet. In the impedance measurement, the AC-component was of the same size as the DC-component. Thus, even at smaller airgap the saturation is unlikely. The saturation could cause an unmodeled phase lag of few degrees. Anyhow at larger airgap, the flux density should remain well below saturation and no additional phase lag due to saturation should occur. Thus, the saturation inside the lamination is unlikely to be the reason for the discrepancy in the dynamic inductance measurement. In the current stiffness measurement, the current and flux density amplitudes are larger. For this reason, the saturation inside the lamination is likely to happen. A decrement in current stiffness above 500 Hz can be seen. This can be the effect of the saturation at the surface of the lamination. Another assumption in the model is that the end effects of the eddy currents are neglected. Thus, the model should overestimate the eddy currents. This means that the assumptions of the model are unlikely to explain the discrepancy of the measured and calculated phases.

Secondly, it was already mentioned that there are a lot of possible unmodeled eddy current paths. Fig. 39 presents also calculation with double lamination thickness. Qualitatively the effect is the same as the interlaminate currents, of course quantitatively nothing can be said. But a part of the discrepancy between the measured and calculated phases are propably due to the unmodelled eddy currents paths.

Thus, one can conclude that the accurate modelling of eddy currents is difficult. But from the practical point of view one can determine some guidelines for an AMB control

system designer.

The eddy currents and hysteresis have no significant effect on the magnitudes of the linearised parameters below 1000 Hz. Fig.37 and 38 showed clearly that the airgap has a large effect on the phase lag. From the controller's point of view the worst case is if the rotor is eccentric and a bearing load is applied in the direction of eccentricity. Then, on the one hand, the phase lag is large and, on the other hand, the gain of the system might be increased as the current stiffness can be large. Thus, the phase margin decreases and at same time the crossover frequency increases. The crossover frequency is typically around 100-200 Hz. At this frequency range, both the eddy currents and hysteresis affect the phase of the current stiffness. Therefore, it is reasonable to assume that the maximum phase lag can be twice the phase lag of the nominal point. By considering the measurements and the results of the calculation, the additional phase lag due to hysteresis and eddy currents at the crossover frequency region is up to ten degrees. In case the airgap length relative to the length of the iron part of the circuit is larger than in test machine 2, the above statement is conservative. The same applies if thicker lamination sheets are used in the bearing.

4 Summary

This thesis deals with the electromagnetic properties of radial active magnetic bearings. The approach is to study the electromagnetic actuator as a part of the control circuit. To be aware of the uncertainties of the system model is of primary importance for the control system designer. Keeping this in mind, the linearised parameters are studied in detail. A special interest is in studying the capabilities of extending the operation range into the magnetic saturation region. To be able to do this, a powerful nonlinear analysis method has to be found, and the finite element method is used. In addition, the extension of the operation range demands a careful investigation of the cross coupling properties. Based on nonlinear simulations, the effect of the power amplifier saturation has been quantified. The uncertainties of the linearised parameters caused by the hysteresis and eddy currents are studied by measurements and models based on the reluctance network field solution.

The stationary two dimensional finite element method is also found to be suitable for estimating the static linearised parameters of radial AMB in the magnetic saturation region. Accuracy of 10-15 % is achieved, which is appropriate. The dynamic inductance can change dramatically due to the saturation. For test machine 2, the range is from 25 mH to 5 mH. In the eccentric cases, the variation is even larger. The main dynamic effect is the phase lead at high frequencies, caused by the decrement of the dynamic inductance. This can destabilise the bending modes of the rotor. The variation of the current and position stiffness due to the saturation can be minimised by an appropriate choice of the bias current. For test machine 2, the minimum range is from 130 N/A to 50 N/A. This causes variations of the gain in the typical crossover frequency range and above. The ratio of the current and the position stiffness decreases due to the saturation. This dominates the dynamics at low frequencies and causes eventually instability when the ratio has decreased into the neighbourhood of the inverse of the proportional gain. Based on these parameter informations, it is possible to design linear controllers which perform satisfactorily also in the saturation region. With a simple gain scheduling scheme, the operation range could be widened and the performance improved. In this scheme, the gain of the controller is increased and the current control loop slowed when the load increases.

When the operation range is extended, the cross coupling of the bearing force can be significant. It turned out that the NNSS pole-configuration had significant cross couplings in the saturation range. The eccentricity worsened the situation. By considering the actuator response to a rotational control, the cross coupling can be regarded as a phase lag or phase lead. The cross coupling in NNSS- configuration can be regarded as producing phase errors up to 10 degrees. The NSNS pole configuration has negligible cross coupling and is also capable of producing a larger force than the NNSS -configuration at a same magnetomotive force. The NSNS -configuration also provides an opportunity for making the rotor shaft

radius larger. This has a significant effect on the rotor bending modes. Therefore, NSNS -configuration gives a greater freedom when designing the rotor.

The power amplifier saturation results in a serious additional phase lag in the current control loop. An interesting feature is that in presence of a high frequency large amplitude disturbance, which saturates the amplifier, the phase of the low frequency response increases with the amplitude of the low frequency reference. This property enables limit cycle oscillations. This can happen when e.g. the unbalance response saturates the amplifier or an unmodeled mechanical (stator) resonance is destabilised.

The eddy currents and hysteresis cause an additional phase lag in the control loop of a radial AMB. Eddy currents are especially important above 1 kHz. But even at lower frequencies the measurements reveal a phase lag of around five degrees. Based on the comparison of the models and measurements, it can be said that the quantitative estimation of the eddy current effects is difficult. The presumable reason is the unmodeled eddy current paths in the machines. Based on the measurements and models, the phase errors due to eddy currents and hysteresis below 1 kHz can be estimated to be up to 10 degrees.

References

[Ahrens and Kucera 1995] Ahrens M., Kucera L., "Cross Feedback Control of a Magnetic Bearing System," *Proceedings of the 3rd International Symposium on Magnetic Suspension Technology*, Tallahassee, FL, USA, 1995.

[Antila et al. 1996] Antila M., Lantto E., Saari J., Esa H., Lindgren O., Saily K., "Design of Water Treatment Compressors Equipped with Active Magnetic Bearings," *Proceedings of the Fifth International Symposium on Magnetic Bearings*, pp. 259-264, Kanazawa, Japan, 1996.

[Antila et al. 1998] Antila M., Lantto E., Arkkio A., "Determination of Forces and Linearised Parameters of Radial Active Magnetic Bearings by Finite Element Technique," accepted to be published in *IEEE Transactions on Magnetics*, 1998.

[Arkkio 1987] A. Arkkio, "Analysis of induction motors based on the numerical solution of the magnetic field and circuit equations," *Acta Polytechnica Scandinavica, Electrical Engineering Series No. 59*, Helsinki, Finland, 1987.

[Bleurer 1992] H. Bleurer, "A survey of magnetic levitation and magnetic bearing types," *JSME International Journal Series III*, Vol. 35, No. 3, 1992.

[Bleurer et al. 1994] H. Bleurer, C. Gahler, R. Herzog, R. Larsonneur, T. Mizuno, R. Siegwart, "Application of digital signal processors for industrial magnetic bearings," *IEEE Transactions on Control Systems Technology*, pp. 280-289, Vol. 2, No. 4, December 1994

[Bornstein 1991] Bornstein K.R., "Dynamic Load Capabilities of Active Magnetic Bearings," *Transactions of the ASME, Journal of Tribology*, Vol. 113, April 1991,pp. 598-603.

[Bottauscio 1996] Bottauscio O., Chiampi M., Repetto M., "Finite Element Analysis of Iron Loss Behaviour: Effect of Frequency and Lamination Thickness," *Proceedings of the 3rd International Workshop on Electric and Magnetic Fields*, pp. 417-422, Liege, Belgium, 1996.

[Brunet 1988] Brunet M., "Practical Applications of the Active Magnetic Bearings to the Industrial World," *Proceedings of the First International Symposium on Magnetic Bearings*, pp. 224-244, Zurich, Switzerland, 1988.

[Coulomb 1983] J.L. Coulomb, "A methodology for the determination of global quantities from a finite element analysis and its application to the evaluation of magnetic forces, torques and stiffnesses," *IEEE Transactions on Magnetics MAG-19*, pp. 2514-2519, No. 6.

[Cui and Nonami 1992] W.M. Cui, K. Nonami, "H_∞-Control of flexible rotor-magnetic bearing systems," *Proceedings of the 3rd International Symposium on Magnetic Bearings*, pp. 505-516, Alexandria , VA, USA, 1992.

[Dussaux 1990] M. Dussaux, "The industrial applications of the active magnetic bearings technology," *Proceedings of the Second International Symposium on Magnetic Bearings*, pp. 33-38, Tokyo, Japan, 1990.

[Earnshaw 1842] S. Earnshaw, "On the nature of the molecular forces which regulate the constitution of the lumiferous ether," *Trans. Camb. Phil. Soc.*, vol. 7, pp. 97-112, 1842.

[Fremerey 1988] J.K. Fremerey, "Radial shear force permanent magnet bearing system with zero-power axial control and passive radial damping," *Proceedings of the First International Symposium on Magnetic Bearings*, pp. 25-31, Zurich, Switzerland, 1988.

[Fujita et al. 1992] M. Fujita, F. Matsumura, T. Namerikawa, "μ-Analysis and synthesis of a flexible beam magnetic suspension system," *Proceedings of the 3rd International Symposium on Magnetic Bearings*, pp. 495-504, Alexandria , VA, USA, 1992.

[Habermann and Brunet 1984] H. Habermann, M. Brunet, "The active magnetic bearing enables optimum damping of flexible rotor," *ASME Paper* No. 84-GT-114, 1984.

[Hara et al. 1996] Hara S., Namerikawa T., Matsumura F., "Improvement of Dynamic Response by Flux Feedback on Active Magnetic Bearings," *Proceedings of the Fifth International Symposium on Magnetic Bearings*, pp. 49-54, Kanazawa, Japan, 1996.

[Hsiao and Lee 1994] Hsiao F.-Z., Lee A.-C., "An investigation of the characteristic of electromagnetic bearings using the finite element method," *Transaction of the ASME Journal of Tribology*, pp. 710-719, vol. 116, October 1994.

[Humpris et al. 1986] R. Humpris, R. Kelm, D. Lewis, P. Allaire, "Effect of control algorithms on magnetic journal bearing properties," *Transactions of the ASME, Journal of Engineering for Gas Turbines and Power*, Paper No. 86-GT-54, 1986.

[Imlach et al. 1991] Imlach J., Blair B.J., Allaire P., "Measured and predicted force and stiffness characteristic of industrial magnetic bearings," *Transaction of the ASME Journal of Tribology*, pp. 784-788, vol. 113, October 1991.

[Ivanyi 1997] Ivanyi A., "Hysteresis Models in Electromagnetic Computation," Akademiai Kiado, Budapest, Hungary, 1997.

[Jayawant 1981] B.V. Jayawant, "Electromagnetic suspension and levitation," *Reports on Progress in Physics*, Vol. 44, pp. 411-477, April 1981.

[Kasarda et al. 1994] Kasarda M., Allaire P., Maslen E., Gillies G., "Design of a High Speed Rotating Loss Test Rig for Radial Magnetic Bearings," *Proceedings of 4th International Symposium on Magnetic Bearings*, pp. 577-582, Zurich, Switzerland, 1994

[Knight et al. 1992] Knight J., Xia Z., McCaul E., Hacker H.Jr., "Determination of forces in a magnetic bearing actuator: Numerical computation with comparison to experiment," *Transaction of the ASME Journal of Tribology*, pp. 796-801, vol. 114, October 1992.

[Knight et al. 1993] Knight J., Xia Z., McCaul E., "Forces in Magnetic Journal Bearings: Nonlinear Computation and Experimental Measurement," *Proceedings of 3rd International Symposium on Magnetic Bearings*, pp. 441-450, Alexandria, VA, USA, 1992.

[Knospe and Collins 1996] Knospe C.R., Collins E.G., "Special issue on magnetic bearing control," *IEEE Transactions on Control System Technology*, Vol. 4, No. 5, September 1996.

[Knospe et al. 1997] Knospe C.R., Fedigan S.J., Hope R.W., Williams R.D., "A Multitasking DSP Implementation of Adaptive Magnetic Bearing Control," *IEEE Transactions on Control Systems Technology*, Vol. 5, NO. 2, pp. 230-238, March 1997.

[Lantto and Antila 1995] Lantto E., Antila M., "Active Magnetic Bearings for High-Speed Machines," *The Proceedings of Stockholm Power Tech, International Symposium on Electric Power Engineering, Royal Institute of Technology and IEEE Power Engineering Society*, pp. 69-74, Stockholm, Sweden, 1995.

[Lantto et al. 1996] Lantto E., Vaananen J., Antila M., "Effect of Foundation Stiffness on Active Magnetic Bearing Suspension," *Proceedings of the Fifth International Symposium on Magnetic Bearings*, pp. 37-43, Kanazawa, Japan, 1996.

[Lantto 1997] Lantto E., "Finite Element Model for Elastic Rotating Shaft," *Acta Polytechnica Scandinavica*. Electrical Engineering Series No. 88, 1997.

[Lantto et al. 1997] Lantto E., Antila M., Tommila V., Saari J., Lindgren O., "Experiences on 250 kW High-Speed Turbocompressors installed in a pulp and paper mill," *Proceeding of MAG '97*, Virginia, USA, 1997.

[Lantto et al. 1998] Lantto E., Antila M., Tommila V., "Robustness Analysis of AMB suspension," *to be published in the Proceedings of 6th ISMB*, 1998.

[Lantto 1998] Lantto E., Thesis for Doctor of Technology.

[Larjola 1988] Larjola J., "The principle of high speed technology." *Proceedings of the Conference on High Speed Technology*, August 21-24 1988,pp. 11-28, Lappeenranta, Finland, 1988.

[Larsonneur 1990] Larsonneur R., "Thesis for Doctor of Technical Sciences," Diss. ETH No. 9140, Zurich, Switzerland, 1990.

[Larsonneur and Herzog 1994] Larsonneur R., Herzog R.J.P., "Feedforward Compensation of Unbalance: New Results and Application Experiences," *Proceedings of IUTAM Symposium the Active Control of Vibration*, Bath, UK, pp.45-52, 1994.

[Lee et al. 1994] A.-C. Lee, F.-Z. Hsiao, D. Ko, "Analysis and testing of magnetic bearing with permanent magnets for bias," *JSME International Journal, Series C*, pp. 774-782, vol. 37, No. 4, 1994.

[Lindgren et al. 1995] Lindgren O.,Saily K.,Lantto E., Saari J., Antila M., "Electromechanical design of motors and active magnetic bearings for high-speed compressors," *Proceedings of MAG'95 Magnetic Bearings, Magnetic Drives and Dry Gas Seals Conference and Exhibition*, pp. 47-55, Alexandria, VA, USA, 1995.

[Maslen et al. 1989] Maslen E., Hermann P., Scott M., Humphris R.R., "Practical Limits to the Performance of Magnetic Bearings: Peak Force, Slew rate, and Displacement sensitivity," *Transactions of the ASME, Journal of Tribology*, Vol. 111, pp. 331-336, April 1989.

[Matsumura and Hatake 1992] Matsumura F., Hatake K., "Relation between Magnetic Pole Arrangement and Magnetic Loss in Magnetic Bearing," *Proceedings of 3rd International Symposium on Magnetic Bearings*, pp. 274-283, Alexandria, VA, USA, 1992.

[Meeker and Maslen 1996] D.C. Meeker, Maslen E.H., "Augmented Circuit Model for Magnetic Bearings Including Eddy Currents, Fringing and Leakage," *IEEE Transactions on Magnetics*, pp. Vol. 32, NO. 4, July 1996.

[Meeks et al. 1994] C. Meeks, P. Mc Mullen, D. Hibner, L. Rosado, "Lightweight magnetic bearing system for aircraft gas turbine engines," *Proceedings of the Fourth International Symposium on Magnetic Bearings*, pp. 429-434, Zurich, Switzerland, 1994.

[Mizuno and Higuchi 1994] Mizuno T., Higuchi T., "Experimental Measurement of Rotational Losses in Magnetic Bearings," *Proceedings of 4th International Symposium on Magnetic Bearings*, pp. 591-595, Zurich, Switzerland, 1994.

[Moon 1994] F. Moon, "Progress in superconducting magnetic bearings," *Proceedings of the Fourth International Symposium on Magnetic Bearings*, pp. 411-416, Zurich, Switzerland, 1994.

[Nonami and Yamaguchi 1992] K. Nonami, H. Yamaguchi, "Robust control of magnetic bearing systems by means of sliding mode control," *Proceedings of the 3rd International Symposium on Magnetic Bearings*, pp. 537-546, Alexandria , VA, USA, 1992.

[Patent U.S. 5473211] "Asynchronous electric machine and rotor and stator for use in association therewith," *Patent U.S. 5473211*, High Speed Tech Oy Ltd, Tampere, Finland, Appl. No. 86880, 9 p, 7.7.1992.

[Reichert et al. 1976] K. Reichert, H. Freundl, W. Vogt, "The calculation of forces and torques within numerical magnetic field calculation methods," *Proceedings of Compumag, Oxford, UK*, pp. 64-73, 1976.

[Saari 1995] Saari J., "Thermal modelling of High-Speed Induction Machines" *Acta Polytechnica Scandinavica*, Electrical Engineering Series No. 82, 1995.

[Saari 1998] Saari J., "Thermal Analysis of High-Speed Induction Machines" *Acta Polytechnica Scandinavica*, Electrical Engineering Series No. 90, 1998.

[Satoh et al. 1990] I. Satoh, C. Murakami, A. Nakajima, Y. Kanemitsu, "A Self-Excited Vibration of Magnetic Bearing System with Flexible Structure," *Proceedings of the Second International Symposium on Magnetic Bearings*, pp. 329-335, Tokyo, Japan, 1990.

[Saitz 1997] J. Saitz, "Calculation of iron losses in electrical machines," Report 51, 57p., Espoo, Finland, Helsinki University of Technology, Laboratory of Electromechanics, 1997.

[Schmidt et al. 1996] E. Schmidt, T. Platter, H. Springer, "Force and Stiffness Calculations in Magnetic Bearings-Comparision between Finite Element Method and Network Theory," *Proceedings of the Fifth International Symposium on Magnetic Bearings*, pp. 259-264, Kanazawa, Japan, 1996.

[Schweitzer et al. 1994] G. Schweitzer, H. Bleurer, A. Traxler, "Active Magnetic Bearings," Zurich, Switzerland, Vdf Hochschulverlag AG an der ETH Zurich, 1994.

[Sortore et al. 1990] C. Sortore, P. Allaire, Maslen E., R. Humpris, P. Studer, "Permanent magnet biased magnetic bearings," *Proceedings of the Second International Symposium on Magnetic Bearings*, pp. 175-182, Tokyo, Japan, 1990.

[Stoll 1974] Stoll R.L., "The Analysis of Eddy Currents," London:Oxford University Press, 1974.

[Tellinen 1998] Tellinen J., "A simple scalar model for magnetic hysteresis," accepted to be published in *IEEE Transactions on Magnetics*, 1998.

[Ueyama and Fujimoto 1990] Ueyama H., Fujimoto Y., "Iron losses and Windy Losses of High Rotational Speed Rotor Suspended by Magnetic Bearings," *Proceedings of 2nd International Symposium on Magnetic Bearings* , pp. 237-242, Tokyo, Japan, 1990.

[Vance 1988] Vance J.M., "Rotordynamics of Turbomachinery," New York, John Wiley & Sons, 1988.

[Zhuravlyov 1992] Y. Zhuravlyov, "Active Magnetic Bearings," Report 37, 92p., Espoo, Finland, Helsinki University of Technology, Laboratory of Electromechanics, 1992.

[Zmood et al. 1987] Zmood R.B., Anand D.K., Kirk J.A., "The influence of Eddy Currents on Magnetic Actuator Perfomance," *Proc. IEEE*, Vol. 75,pp. 259-260, Feb. 1987.

Appendix

A Controllers

A.1 1D controller

$$i_{\mathrm{ref}} = G_{\mathrm{c}} x_{\mathrm{ref}} \tag{A.1}$$

$$i_{\mathrm{ref}} = i_{\mathrm{refDC}} + \Delta i_{\mathrm{ref}} \tag{A.2}$$

$$i = i_{\mathrm{DC}} + \Delta i_{\mathrm{c}} \tag{A.3}$$

$$G_{\mathrm{c}} = \frac{1}{\frac{s^2}{(\omega_0)^2} + \frac{s2\xi}{\omega_0} + 1}[k_{\mathrm{p}}(1 + \frac{1}{sT_{\mathrm{i}}}) + \frac{sk_{\mathrm{d}}}{sT_{\mathrm{d}} + 1}] \tag{A.4}$$

$$\Delta u_{\mathrm{c}} = k_{\mathrm{cf}}(\Delta i_{\mathrm{ref}} - \Delta i_{\mathrm{c}}) \tag{A.5}$$

A.2 1-plane controller

$$\begin{bmatrix} i_{\mathrm{refD}} \\ i_{\mathrm{refN}} \end{bmatrix} = \begin{bmatrix} G_{\mathrm{C}} & k_{\mathrm{cr}} G_{\mathrm{C}} \\ k_{\mathrm{cr}} G_{\mathrm{C}} & G_{\mathrm{C}} \end{bmatrix} \begin{bmatrix} x_{\mathrm{refD}} \\ x_{\mathrm{refN}} \end{bmatrix} \tag{A.6}$$

$$\boldsymbol{G}_{\mathrm{c}} = \begin{bmatrix} G_{\mathrm{C}} & k_{\mathrm{cr}} G_{\mathrm{C}} \\ k_{\mathrm{cr}} G_{\mathrm{C}} & G_{\mathrm{C}} \end{bmatrix} \tag{A.7}$$

ω_0	$2\ \pi\ 707$	[rad/s]
ξ	0.1	
k_{p}	16911	[A/m]
k_{d}	38	[A s/m]
k_{cf}	75	[V/A]
k_{cf}	0.3	
T_{i}	0.15	[s]
T_{d}	0.00015	[s]

B Rotor model

B.1 The rotor model of the test machine 2

$$\boldsymbol{M}_{\mathrm{rot}} = \begin{bmatrix} 20.89 & 0 & 0 \\ 0 & 0.3817 & 0 \\ 0 & 0 & 8.7439 \times 10^{7} \end{bmatrix} \tag{B.8}$$

$$\boldsymbol{K}_{\mathrm{rot}} = \begin{bmatrix} 0 & 0 & 0 \\ 0 & 0 & 0 \\ 0 & 0 & 2.5232 \times 10^{7} \end{bmatrix} \tag{B.9}$$

$$\boldsymbol{G}_{\mathrm{rot}} = \begin{bmatrix} 0 & 0 & 0 \\ 0 & 1.8839 \times 10^{-2} & -3.2711 \times 10^{-3} \\ 0 & -3.2711 \times 10^{-2} & 3.2323^{-2} \end{bmatrix} \tag{B.10}$$

$$\boldsymbol{B}_{\mathrm{b}} = \begin{bmatrix} 1 & 1 \\ 0.2089 & -0.2161 \\ 0.09296 & 0.16391 \end{bmatrix} \tag{B.11}$$

$$\boldsymbol{C}_{\mathrm{m}} = \begin{bmatrix} 1 & 0.2838 & 0.5482 \\ 1 & -0.2831 & 0.38142 \end{bmatrix} \tag{B.12}$$